Atomistic Modeling of Deformation at the Nanoscale

by

Donald K. Ward

B. E., Engineering(Mechanical),
Colorado School of Mines, 2001

A dissertation submitted in partial fulfillment of the
requirements for the Degree of Doctor of Philosophy
in the Division of Engineering at Brown University

Providence, Rhode Island
May, 2008

This dissertation by Donald K. Ward is accepted in its present form by the Division of Engineering as satisfying the dissertation requirement for the degree of Doctor of Philosophy.

Date _____ _____

Professor William A. Curtin, Adviser

Recommended to the Graduate Council

Date _____ _____

Professor K.-S. Kim, Reader

Date _____ _____

Professor S. Kumar, Reader

Approved by the Graduate Council

Date _____ _____

Shiela Bonde
Dean of the Graduate School

Vita

Donald Keenan Ward was born in Sacramento, CA on March 27th, 1979. He was raised in Placerville, CA for his entire child hood, along with his older sister Chelsea and younger brother Jonathan, by parents Michael and Francine. Placerville, nestled in the foothills of the Sierra Nevadas offered a peaceful rural surrounding for Donald to grow and learn. He attended El Dorado High School and participated on the Varsity Golf and Soccer teams as well as several academic societies. Upon Graduation Donald moved to Golden, CO in the fall of 1997, to attend Colorado School of Mines. While at Mines Donald studied Engineering with a Mechanical specialty. Along with academics Mines offered the opportunity to explore the outdoors as well. Donald endulged in fishing, hiking, biking and snowboarding while in CO. Donald received a B.S. in Engineering in 2001 and moved to Providence that fall to begin his graduate career at Brown Univeristy.

Acknowledgements

I would like to start by thanking my advisor Prof. William Curtin. Your support, guidance and most importantly your patience has been greatly appreciated. To the entire Brown community and Engineering department thank you for helping to make my learning experience one I will always remember. Dr. Mark Lusk, thank you for your encouragement and your advice to apply to graduate school.

To my friends here in Providence you have truly made this home, Festivities, Birthdays, Thanksgivings and all other events have been unforgetable and warm because all of you. Jean, thanks for putting up with me and reading my papers and listening to my whining. Pat, Mark, Eddy, Ray, and Brian, thanks for the Monday lunch time. Dave, my co-manager, we are a dynasty. Steve you were the best roommate a guy could ask for. Brian, 3:00 coffee will remain a staple in my life. Also, thanks too Ashwin and the Mikes (O'day and Dewald). Mark, who's better than us?

This thesis could not have been completed with out the help of Dhananjay Tambe who taught me everything I know about Latex. Thank you so much for everything and good luck with your Harvard adventure.

Other Dave, moving out east was not easy, hearing you were moving out as well was a big help. Thanks for being there and always giving me an escape from Provi.

Most importantly I need to thank my family. With out their support and love this would have been impossible. Mom and Dad, I love you. I would run out of room

if I tried to fit everything I owe you on this page so I will just simply say thank you. Chels and Roger, you guys have been a rock for me and when ever I have faced a difficult situation you have been there to talk me off the ledge. I can not tell you enough how much it has meant to me I love you. Jon, my brother in arms, you are my best friend. Whenever I needed to chat and needed something light hearted you were there, love ya. Thank you Family!

I dedicate this to my Parents.

Contents

⋆ Parts of this thesis have appeared in the following publications:

Ward, D.K., Lian, J., Curtin, W.A., Farkas, D., Wang, J., Kim, K.-S., Qi, Y. (2008), 'Size-scaling of plastic deformation in nanoscale asperities', Submitted to PNAS.

Ward, D.K., Lian, J., Curtin, W.A., Farkas, D., Wang, J., Kim, K.-S., Qi, Y. (2008), 'An Energetic Model to Predict Size-Scaling of Nanoscale Plasticity', Submitted to TBA.

Ward, D.K., Curtin, W.A., and Qi, Yue (2006), 'Mechanical behavior of aluminum-silicon nanocomposites: A molecular dynamics study', *Acta Materialia*, **54**(17), 4441–4451.

Ward, D.K., Curtin, W.A., and Qi, Yue (2006), 'Aluminum-silicon interfaces and nanocomposties: A molecular dynamics study', *Composites Science and Technology*, **66**, 1148–1158.

Wang, J., Ward, D.K., Curtin, W.A., Kim, K.-S. (2003), 'Contact compression of self-assembled nano- and micro-scale pyramid structures on Au(100) surface', *Continuous Nanophase and Nanostructoured Materials: MRS Symposium - Proceedings*, **788**, 159–164.

List of Tables

List of Figures

Chapter 1

Introduction

Nanoscale systems have been an extremely active area of research in recent years. Topics ranging from nano-machines to nano-crystalline-coatings have flooded engineering and physics journals with novel ideas and practical applications. With experiments showing exciting new behavior for materials at the nano-scale it has become increasingly more important to try and understand the underlying physics such that the benefits can be harnessed and applied to industrial and commercial applications. Of particular interest are the systems that show superior mechanical properties at a nanoscale relative to their bulk counterparts.

The scientific community was first introduced to the idea of improving mechanical properties with decreasing size by Hall (1951) and Petch (1953). They were the first to show flow stress for a polycrystalline material will increase with decreasing grain size. These studies also established a simple relationship or "size-scaling" where the flow stress increases proportionally to the inverse of the square root of the grain-size, $\sigma \propto d^{-1/2}$. The current speculated mechanism responsible for this hardening is the piling up of dislocations at grain boundaries resulting in higher stresses necessary for either dislocation avalanches to penetrate the grain boundary or for dislocation nucleation on the opposite side of the grain boundary (Louchet *et al.* (2006)). The

scaling arises from the summation of the $1/d$ stress contribution from each dislocation inhibited at the grain boundary (Armstrong *et al.* (1966); Friedman and Chrzan (1998)).

Since the introduction of Hall-Petch behavior other properties have been shown to improve at smaller lengths scales and many have speculated on the mechanisms responsible for the behavior. For example, as grain sizes in polycrystals decrease, experimental and numerical studies indicate that these materials exhibit increasing strengths; Van Swygenhoven *et al.* (1999, 2003, 2002); Derlet and Van Swygenhoven (2002); Schiøtz *et al.* (1998, 1999); Yamakov *et al.* (2002, 2001). Many single-phase nanocrystalline materials have been studied to understand the deformation mechanisms related to decreasing grain size. More recently hardness and wear have also been shown to depend on grain size by Farhat *et al.* (1996). Hardness tests show that the same $d^{-1/2}$ scaling arises due to a mechanism similar to that responsible for scaling of the flow stress . Wear also shows a lower peak coefficient of friction with decreasing grain size because less energy is expended by plowing and shearing of smaller grains.

The $d^{-1/2}$ scaling begins to break down as crystalline materials approach the nanograin (ng) sizes, $d < 100$ nm. For the ng regime the scaling exponent is greater than the $-1/2$ exponent of larger grain sizes. Materials consisting of ngs are more dependent on locations of dislocation sources (Louchet *et al.* (2006)) and the activation of secondary, non-dislocation mechanisms, such as grain boundary sliding, which become active (Schiøtz *et al.* (1998, 1999)). For ng materials with grain sizes $d < 10$ nm the material actually begins to soften as the secondary mechanisms dominate the deformation resulting in a "Reverse Hall-Petch" behavior (Schiøtz *et al.* (1998)).

For crystalline materials the question of how to optimize superior nano-scale properties without compromising other properties ultimately drives a large amount of industrial research. One aspect that has not been significantly studied is the effect of introducing a second phase into the nano-crystal. The introduction of a second phase has been shown to stabilize nanocrystals and allow properties to improve beyond their single phase limits (Ping *et al.* (2000)). Yet, experiments to elucidate nanocrystalline mechanical properties are difficult to perform because most processes used to create nanocrystals, e.g. electro-deposition, are only capable of creating sheets with thicknesses of ~ 100 μm that contain a significant amount of impurities.

Nano-crystalline composite Ag-Ni (Cheng and Drew (1997)), Al-Ge (Adams *et al.* (1992)) coatings, with two phases separated, have been made through co-deposition methods. Fucutani *et al.* (2004) have shown that with strictly controlled deposition conditions the nanostructure of Al-Si films is close to an idealized cylindrical morphology with 7-10 nm crystal Al cylinders embedded in the amorphous Si matrix. Such nanocomposites may improve the stability of nanomaterials against grain growth and creep, may improve stiffness, and may enhance other mechanical properties such as hardness and wear resistance. Nanocomposites are thus an attractive area for investigation but only one computational study has been done on two-phase nanocomposites. A Ni-Ag composite has been studied numerically using Molecular Dynamics(MD), and it was found that the introduction of a second phase decreases the tensile strength of the composite and also reduces the effectiveness of grain boundary sliding, grain rotations, and recrystallization in acting as deformation mechanisms, relative to single phase composites (Qi and Cheng (2004)). To this point the limited MD studies have not examined the metal/ceramic composites commonly used for coatings and have not studied the effect of strain rates.

As seen from experiments an important component of composites mechanical response is the behavior of the two phase interface. Metal/silicon interfaces have been studied previously on a very limited scale. Baskes *et al.* (1994) and Gall *et al.* (2000) studied (001) out of plane oriented Ni(110)/Si(100) and Al(100)/Si(100) interfaces, respectively. Baskes *et al*. studied the results on the interface associated with atomic mismatch. The low energy interface configurations resulted in a ripple effect at the metal/Si interface. Gall *et al*. concluded that premature failure and residual bonding of the metal onto the Si interface results from a stress concentration created by the ripple energy at the interface. Gall *et al*. also studied failures associated with small voids in the metal near the interface, resulting in lower interfacial tensile strengths as the void size increases. These simulations exhibited high strength interfaces on the order of 6-9 GPa and significantly enhanced toughness relative to a normal Griffith fracture.

Beyond polycrystalline, materials size-scaling has also been reported in single crystal metals, and extends to length scales smaller than those at which secondary mechanisms are activated in polycrystalline materials. Without grain boundaries, pile up mechanisms are not responsible for the scaling exhibited by single crystals thus the hardening must come from an alternate source. Many experimental studies elucidate the size effects in single crystals. Aifantis (1999) showed increasing flow stress with decreasing nanowire diameter, with simulations by Diao *et al.* (2004); Park *et al.* (2006) supporting the findings. In thin films Espinosa *et al.* (2004) shows increasing yield stress, with decreasing film thicknesses down to $\sim$ 100 nm. Bulge tests of free standing Cu films also show yield stress depends on film thickness and passivation (Nix (1989); Lane *et al.* (2000); Nicola *et al.* (2006); Xiang and Vlassak (2006)). Columns under compression show increasing yield stress with decreasing cross sectional area as reported by Uchic *et al.* (2004). Similarly, Greer *et al.* (2005); Greer and Nix

(2005) performed compression tests on Au nanopillars, seen in Figure 1.1 and reported increases in yield stress and flow stress with decreasing pillar diameter. Recently nanoindentation of single crystals have also shown size-scaling for nm length scales (Nix and Gao (1998); Nix *et al.* (2007); Zong *et al.* (2006)) as well as fracture toughness (Lane *et al.* (2000)). Size scaling of flow stress has also been advanced by Sieradzki *et al.* (2006) and Volkert and Lilleodden (2006) in the context of the diameter of whiskers and columns.

Several models over a range of length scales have been developed to model crystalline materials and have varying success in capturing scaling. At the smallest length scales < 10 nm, models describe the nucleation of individual dislocations. Energetic considerations are used to determine critical quantities during the nucleation process. The two most significant models are the Rice-Thomson (RT), (Rice and Thomson (1974)) and Peierls-Nabarro (PN), (Rice (1992)), models, both of which are 2-D methods. While quite general, they have been applied to simple indentation by Shenoy *et al.* (2000). The RT model estimates the force per unit length, P_{cr}^{FF}, necessary for the existence of a stable dislocation at a critical distance d from the indenter. There are two competing forces acting on the dislocation: the force due to the field of the indenter, $\sigma^L(a,d)$ and the stress due to the image force attracting the dislocation to the surface, $\sigma_{xz}^d(a,d)$, where a is the radius of the indenter. Setting the equilibrium distance equal to the dislocation core radius $d = r_c$, the resulting critical pressure for nucleation is $P_{cr} = (\mu b/(1-\nu))\sqrt{a/r_c}$. The only unknown is r_c, which is estimated from atomistic simulations. This model sets a lower limit for the nucleation pressure since it only determines the equilibrium pressure, but it does predict a scaling exponent of 1/2 for the 2-D problem.

The PN method circumvents the need for a critical distance by explicitly considering the process by which the full burgers vector is created, i.e. the relative sliding of

neighboring atomic planes, and the maximum shear stress τ_{max} during that process. Nucleation occurs when the applied shear stress on the slip plane from the indenter attains the maximum value, $\sigma_{xz}^{L}(a,0) = \tau_{max}$. Analytical solutions are not trivial since the stress solution at an edge is usually singular, which is again resolved using atomistic simulations. Atomistic simulations alone, using MD methods, are also useful in modeling scaling but to this point are extremely limited by the size of the systems that can be modeled. Both the RT and PN methods become very cumbersome when the number of dislocations increases, as a series of linked equations must be solved to determine the equilibrium positions for each dislocation. Even with the more complexity with increasing numbers of dislocations recent work on a PN-type model for multiple dislocation emission from a crack tip has been successful Warner *et al.* (2007).

Another set of models combine length scales in an attempt to capture the detail of the atomistic energetics and the robustness of continuum methods. One example of this linking of length scales is the quasicontinuum (QC) method Tadmor *et al.* (1996). Many models similar to QC exist including a version that passes dislocations from the atomistics to a discrete dislocation region, described below, but much is left to be done (Shilkrot, Curtin and Miller (2002); Shilkrot, Miller and Curtin (2002); Miller *et al.* (2004)).

The discrete dislocation (DD) models developed by van der Giessen and Needleman (1995); Deshpande *et al.* (2005), remove the details associated with atomistics that are not generally necessary to capture material behavior at micro-length scales. DD models treat all dislocations as line defects in a 2-D plane strain formulation. A general DD simulation consists of an elastic body with a random distribution of dislocation sources and obstacles. Under an applied load, the stress and strain fields are solved given the current dislocation distribution. The forces on the dislocations

are then used to move the dislocations according to a mobility law, and other constitutive rules for nucleation, annihilation, and pinning/depinning at obstacles are invoked. The DD model has recently predicted size scaling for indentation at the sub-micron level, Widjaja *et al.* (2005, 2007), and for thin film yielding Chng *et al.* (2006).

Increasing the length scale further introduces an important class of models for describing size dependent plastic flow which do not account for discrete plastic entities, the strain-gradient-plasticity theories (Fleck *et al.* (1994); Fleck and Hutchinson (1997, 2001)). These models introduce a length scale and additional scale-dependent constitutive behavior into the framework of conventional plasticity theories. Just as the grain size for polycrystals sets a size scale for the deformation, the idea of scaling due to large strain gradients and geometrically necessary dislocations (GNDs)(Nix and Gao (1998)), has a microstructural characteristic length, $\hat{l}$, which scales with L^2/b where, L is the distance between dislocation obstacles and b the Burgers vector. A schematic of the GND concept is shown in Figure 1.2. By introducing the concept of GNDs, size scaling is captured for length scales of < 1 μm. The scaling for the GNDs comes from the argument that the shear strength τ is a function of the density of dislocations; $\tau = \alpha\mu b\sqrt{\rho_G + \rho_s}$ where ρ_G is the GND density, ρ_s the statistically stored dislocation density, μ the shear modulus, and α is a constant normally set to 0.5. The density is easily calculated through geometric considerations for a known amount of deformation and an assumed plastic zone volume. Since the density decreases with contact area the corresponding shear strength will decrease as well, resulting in the size scaling for indentation and other contact problems. The characteristic length scale then becomes $\hat{l} = b(\mu/\sigma_o)^2 = 4/(3b\rho_s) = 4L_s^2/(3b)$ where L_s is the distance between the statistically stored dislocations. Nix and Gao show

excellent agreement between experiments and the GND strain gradient plasticity considerations for contact edge lengths of ~ 750 nm with hardnesses of ~ 2 GPa for the indentation of Cu. Zong *et al.* (2006) reports for the indentation of Ni, Ag and Au with hardnesses $\sim 2-5$ GPa at contact edge lengths of $<\sim 750$ nm for a range of indenter geometries, with a good fit to the Nix-Gao model. The Nix-Gao model clearly fails for edge lengths < 100 nm or smaller, Qu *et al.* (2004), which is rationalized by the fact that the plastic volume in the Nix-Gao model is too small at small contact lengths.

Another key model that incorporates several components of the models already discussed has been developed by (Gerberich:05,Gerberich:06). Gerberich has attempted to capture the scaling at length scales 5 nm $< \ell <$ 500 nm by using the PN and RT models as a framework for the energetics of multiple dislocation avalanche events. Since the RT and PN models include all energies necessary to nucleate a dislocation the model is extended to multiple dislocations by predicting the work associated with dislocation motion. Since it becomes increasingly more complicated to keep track of locations for a large number of dislocations and to determine the interaction stresses associated with these dislocations, a generic description of this energy is given as: $f d\delta_{exc} = \delta W_p + \delta S + \delta U_\ell$. Here $f d\delta_{exc}$ is the external work, δW_p is the change in plastic energy, δS is the change in surface energy and δU_ℓ is the change in elastic energy. The model is minimized to determine an equilibrium contact area that will support the dislocation structures in the bulk. This model attempts to account for all of the energy associated with the process of nucleating a single dislocation loop during indentation and then apply it to multiple nucleations. To account for multiple events, approximate distance and shear stresses are used to determine the work done on moving dislocations. The model neglects specific interaction energies and uses a similar relation to that of the Nix-Gao to describe the motion and interactions over an

approximate plastic volume. Neglecting the actual interactions result in the model's inability to capture specific scaling at $\ell < 500$ nm.

While the above models fail to capture scaling for $\ell < 500$ nm recent experiments by Wang *et al.* (2006) and Nix *et al.* (2007) show a size-scaling for a length scales of 100 nm $< \ell <$ 500 nm. Wang *et al.* (2006) performed compression experiments on extremely well-characterized single-crystal Au pyramids shown in Figure 1.3 (Wang *et al.* (2006)). The hardness (contact pressure) versus contact edge length ℓ_c over the range $\ell_c \sim 100 - 600$ nm reaches peaks of] $\sim$ 2.5 Gpa and shows a scaling $H \approx \ell_c^{-0.75}$ independent of the starting contact edge length, which is slightly lower than the scaling predicted by the Nix-Gao and PN models. Independently, Nix *et al.* (2007) performed indentation experiments on a Au (100) single crystal thin film using a Berkovich indenter. This is essentially the inverse problem of the pyramid since the slope of the Berkovich indenter is almost exactly the same as that of the pyramid. The similar geometries between the two experiments results in roughly the same number of dislocations necessary to accommodate the deformation. Assuming that the deformation and high stress is local to the point of contact it is not surprising that the indentations show a scaling of $H \approx \ell_c^{0.5}$ with hardnesses of $\sim$ 2.5 GPa at $\ell_c \sim 100$ nm. These experiments now show scaling of the flow stress at a length scale $< \ell <$ 500 nm that is not captured by any of the models presented above.

This work examines two important systems introduced above: i) Al-Si nanocomposites under tension, ii) Au nano-asperities under compression. Nanocomposites as mentioned are the next natural progression in the study of nanograin materials. With single phase nanomaterials primarily understood it is important to understand the influence of introducing a second phase. In this case Al-Si is chosen because it is a material of interest for the automotive industry. In composite systems, the role of bi-material interfaces can be predominant, and so the work begins with a detailed study

of the deformation, strength, and fracture energy of a set of Al-Si interfaces having various orientations. The work then turns to the Al-Si nanocomposites and examines elastic response, plastic deformation mechanisms and failure processes as well as making comparisons to Al polycrystals all with the goal of understanding how to enhance the macroscopic behavior of the composite. Au asperities, on the other hand, are important because they represent the smallest defects of generally rough surfaces. These surfaces could belong to large gears in a turbine or small electrical contacts but either way the properties of the surface are important in predicting system behavior. Previous experiments have been performed which capture hardness scaling for $\ell < 500$ nm which offers the unique opportunity to compare atomistic models with experiments. This work studies the compression of extremely well-characterized nanoscale asperities in the form of Au pyramids, similar to those of the Wang experiments, using large-scale molecular dynamics simulations. The simulations are extensive, not only including large sizes, large initial contact lengths, and large depths of indentation, but also including variations in temperature and stacking fault energy (by using different interatomic potentials). The MD simulation also allows for the deformation mechanisms to be determined through visualization. To understand the size scaling, and the origin of possible differences between the MD and experiment, we propose an energy-based model, using the deformation mechanisms from the MD, to predict a lower limit for the hardness versus contact size, similar to that of Gerberich et al. Each component of the energy is examined to determine what specifically dominates the scaling at different length scales. The nanoasperity study thus establishes a basis for the hardness scaling for $\ell < 500$ nm.

The rest of the thesis is presented as follows. Ch. 2 contains a comprehensive review Molecular Dynamics and interatomic potentials. Followed by the MD simulations of Al/Si interface in Ch. 3 including strength and toughness analysis. In Ch. 4

the Al/Si study is extended to the deformation and failure of nanocomposites. The work then shifts the the Au nanoasperities with Ch. 5 focusing on the MD simulations. Ch. 6 will then take the information gained from the MD and present the basis for an energetic model to predict the hardness of the asperity compression. Finally closing remarks will be made in Ch. 7.

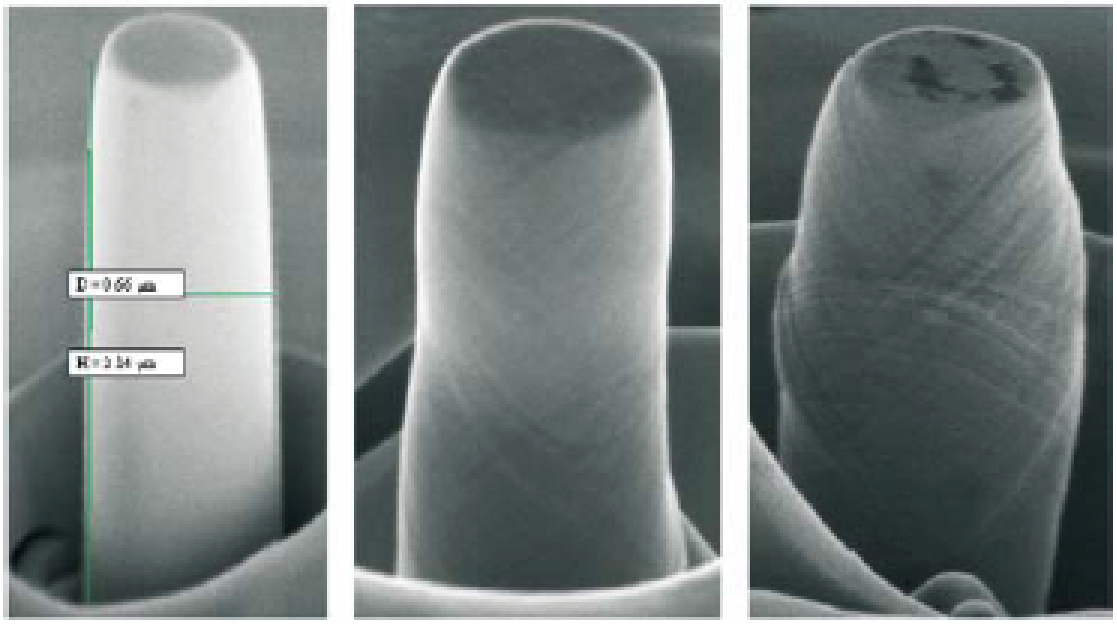

Figure 1.1: Compression of nano pillars performed by Greer et al. Clear dislocation bands appear at late stages of compression, Greer and Nix (2005).

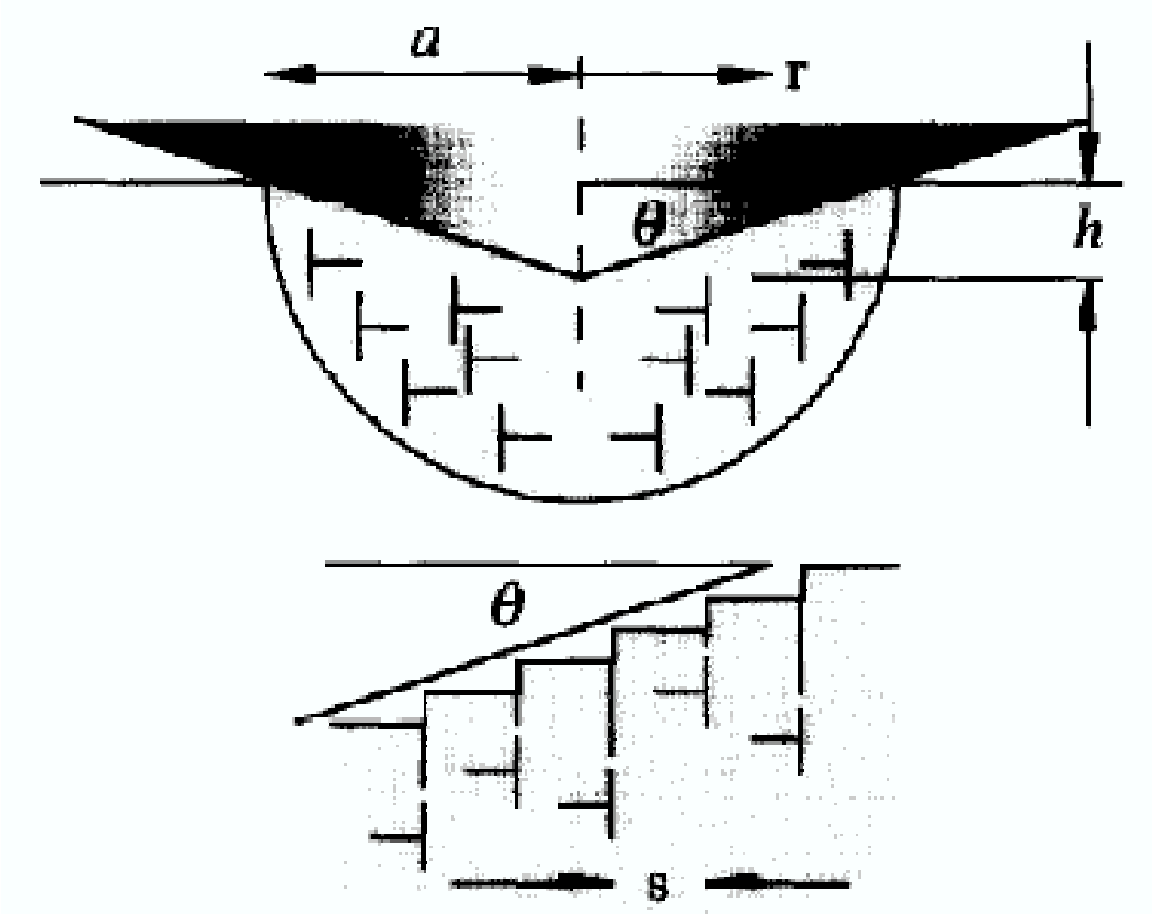

Figure 1.2: Schematic of the generation of geometrically necessary dislocations (GNDs) during an indentation process taken from Nix and Gao (1998).

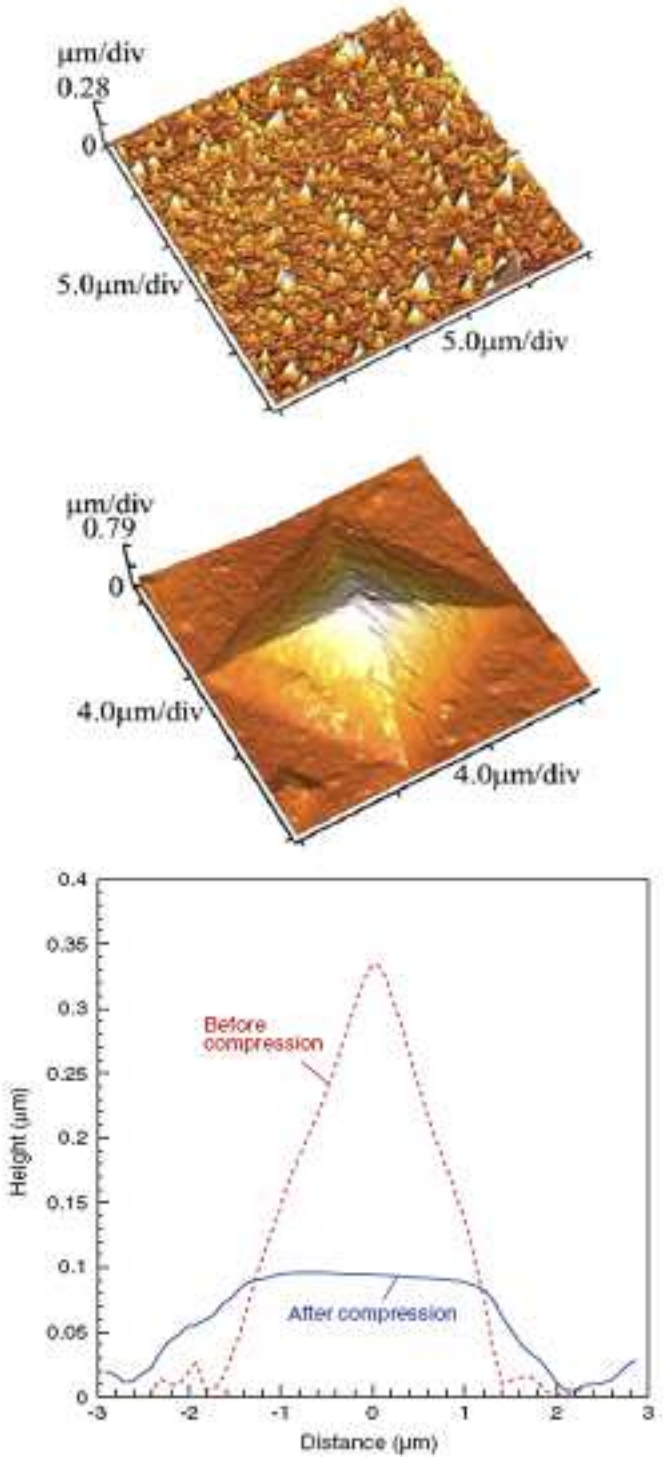

Figure 1.3: a)AFM image of pyramid array on (001) Au single crystal surface; b) single pyramid with (114) facets; c) Pyramid profile before and after compression by a flat mica indenter. From experiments performed by Wang *et al.* (2006).

Chapter 2

Simulation Details

2.1 Atomic Potentials

In nanoscale systems, e.g. nanocomposites and nanoasperities, molecular dynamics is used to study the atomic response to exterior loading. Molecular dynamics (MD) is a method used to describe the motion of individual atoms using Newton's equations of motion in some iterative process over a desired time, t, at a given time increments, dt. The ultimate desired outcome of MD is the new atomic positions of an atomic configuration under some external influence, whether that be a load, temperature or any number of other effects. In order to progress the atomic positions and velocities, the forces acting on a single atom must be accurately described. Many methods have been proposed to describe these forces.

The earliest methods used to describe fluid motion were generic potentials called Lennard-Jones (LJ) potentials which determined the total energy of a system with two simple terms attributed to the repulsion and attraction of particles (Allen and Tildesley (1989)). A simple example and probably the most common form is called

a LJ 6-12 potential and is expressed as:

$$V = \sum_i \sum_{j>i} v^{LJ}(r_{ij}) = \sum_i \sum_{j>i} 4\epsilon \left[\left(\frac{\sigma}{R_{ij}} \right)^{12} - \left(\frac{\sigma}{R_{ij}} \right)^{6} \right] \tag{2.1}$$

where V is the total energy of the system and v^{LJ} is the individual contribution to the energy for each atom i and j interaction at a spacing of R_{ij}. The energy of the interaction between atoms i and j are summed up for the entire system to give a total energy. For this potential, ϵ is the energetic minimum for a single atom-to-atom interaction which leads to an equilibrium atomic spacing of σ. As mentioned the potential has two competing terms, the attractive term and the repulsive term; at distances R greater than the equilibrium spacing, $R > \sigma$, the potential is attractive while at $R < \sigma$ the potential is repulsive. The force on i from j is determined by simply taking the derivative of the energy with respect to the atom spacing, $f_{ij} = dv_{ij}^{LJ}/R_{ij}$.

2.1.1 Embedded Atom Method

LJ potentials give a clear picture of the atomistic attractive and repulsive nature but lack the detail necessary to effectively predict the more complicated electron fields in metallic interactions. The most widely accepted inter-atomic potential used for metallic materials is the Embedded Atom Method (EAM), developed by Foiles *et al.* (1984, 1986); Daw and Baskes (1983, 1984). For the Au nanoasperities, to model the Au-Au interaction, two different potentials are implemented, Auu3 (Foiles *et al.* (1986)) and Au2, (Park and Zimmerman (2005)). The EAM potential is slightly more complicated than LJ because of an additional term which accounts for the background electron density at a given atom location in addition to the pair interaction between

atoms. EAM determines the total energy of the system as

$$E_{tot} = \sum_i F_i(\rho_{h,i}) + \frac{1}{2}\sum_i \sum_{j(\neq i)} \phi_{ij}(R_{ij}) \tag{2.2}$$

The two important aspects of the energy are: $F_i(\rho_{h,i})$ the energy necessary to embed an atom into a host electron density $\rho_{h,i}$, and $\phi_{ij}(R_{ij})$ the pair potential between atoms i and j at a distance R_{ij}. The host electron density is defined as the superposition of the density for each atom,

$$\rho_{h,i} = \sum_{j(\neq i)} \rho_j^a(R_{ij}) \tag{2.3}$$

where the density for each atom is defined using Hartree-Fock wave functions (Clementi and Roetti (1974); McLean and McLean (1981)) as $\rho^a(R) = n_s\rho_s(R) + n_d\rho_d(R)$. Here, n_s and n_d define the number of electrons in the s and d orbitals respectively. The total number of outer electrons is fixed which results in only n_s as an adjustable parameter for the embedding function. For the Au2 potential, the electron density is defined as $\rho(R) = R^8(e^{-\beta_M R} + 2^{11}e^{-2\beta_M R})$ while for the Auu3 potential this function is fit to an atomic configuration of $5d^{10}6s^1$. In the former expression, β_M is a fitting parameter for the function. The pair potential, on the other hand, is more easily described using the effective charges, $\phi_{AB} = Z_A(R)Z_B(R)/R$, of atom types A and B which allows for the analysis of alloys. The effective charge is assumed to take the form $Z(R) = Z_0(1 + \beta R^{nu})e^{-\alpha R}$ where Z_0 is the number of outer electrons and α, β and ν are left as adjustable parameters. These functional forms with five adjustable parameters n_s, β_M, α, β and ν, are then fit to several bulk constants: the sublimation energy, lattice constant, elastic constants, vacancy-formation energy, and the internal energy for the specified elements. While the methods of determining the potentials are similar, the values of the fitting parameters are slightly different and Au2 is also fit to the stacking fault energy. The values of the most important constants for this

Table 2.1: Lattice constant a_o, cohesive energy E_o, bulk modulus B, elastic constants C and stacking fault energy γ_{sf} as predicted by the Auu3 and Au2 potentials compared with the experimental values

	a_o(Å)	E_o(eV)	B(GPa)	C_{11}(GPa)	C_{12}(GPa)	C_{44}(GPa)	γ_{sf} (mJ/m^2)
Auu3	4.08	3.93	167	183	159	45	4.71
Au2	4.08	3.93	166.67	185.8	157.1	38.949	31
Exp	4.08	3.93	166.67	186	157	42	32

study are listed in Table 2.1.1 for both potentials. Using these potentials yield elastic constants for the (001) orientation of $E = 35.5$ GPa, $\mu = 45$ GPa and $\nu = 0.46$ for Auu3 and $E = 42$ GPa, $\mu = 39$ GPa and $\nu = 0.46$ for Au2. It is not the differences in the elastic constants for the (001) orientation as well as the large discrepancy between the stacking fault energies in Table 2.1.1. The Elastic properties for these potentials are confirmed in Ch. 5.

2.1.2 Modified Embedded Atom Method

EAM models the interactions for metals very well but has some limitations. For materials that have direction-dependent bonding, a more complicated description of the energy is required. Initial direction-dependent potentials introduced an energy penalty for bond angles between three atoms at nonpreferable orientations (Phillips (2001)). For this study the Modified Embedded Atom Method (MEAM) is used to describe the interatomic interactions between Al-Al, Si-Si, and Al-Si (Baskes (1992); Lee *et al.* (2003)). This potential is similar to the more common EAM potentials but does allow for the directional dependence of the Si bonding; details of the agreement between MEAM and experimental and ab-initio calculations are contained in Baskes (1992); Lee *et al.* (2003); Daw and Baskes (1984). MEAM not only predicts the bulk properties of Si but can also predict the experimentally observed 7x7 DAS reconstruction of Si(111) as the most stable structure among other NxN DAS structures

(Takahashi *et al.* (1999)).

MEAM defines the energy E of the system as the sum of energies for each atom i, having energy contributions from an embedding function F that depends on a local electron density $\bar{\rho}_i$, and a pair potential ϕ, so that

$$E = \sum_i \left[F(\bar{\rho}_i) + \frac{1}{2} \sum_{j(\neq i)} \phi(R_{ij}) \right], \quad F(\bar{\rho}_i) = AE_c \frac{\bar{\rho}_i}{\bar{\rho}^o} \ln \frac{\bar{\rho}_i}{\bar{\rho}^o} \tag{2.4}$$

where A is a constant, E_c is the cohesive energy, and $\bar{\rho}^o$ is a reference electron density. The pair potential only depends on the distance between atoms i and j, R_{ij}. The actual angular dependence of the potential is buried in the definition of $\bar{\rho}_i$, which represents the electron density at atomic site i. The electron density is determined using

$$\bar{\rho}_i = \rho_i^{(o)} \sqrt{1 + \Gamma_i} \tag{2.5}$$

with

$$\Gamma_i = \sum_{k=1}^{3} t^{(k)} \left(\frac{\rho_i^{(h)}}{\rho_i^{(o)}} \right)^2 \tag{2.6}$$

where t is an adjustable parameter used to weight directional dependence, $\rho_i^{(o)}$ is a spherically symmetric term, and the $\rho_i^{(h)}$ represent the angular dependent terms of

the electron density as

$$
\begin{aligned}
(\rho_i^{(o)})^2 &= \sum_{j\neq i} \rho_i^{a(o)}(R_{ij}) \\
(\rho_i^{(1)})^2 &= \sum_{\alpha} \left[\sum_{j\neq i} \rho_i^{a(1)}(R_{ij}) \frac{R_{ij}^{\alpha}}{R_{ij}}\right]^2 \\
(\rho_i^{(2)})^2 &= \sum_{\alpha,\beta} \left[\sum_{j\neq i} \rho_i^{a(2)}(R_{ij}) \frac{R_{ij}^{\alpha} R_{ij}^{\beta}}{R_{ij}^2}\right]^2 - \frac{1}{3}\left[\sum_{j\neq i} \rho_i^{a(2)}(R_{ij})\right]^2 \\
(\rho_i^{(3)})^2 &= \sum_{\alpha,\beta,\gamma} \left[\sum_{j\neq i} \rho_i^{a(3)}(R_{ij}) \frac{R_{ij}^{\alpha} R_{ij}^{\beta} R_{ij}^{\gamma}}{R_{ij}^3}\right]^2 - \frac{3}{5}\sum_{\alpha}\left[\sum_{j\neq i} \rho_i^{a(3)}(R_{ij}) \frac{R_{ij}^{\alpha}}{R_{ij}}\right]^2
\end{aligned}
\tag{2.7}
$$

where

$$
\rho^{a(h)}(R_{ij}) = \exp\left[-\beta^{(h)}(R_{ij}/r_e - 1)\right] \tag{2.8}
$$

is the electron density from a neighboring atom at a distance R_{ij} from the atom of interest. The α, β, and γ variables are summed over the three directional components of the distance vector between atoms i and j.

The initial versions of MEAM which only determined energies between first nearest neighbors (1NN) contained many problems. It was determined early in the development of the MEAM that for body centered cubic (bcc) structures there were other structures with lower energies and that surface energies of common orientation (100), (110) and (111) were not close to the experimental values (Lee *et al.* (2001)). It was determined that by simply including the second nearest neighbors (2NN) MEAM could again correctly predict the low energy structure, and surface energies were much closer to expected values. Shortly there after similar problems arose in face centered cubic (FCC) structures, such as Al. MEAM actually predicted the hexagonal close packed (hcp) atomic structure as more stable than FCC (Lee *et al.* (2003)). Early simulations performed with older versions of MEAM potentials did show under tension FCC Al would transform fairly quickly to an hcp structure. Including the 2NN

interactions with a screening function resolve these issues. The screening function accounts for the interaction of a 2NN considering a 1NN can be in between the nucleus and 2NN. The values of the elastic constants for this potential were not confirmed here.

2.2 Molecular Dynamic Details

Molecular dynamics is an excellent tool to model atomic motion using the potentials established above. Unlike molecular statics (MS), which uses energy minimization to find an equilibrium structure (i.e. Congegate Gradient Methods), MD uses the forces and velocities to step the atom motions forward in time. Many different software packages exist to perform these types of simulations ranging from basic Fortran codes written by graduate students to commercial codes with gui interfaces. Here two different codes are used to run the simulations: Baskes' own MEAM code for the Al-Si calculations and the Large-scale Atomic/Molecular Massively Parallel Simulator (LAMMPS) for the much larger Au asperity simulations. Besides the different potentials, the dynamics machinery is primarily the same, consisting of an integrator to step the simulation in time and a thermostat/barostat to control the important environmental/boundary conditions.

Atomic positions are determined by integrating the equations of motions numerically. Many different methods of integrating these equations exist with varying degrees of precision and effectiveness. The basic integrators for MD generally take the current positions, velocities, and forces to determine the positions and velocities after an increment in time, Δt, using Newton's equations of motion. Different methods are used here for the two different MD packages. For the simulations here a Nordseick integrator (Nordsieck (1962); Beeler Jr. (1983)) is implemented for the MEAM potential and the Verlet integrator (Verlet (1967)) for the EAM potential, each using a

time step of 1 fs.

The Nordsieck integrator is a scheme that requires a large amount of memory to integrate the equations of motion which is not ideal for larger systems but is sufficient for the Al/Si simulations. The first step is to determine the first five scaled time derivatives of the atom coordinate $\mathbf{x}(t)$ as:

$$\begin{aligned}
\mathbf{v}_1 &= (d\mathbf{x}/dt)\Delta t, \\
\mathbf{v}_2 &= (\frac{1}{2})(d^2\mathbf{x}/dt^2)(\Delta t)^2, \\
\mathbf{v}_3 &= (\frac{1}{6})(d^3\mathbf{x}/dt^3)(\Delta t)^3, \\
\mathbf{v}_4 &= (\frac{1}{24})(d^4\mathbf{x}/dt^4)(\Delta t)^4, \\
\mathbf{v}_5 &= (\frac{1}{120})(d^5\mathbf{x}/dt^5)(\Delta t)^5
\end{aligned} \tag{2.9}$$

Which are then used to predict the positions and derivatives at time $(t + \Delta t)$ as:

$$\begin{aligned}
\mathbf{x}(t+\Delta t) &= \mathbf{x}(t) + \mathbf{v}_1 + \mathbf{v}_2 + \mathbf{v}_3 + \mathbf{v}_4 + \mathbf{v}_5, \\
\mathbf{v}_1(t+\Delta t) &= \mathbf{v}_1(t) + 2\mathbf{v}_2(t) + 3\mathbf{v}_3(t) + 4\mathbf{v}_4(t) + 5\mathbf{v}_5(t), \\
\mathbf{v}_2(t+\Delta t) &= \mathbf{v}_2(t) + 3\mathbf{v}_3(t) + 6\mathbf{v}_4(t) + 10\mathbf{v}_5(t), \\
\mathbf{v}_3(t+\Delta t) &= \mathbf{v}_3(t) + 4\mathbf{v}_4(t) + 10\mathbf{v}_5(t), \\
\mathbf{v}_4(t+\Delta t) &= \mathbf{v}_4(t) + 5\mathbf{v}_5(t), \\
\mathbf{v}_5(t+\Delta t) &= \mathbf{v}_5(t)
\end{aligned} \tag{2.10}$$

These are not the correct values of the positions and derivatives but simply a prediction which is now used to compute the new force $\mathbf{f}(t + \Delta t)$ and a displacement function, $\Phi = (1/2)(\mathbf{f}/m)(\Delta t)^2 - \mathbf{v}_2(t + \Delta t)$. With these values the new corrected

positions and derivatives are calculated using:

$$\begin{aligned} x^c(t+\Delta t) &= x(t+\Delta t) + c_0\Phi, \\ v_n^c(t+\Delta t) &= v_n(t+\Delta t) + c_n\Phi \end{aligned} \tag{2.11}$$

where $n = 1, 2, ...5$ and the constants c_n depend on the order to which the scheme is taken (in this case 5th order) and are 3/16, 251/360, 1, 11/18, 1/6 and 1/60 for $c_0 - c_5$ respectively. The Nordsieck method does not loss stability or accuracy during incrementation.

For the pyramid simulations, a specific type of Verlet integrator called velocity Verlet is implemented to integrate the equations of motion. The positions and velocities for an increment of dt is given by:

$$\mathbf{x}(t+dt) = \mathbf{x}(t) + dt\mathbf{v}(t) + \frac{1}{2}dt^2\mathbf{a}t \tag{2.12}$$

and

$$\mathbf{v}(t+dt) = \mathbf{v}(t) + \frac{1}{2}dt[\mathbf{a}(t) + \mathbf{a}(t+dt)] \tag{2.13}$$

Notice in the expression for $\mathbf{v}(t+dt)$, the accelerations for t and $t+dt$ are required. This implies that there must be an intermediate force calculation between Eq 2.12 and Eq 2.13. This intermediate force calculation is performed using the positions determined from Eq 2.12. An intermediate velocity is also determined just before the force calculation by:

$$\mathbf{v}(t+\frac{1}{2}dt) = \mathbf{v}(t) + \frac{1}{2}dt\mathbf{a}(t) \tag{2.14}$$

Calculating an intermediate velocity saves on storage space, requiring storage of only one acceleration rather than two. Once the forces and thus accelerations are calculated

the final portion of the velocity is determined using:

$$\mathbf{v}(t+dt) = \mathbf{v}(t+\frac{1}{2}dt) + \frac{1}{2}dt\mathbf{a}(t+dt) \tag{2.15}$$

which is nothing more than the same expression from Eq 2.13. These integrators are excellent for progressing the atomic structure in time but will only result in systems with conserved energy. For all simulations 0.001 ps is used for the time increment.

For the simulations performed here, conserving energy is not the most desirable method of dynamics. Here we would like to define the pressure and temperature (NPT dynamics) so it is necessary to implement tools to control these values. The Nose/Hoover barostat and thermostat are the most common method of control for the environmental parameters of the system (Nose (1984); Hoover (1985); Allen and Tildesley (1989)). The thermostat is created by allowing energy to flow to a large reservoir which adds an extra degree of freedom, s, to the simulation with a corresponding momentum, p_s. The atomic velocities are then related to the position time-derivatives by $\mathbf{v} = s\ d\mathbf{x}/dt$. The new degree of freedom is extended to the potential and kinetic energy and changes the equations of motion to dampen out extra energy which would ultimately result in a lower temperature. The new equations of motion are

$$\ddot{\mathbf{x}} = \frac{\mathbf{f}}{ms^2} - \frac{2\dot{s}\dot{x}}{s} \tag{2.16}$$

$$Q\ddot{s} = \sum_i m\dot{x}_i^2 - (f+1)\frac{k_B T}{s} \tag{2.17}$$

where $\mathbf{f}$ is the force on the atom, m is the mass, Q is the thermal inertia parameter or the damping coefficient. Also, f is the number of degrees of freedom for N atoms $(3N-3)$, T is the desired temperature and k_B is the Boltzmen constant.

With an effective method for controlling the temperature, the pressure can now be addressed. The best method for constraining the pressure is to adjust the volume

of the simulation box to relieve or induce pressure. To do this, a Lagrange multiplier χ is introduced which represents the rate of dilation of the system. Combining the temperature and pressure constraints results in new equations of motion:

$$\begin{aligned}
\dot{\mathbf{s}} &= \mathbf{p}/mV^{1/3} \\
\dot{\mathbf{p}} &= \mathbf{f} - (\chi + \xi)\mathbf{p} \\
\dot{\xi} &= \left(\sum_i \mid \mathbf{p}_i \mid^2 /m - f k_B T \right) /Q \\
\chi &= \dot{V}/3V \\
\dot{\chi} &= (\wp - P)V/t_P^2 k_B T
\end{aligned} \tag{2.18}$$

where V is the volume of the simulation $\wp$ is the instantaneous pressure, t_p is a relaxation parameter for the fluctuations of the pressure and ξ is another Lagrange multiplier defined as:

$$\xi = \left(\sum_i \mathbf{p}_i \cdot \mathbf{f}_i \right) / \left(\sum_i \mid \mathbf{p}_i \mid^2 \right) \tag{2.19}$$

With these new equations of motion the pressure and temperature are effectively controlled and the fluctuations due to the dynamics are damped using the Q and t_s values. Trial and error is used to determine which values of the constants converge the energy, temperature and pressure of the system in the fewest time steps. These values used for each particular simulation are stated later in the thesis.

2.3 Measures of Deformation and Stress

Three important parameters used in the analysis of molecular dynamics systems are Centro-Symmetry, Effective Strain and the Virial Stress. Centro-symmetry is a parameter used to determine the local strain an atom undergoes and is also a way to

locate stacking faults and dislocations. Centro-Symmetry is defined as:

$$C = \sum_{j=1,6} \mid R_{ij} + R_{ij+6} \mid^2 \tag{2.20}$$

where R_{ij} and R_{ij+6} are the vectors from the atom of interest, i, to the 12 nearest neighbors of that atom in an FCC structure. The vectors are paired such that R_{ij} and R_{ij+6} are the six pairs of opposite atoms and result in a measure of the local deformation about the object atom, since the only time the result is non zero occurs when deformation is nonhomogenous (Kelchner *et al.* (1998)). For a perfect lattice this value is 0 $\mathring{A}^2$. Kelchner has shown that the centro-symmetry captures the departure from a perfect FCC lattice in shear and that the value ranges from $0.5 - 4$ $\mathring{A}^2$ for partial dislocations, $4 - 20$ $\mathring{A}^2$ for stacking faults and > 20 $\mathring{A}^2$ represents surface atoms.

To visualize the deformation mechanisms in various materials, we analyze the local effective strain field throughout the material, using the following effective strain mapping method. As an example the method will be described for the nanocomposite Al/Si which lends itself to the method well since it is essentially a 2D system. First, a two-dimensional projection of the first two (011) planes of atoms in the unstrained state are used as nodes to create a triangular mesh of elements, with some atoms near the grain boundary removed to ensure that all elements have sizes on the order of the atomic spacing. Under an applied strain, each atom displaces by some amount $\mathbf{u}$ and the corresponding elements deform as characterized by the deformation gradient $\mathbf{F} = \mathbf{I} + \nabla\mathbf{u}$. The Lagrangian strain tensor $\mathbf{E} = 1/2(\mathbf{F}^T\mathbf{F} - \mathbf{I})$, is then calculated and the effective strain $E_e = 1/2\left[(E_1 - E_2)^2 + E_1^2 + E_2^2\right]^{1/2}$ is determined from the principle values of the Lagrangian strain, $\{E_i\}$. The effective strains for elements having atom nodes that deform elastically are on the order of the macroscopic strain, i.e. much smaller than the strain associated with a stacking fault. However, the

effective strains for elements in which the atom nodes slide relative to one another, either by dislocation motion or grain boundary motion, are very large, on the order of 100%. Thus, a contour map of the effective strain clearly shows both dislocation motion, appearing as straight lines traversing a grain corresponding to the dislocation slip, and grain boundary sliding-like phenomena, appearing as irregular deformation along the grain boundaries.

Virial stress is a parameter used to quantify the stress a single atom is experiencing (McLellan (1974)) and is defined as:

$$\sigma_{\alpha\beta} = \frac{1}{\Omega} \sum_i \left(-m^{(i)}(v_\alpha^{(i)} - \bar{v}_\alpha)(v_\beta^{(i)} - \bar{v}_\beta) + \frac{1}{2} \sum_j (x_\alpha^j - x_\alpha^i) f_\beta^{ij} \right) \tag{2.21}$$

where Ω is the volume of a region containing i atoms and α and β define the Cartesian components of stress. The stress consists of two components; first, a dynamic portion defined by the mass $m^{(i)}$, velocity $v_\alpha^{(i)}$ of atom i and the local velocity $\bar{v}_\alpha$, and finally a static portion consisting of the atomic positions of atoms i and j, $x_\alpha^{(i)}$, and the force between atoms i and j, f_β^{ij}. For many cases the dynamic portion is much smaller than the portion defined by the forces between atoms (e.q. the models studied here) so the velocity portion is neglected. In this instance the interpretation of the local stress must be approached with caution but the virial stress gives a reasonable expression for a macroscopic stress value.

Chapter 3

Al/Si Interfaces: MD Study

With single phase nanomaterials primarily understood it is important to understand the influence of introducing a second phase into the system. Here Al-Si composites are chosen to study the influence of introducing a ceramic particle into a metal polycrystalline material. Al-Si is chosen because it is a material of interest for the automotive industry. Recent experimental work by some automotive companies have focused on Al-Si as an attractive coating material (Olk and Haddad (2006),Olk *et al.* (2006). In composite systems, the role of bimaterial interfaces can dominate the strength and failure, and so the work on composites begins with a detailed study of the deformation, strength, and fracture energy of a set of Al-Si interfaces having various orientations. Highly mismatched Al/Si interfaces show good tensile strength and significantly enhanced fracture energy relative to structurally-well-matched interfaces, suggesting the possibility that nanocomposites can have good strength and toughness.

3.1 Al-Si Interface Structures

The interface geometries are generated by creating one slab of each material, using the zero-temperature lattice constant, with the desired surfaces and placing them in contact with one another, as shown in Figure 3.1. Al/Si systems are excellent for use in periodic MD simulations because their lattice constants, 4.041 $\mathring{A}$ for Al and 5.42 $\mathring{A}$ for Si, have a near perfect 4 to 3 relationship which lends itself perfectly to a repetitive periodic system. For these simulations in order to maintain a perfect cubic structure for each element type as well as periodicity in the z-direction a [110] crystalligraphic orientation with a 11.45 $\mathring{A}$ thickness is chosen. This requires the Si slab to consist of six atomic layers while there are eight atomic layers for the Al slab. The length in the y-direction (perpendicular to the [110] z-direction and the interface normal) is varied in each case until the lattice mismatch between the two elements is accommodated and periodic boundary conditions can be applied in the y-direction. It is important to use a [110] z-direction to optimize the plasticity and slip systems available for plasticity. A [110] z-direction gives for active slip systems that are perpendicular to the thin z-direction. If the slip systems are not perpendicular to the periodic thickness slip will propegate itself through the periodicity and interact with itself unrealistically. The x-direction is normal to the interface and is the direction of the prescribed displacement. Periodic boundary conditions are not implemented in the x-direction. The interface model is then relaxed using molecular statics (T=0K), holding the two ends along the x-direction fixed while the y- and z-directions are allowed to translate, to create the bonded interface. The system is then annealed at a temperature of 300 K for 20 ps, with damping coefficients of $Q = 1$ and $t_s = 0.1$. With fixed ends, the annealing creates a residual tensile stress along the loading axis x. From this state, the sample is deformed by holding one end of the sample fixed and displacing all remaining atoms in increments of 1% strain from their current positions,

and relaxing the system using Molecular Dynamics at the prescribed temperature, 300 K, for 20 ps after each strain increment.

3.2 Interface Maximum Tensile Strength

This study investigates nine different interfaces, ranging from well-matching Al(111)/Si(111) to highly mismatched Al(113)/Si(335). We calculate a stress-strain curve for each interface sample, which consists of an initial linear region followed by some slight fluctuations associated with thermal activity leading up to a rapid post-peak decline, but it has little importance because the response is associated with the relative lengths and moduli of the two phases in the loading direction. The property of interest is the maximum tensile strength σ_T, i.e. the peak of the stress-strain curve, which we have extracted from the data and shown in Table 3.1; σ_T varies from 3.9-7.4 GPa among the different interfaces. Figure **??** shows the corresponding fracture surfaces. The fracture surfaces show three basic types of failure: (1) near perfect cleavage of the Al surface with small amounts or no Al sticking to the Si surface (interfaces B, D, and F), (2) significantly rough Al interface with Al sticking to the Si surface and no dislocation activity (interfaces E, G, H), and (3) significantly rough Al interface with sticking to the Si surface and dislocations emitted from the interface into the Al slab (interfaces A and C). The two highest tensile strengths B and C are not of the same failure type and the interfaces with lower strengths can have any type of fracture surface, and so the tensile strength does not correlate directly with the failed surface morphology and method of failure.

Several factors conspire to establish the tensile strength. The most important factor is the interfacial bonding, which is related to the orientations of both Al and Si and to the lattice mismatch. Since Al has more-uniformly distributed metallic bonds while Si has more-directional covalent bonds, the Al/Si interfacial bonding

Table 3.1: Al/Si bimaterial interface orientations and tensile strengths.

Interface	Al Surface	Si Surface	σ_T (GPa)
A	100	100	6.4
B	111	111	7.2
C	100	111	7.4
D	111	100	5.6
E	110	100	5.3
F	111	112	5.0
G	113	335	3.9
H	221	113	4.8
I	110	331	4.1

is mainly determined by the orientation and dangling bonds at the Si surface as shown by Baskes *et al.* (1994) and Gall *et al.* (2000). The Si surfaces, cleaved along different orientations, vary in the amount of dangling bonds and surface roughness. Si (111) has one dangling bond per atom per surface unit cell, resulting in an atomic density of $0.078/\mathring{A}^2$. The surface densities are defined as the number of atoms with dangling bonds in each surface unit cell before any surface reconstruction. In the case of Si (111) there are two atoms with dangling bonds per unit cell with area of $a/\sqrt{2} \times \sqrt{3}a/\sqrt{2}$, where a is the lattice parameter, resulting in a density of $\sqrt{3}/a^2 = 0.078/\mathring{A}^2$. Continuing with the other surface densities: Si(100) has two dangling bonds per atom and atomic density of $0.0675/\mathring{A}^2$; Si(112) has atomic steps on the surface with two atoms per unit cell, one atom having one dangling bond and the other having two dangling bonds, and an atomic density of $0.055/\mathring{A}^2$; Si(113) has one atom with two dangling bonds per cell, and an atomic density of $0.041/\mathring{A}^2$; Si(331) has 2 atoms per surface unit cell, each one has one dangling bond, and an atomic density of $0.062/\mathring{A}^2$; Si(335) has three atoms in the unit cell, two have one dangling bond and one has two dangling bonds, and an atomic density of $0.062/\mathring{A}^2$. Si(111) surface thus has the highest atomic density with all dangling bonds normal

to the surface. With high number of bonds that are normal to the interface they tend to attract Al atoms in a normal direction with out creating high stress concentrations and so the interface of Al/Si(111) is generally smooth and uniform. The strongest interfaces B and C consist of Si(111) surfaces, with strengths of 7.2 and 7.4 GPa respectively, and the interfaces with Si(111) have the least adhesive transfer. In contrast, although the Si(100) surface is one of the denser surfaces, some atoms have two dangling bonds along the cleaved surface forming 35^o angles with the surface. With two bonds available at an angle many irregular bonds between the Al and Si will occur including two Si atoms bonding with a single Al atom leaving some Al atoms without shared bonds with the Si interface. This creates weaker and non-uniform interfaces: interfaces with Si(100) (A, D, E) have strengths in the range of 5.3-6.4 GPa. The remaining interfaces created with the rougher and less dense Si surfaces (F, G, H, I) are the weakest, with strengths between 3.9-5.0 GPa. These rough surfaces would normally reconstruct to minimize the surface energy but due to the introduction of the Al surface small voids are created at the interface before annealing. When the interface is annealed at 300K Al atoms migrate to fill the voids present at the interfaces, creating stress concentrations in the Al. These stress concentrations lead to premature failure of the interface and cause more adhesive transfer of Al to Si surfaces. Only motion of Al atoms at the interface are seen during relaxation. There are not dislocations from the slabs moving to the interface, since they are created perfectly clean, nor are there dislocations nucleated from the interface during relaxation.

Another factor determining the strength of the interfaces is the orientation of the Al(111) planes with respect to the direction of the applied load. Most of the failures occur by separation of Al(111) planes, either from one another or along the Si interface. Hence, if the Al(111) planes are perpendicular to the loading then the

stresses required to cause failure are lower than if these Al(111) planes are rotated away from perpendicular with respect to the loading axis. The stronger of the two interfaces with Si(111), C, has the Al(111) planes rotated with respect to the loaded direction. The effect of the orientation of Al(111) is even more dramatic in the case of interfaces A and D: A is stronger by 0.8 GPa with the exact same Si structure at the interface. The rotated Al(111) planes have less importance when the Si surface is extremely rough. When the Si surface is rough, the more important factor is how well the Al matches with the Si surface. In comparing cases H and G, the Si surfaces have a similar roughness but G has an Al(113) surface that is relatively smooth compared to that of the Al(221). However, the match of the flat Al(113) with the rough Si (335) creates an interface with several stress concentrations while the peaks on Al(221) fit almost perfectly into the troughs of the Si(113). Therefore, interface H has smaller local stresses and a strength 0.9 GPa higher than G.

Overall, the combined effects of the Al(111) orientations and Si surface orientations and topologies are consistent with the observations that (i) the strongest interface is C, consisting of the Al (100) interface with rotated Al (111) planes and a Si (111) interface with its tightly packed and low bond initial structure, the two best possibilities, and (ii) the weakest interface is G, comprised of the Al (113) surface and the Si (335) surface which has a high number of dangling bonds and significant cavities at the interface. All other interfaces are some combination of the strengths and weakness in the bonding leading to intermediate tensile strengths.

3.3 Interface Fracture Energy

Another important aspect of the interface failure is the fracture energy, since polycrystalline fracture requires propagation of a crack in addition to crack nucleation. Three components comprise the total energy for the failed interface simulation: the

bulk energy of each of the slabs; the energy associated with the fixed-end boundary conditions; and the fracture surface energy. Of interest is the fracture surface energy versus the clean surface energy and the fracture surface work of separation W_S compared to the Griffith work of separation W_G.

The surface energies can be calculated very easily from the simulation cells given knowledge of the bulk cohesive energy E^{α}_{COH} of each atom type α. A block of the desired material is created with all directions periodic except x, which has free surfaces of the desired orientation (ijk). The total energy E_T of such a system consists of the bulk cohesive energy of the slab $E^a_B = N^a E^{\alpha}_{COH}$ and the total surface energy $\gamma^{\alpha}_{(ijk)}$, with N^{α} the number of atoms of type α. The surface energy per unit area is then

$$\bar{\gamma}^{\alpha}_{(ijk)} = (E_T - E^{\alpha}_B)/2A \tag{3.1}$$

where A is the total area associated with the projection of the free surface onto the simulation cell, i.e. the y-z planar area. The total clean surface energy for the Al-Si system, $\gamma = (\bar{\gamma}^{Al}_{(ijk)} + \bar{\gamma}^{Si}_{(lmn)})$, gives the total energy of the two surfaces per unit area. The fractured surface energy cannot be determined in the same manner as the perfect surfaces because the energies associated with the fixed ends in the simulation, E_{fe}, are unknown a priori. To determine E_{fe}, we calculate the total energy E_S of a sample consisting of the two slabs for each material with the ends fixed and with an interface separation sufficient to ensure that the two sides of the interface do not interact and obtain

$$E_{fe} = E_S - E^{Al}_B - E^{Si}_B - A\gamma \tag{3.2}$$

The energy per unit projected area of the fractured surface configuration can then be calculated as

$$E_F = (E_T - E^{Al}_B - E^{Si}_B - E^{fe})/A \tag{3.3}$$

For fracture propagation, we are also interested in the energy of the as-created interfaces. The initial interface simulation cells have a small amount of strain energy present from holding the ends fixed during relaxation. If the annealed interfaces are used without changing the boundary conditions this extra strain energy would be erroneously associated with the interface. To eliminate this strain energy, the originally-fixed ends are relaxed while holding their y-z positions fixed. Such a structure now consists of three energy components: E_B, the new relaxed end energy E_{fe}, and the interface energy E_I. The interface energy per unit area is then

$$E_I = (E_T - E_B - E^{fe})/A \tag{3.4}$$

With the above surface energies properly calculated, the work of fracture for the actual separated interfaces, W_S , is given by

$$W_S = E_F - E_I \tag{3.5}$$

while the Griffith work of fracture, W_G, associated with perfect cleavage fracture of the as-fabricated interface is given by

$$W_G = \gamma - E_I \tag{3.6}$$

We can thus define a toughness enhancement factor as

$$T = W_S/W_G \tag{3.7}$$

The various energies associated with all the interfaces are shown in Table 3.2. The values of W_G vary by as much as a factor of 2 between the interfaces but in general are small. The actual fractured surface energies E_F can equal γ, but are usually higher

due to roughness and/or deformation. Fracture surfaces that show little roughness and almost no residual adhesion of Al on Si (B, D, F) have fracture surface energies nearly identical to the clean surface energy, $W_S \sim W_G$, and thus $T \sim 1$, and are characterized as brittle. The fractured surfaces that are more irregular with considerable Al adhesion on the Si (A, C, E, G, H, I) have higher E_F values relative to the γ values, and thus $T > 1$, and are characterized as ductile. These ductile interfaces are broken up into two types of failure: those that fail after dislocation emission during failure (A and C) and those that do not emit dislocations from the interface(E, G, H, I). The toughest interfaces, with $T \sim 2.0 - 2.2$, emit dislocations from the interface into the Al slab, which permit energy to be absorbed by the bulk of the material and away from the high local stresses at the interface. The extra energy resulting from the dislocations is a component of energy that is not directly related to the structure of the surface. The remaining ductile interfaces show lower toughness of $T \sim 1.4-1.7$ that are caused by the roughness of the Al surface and the fraction of the Al surface with a local (111) orientation. As mentioned before, much of the fractured Al fails along the (111) planes that results in surface energies reflecting the lower energy of this close packed orientation. Al (111) has a surface energy of 0.0366 eV/$\mathring{A}^2$ versus energies of 0.0492 eV/$\mathring{A}^2$ and 0.0526 eV/$\mathring{A}^2$ for Al (100) and Al (110). An interface can fail with only moderate toughness enhancement over the brittle value by creating a rough interface consisting of Al (111) planes. The differences between G and I are good examples of the role the Al (111) surface has in determining toughness: G has a smoother fracture surface but contains significant Al (110) structure, while I has significant roughness but much of the failed Al surface area is locally (111) causing a lower final fracture energy. It is also interesting to note which Al interfaces lead to particular types of failures. The most brittle interfaces are created using Al (111)

Table 3.2: Interface and fracture energies for various Al/Si interfaces.

Label	Al Surface	Si Surface	E_I (eV/Å^2)	γ (eV/Å^2)	E_F (eV/Å^2)	W_G (eV/Å^2)	W_D (eV/Å^2)	T
A	100	100	0.113	0.163	0.224	0.050	0.108	2.2
B	111	111	0.098	0.141	0.140	0.042	0.041	1.0
C	100	111	0.113	0.153	0.193	0.040	0.079	2.0
D	111	100	0.112	0.151	0.158	0.039	0.046	1.2
E	110	100	0.115	0.167	0.195	0.052	0.078	1.5
F	111	112	0.103	0.136	0.147	0.033	0.043	1.3
G	113	335	0.121	0.147	0.165	0.025	0.044	1.7
H	221	113	0.117	0.148	0.167	0.031	0.049	1.6
I	110	331	0.087	0.152	0.179	0.065	0.092	1.4

surfaces. The Al (111) has a tendency to keep its initial structure when failing independent of the Si structure. The toughest interfaces come from those constructed with Al (100) surfaces. The Al (100) interface is the structure that is most likely to emit dislocations because of the near 45 degree orientation of the Al (111) slip planes allowing lower tensile stresses needed to approach the necessary shear stresses required for slip. Correlating the two sets of results on strength and fracture energy, the two properties are dominated by two main factors: the Si surface structure and the orientation of Al (111) planes. The strongest interfaces are those that have a high Si surface density with uniformly distributed dangling bonds normal to the surface. The toughness of the interfaces is dominated by the orientation of Al (111) planes relative to the direction of the applied load. The orientations of both Al and Si can be used together to create interfaces that are strong and tough, as shown for interface A which has the tough Al surface and the strong Si surface. Most poorly-matched interfaces incorporate the worst combination of rotated Al (111) planes and rough Si surface, leading to interfaces with relatively low strengths and toughnesses. While

these toughnesses and strengths are relatively low compared to more-perfect interfaces, the strengths are still high compared to those of bulk materials. Based on our results, Al-Si composites are not expected to show low-strain crack nucleation at the Al-Si interfaces nor easy propagation once cracks are nucleated; both aspects are encouraging for the performance and functionality of Al-Si.

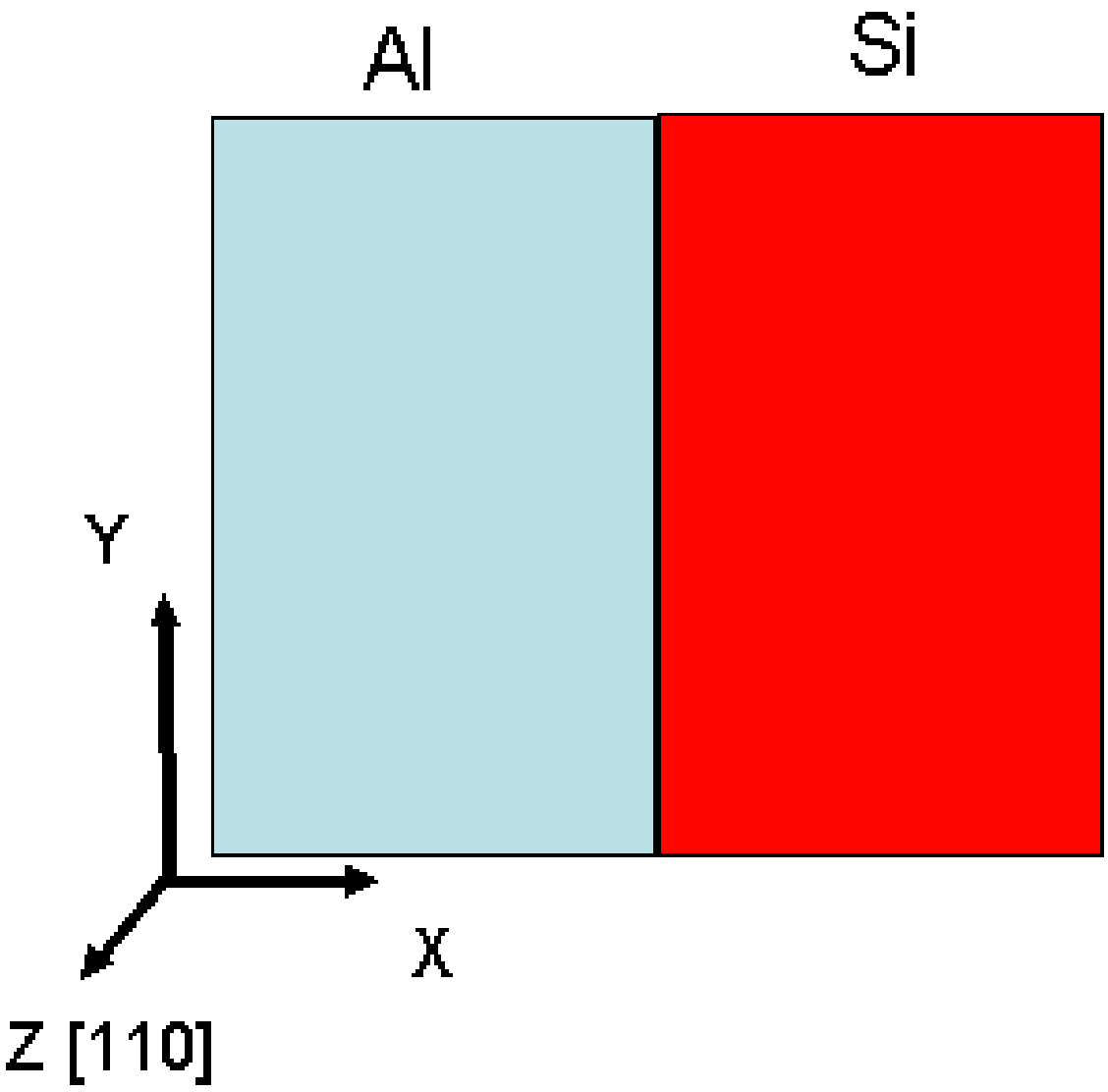

Figure 3.1: Schematic of the bimaterial interface test geometry.

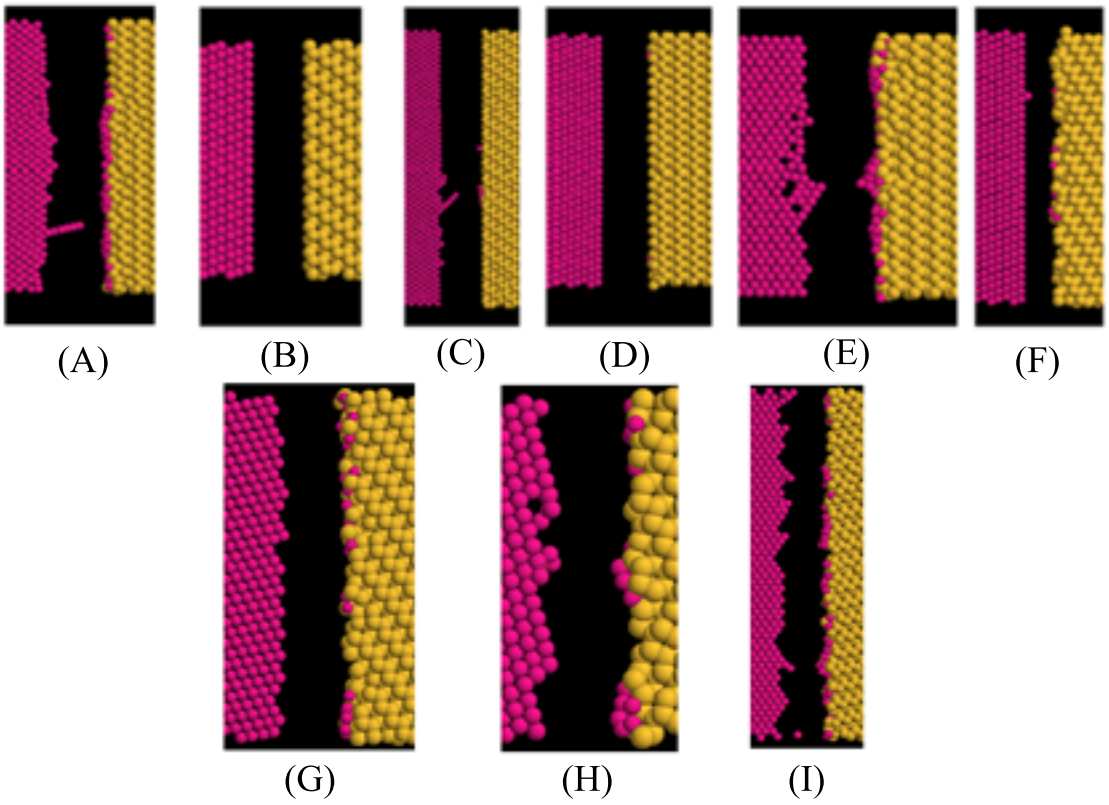

Figure 3.2: Fracture morphologies for various Al/Si interface failures A-I(see Table 3.3).

Chapter 4

Al/Si composites: MD Study

4.1 Al-Si Nanocomposite Structures

With a detailed study of the deformation, strength, and fracture energy of a set of Al-Si interfaces having various orientations completed the topic of Al-Si nanocomposites can now be investigated. Since highly mismatched Al/Si interfaces show good tensile strength and significantly enhanced fracture energy relative to structurally-well-matched interfaces, it is possible that nanocomposites can have good strength and toughness. The study here examines several aspects of Al-Si nanocomposites including elastic response, plastic deformation mechanisms and failure processes as well as making comparisons to Al polycrystals. The elastic responses of the nanocomposites are shown to depend on several factors including amount of Si content as well as the orientation of the highly anisotropic Si particles. MD results also indicate that the mechanisms of nanocomposite deformation are quite different from the Al polycrystal, with dislocation activity suppressed but Al-Si interface deformation enhanced. These competing effects lead to macroscopic behavior similar to Al polycrystals in low-Si-content nanocomposites but to higher yield stresses in higher-Si-content nanocrystals. With increased deformation at the interfaces it is not surprising that

the dominate failure mechanism is at the interfaces. The normal loads at which the composites fail are found to be lower than loads for the bicrystal due to composite stress concentrators. A self consistent Eshelby analysis, Eshelby (1957) predicts the stress concentration and in combination with known interface failure stresses is used to determine remote loadings that result in composite failure.

The polycrystal nanocomposite geometry studied here contains eight columnar hexagonal grains having diameters of 5 nm. All grains have a common crystal orientation parallel to the columnar z-axis. A z-thickness of 1.145nm accommodates the periodic mismatch (less than 0.5%) between the Al and the Si such that the composite consists of eight atomic layers in the Al grains and six atomic layers in the Si grains in the thickness direction. A schematic of the polycrystal structure is shown in Figure 4.1. The in-plane (x-y) crystallite orientation of each grain is randomly chosen, leading to a range of grain boundaries angles and a range of resolved shear stresses acting on the primary slip systems. Nanocomposite samples are created by assigning an Al or Si identity to each grain and growing the appropriate crystal structure from the center of the grain following the assigned cell orientation until the crystal reaches the grain boundary. The as-constructed system size is 25.6nm x 14.78nm x 1.145nm and contains approximately 25,000 atoms.

The use of columnar grain structures is well-established in the literature (Yamakov *et al.* (2001, 2002, 2003)) as a means of studying deformation mechanisms and trends in nanomaterial behavior in a computationally-efficient manner. Nonetheless, some remarks are warranted. Selection of the (110) grain texture yields four available (111) slip planes in every fcc grain of the system, which is sufficient for general plastic deformation in 2d. Thus, deformation via both dislocation plasticity and grain-boundary sliding is possible in these materials. The small sample thickness limits the deformation to nearly 2d plane strain conditions, so that the occurrence of cross-slip,

grain rotation, dislocation junction formation, and/or dislocation multiplication is reduced relative to a 3d grain structure. The thickness is large enough, however, that the activation energy for dislocation nucleation at finite temperature is relatively close to the correct value Zhu and Yip (2004); plasticity is thus not artificially enhanced by low nucleation barriers as would be the case for much smaller thicknesses. Since experimental microstructures in Al-Si tend toward columnar structures, the overall geometry used here has some similarities to materials that have been fabricated.

We have examined 10 nanograin polycrystals with 3 different Si concentrations. To focus on the effect of the Si additions, two sets of nanocomposite structures consist of crystal orientations that are held fixed, with Si grains simply replacing identically-oriented Al grains. Each set thus consists of (i) an all-Al polycrystal containing 8 Al grains (8Al), (ii) a nanocomposite containing 7 Al grains and 1 Si particle (7Al-1Si) substituted at the location of grain 1 with the same orientation as the replaced Al particle, and (iii) a nanocomposite containing 6 Al grains with 2 Si particles (6Al-2Si), with one Si particle at grain 1 and one Si particle at grain 8. Set 1 was generated with random orientations while Set 2 was constructed with all grain boundary mismatch angles larger than 22.5. To augment this set of simulations, we have generated 4 nanocomposites, denoted Random 1-4, with random grain orientations that are completely different than the two sets above. Materials Random 1 and 2 contain 1 Si particle and Random 3 and 4 contain 2 Si particles. Random 3 has two Si particles separated in the same location as the configurations in Set 1 and 2, while Random 4 has the Si particles adjacent to one another at grains 6 and 1.

After creating each nanocomposite material, the system is annealed for 20 ps at 300 K, using NPT dynamics and full periodic boundary conditions, to relax the as-built interface structures and to reach local equilibrium for the entire specimen. The tensile loading is then applied in increments of 1% strain in the x-direction, followed by

relaxation at 300 K for 20 ps while holding the cell length along x fixed with all other lengths free to relax. Due to the constraints on the system during annealing, small amounts of compressive residual stress are present at the starting state deemed to be zero deformation. The computed stress-strain curves, with strain measured from the zero deformation state, are thus corrected by substracting the residual strain (shifting the as-computed stress-strain curves to negative strains) so that the state of zero global stress coincides with a state of zero strain in all nanocomposites. Stresses in the system are measured using the Virial expression, from Chap. 2, to compute the product of the atomic stress and atomic volume (McLellan (1974)), and the result is divided by the undeformed perfect crystal volume per atom. The global applied stress is computed by summing the Virial contributions from all of the atoms and dividing the result by the entire cell volume.

4.2 Composite Elastic Response

Ten different polycrystals were created and strained to failure. The tensile stress-strain curves for nanocomposite Set 1 are shown in Figure 4.2a and those for Set 2 are shown in Figure 4.2b. The stress-strain curves for all four 7Al-1Si nanocomposites and all four 6Al-2Si nanocomposites are shown in Figures 4.3a,b, respectively. The initial response of all materials is nearly linear up to at least $\sim 2\%$ strain. We compute an effective tensile elastic modulus by fitting a linear line through the data up to 2% strain for each composite; the resulting values are shown in Table 4.1.

Considering the average over all specimens of the same Si content, there is a 4% increase with 1 Si and an 11% increase with 2 Si. As a check of these values a self-consistent Eshelby analysis for cylindrical, elastically-isotropic Si particles with E=165 GPa embedded in a homogeneous elastically-isotropic Al matrix with $E =$ 68 GPa is used to predict these increases. For a generic anisotropic material the

Table 4.1: Effective tensile elastic moduli for Al-Si nanocomposites, in GPa.

	8Al	7Al-Si	6Al-2Si
Set 1	67.7	70.9	91.6
Set 2	65.5	69.1	73.9
Random 1	—	66.3	—
Random 2	—	70.9	—
Random 3	—	—	65.5
Random 4	—	—	64.9

composite stiffness is determined using:

$$\bar{\mathbf{C}} = \mathbf{C}_m(\mathbf{I} + v_f\mathbf{G})^{-1} \tag{4.1}$$

where $\bar{\mathbf{C}}$ is the composite stiffness matrix, v_f is the volume fraction of Si, and $\mathbf{G}$ is defined as:

$$\mathbf{G} = \left[(\mathbf{C}_m - \mathbf{C}_p)(\mathbf{S} - v_f(\mathbf{S} - \mathbf{I}_d)) - \mathbf{C}_m\right]^{-1}\left[\mathbf{C}_p - \mathbf{C}_m\right] \tag{4.2}$$

Where $\mathbf{C}_m$ and $\mathbf{C}_p$ are the stiffness matrices for the Al matrix and Si particle respectively. $\mathbf{S}$ is the Eshelby tensor which contains components of elastic coefficients and ultimately relates the constrained and stress free strains in the analysis. This simple analysis results in a composite stiffness matrix and the directional Young's modulus is determined by calculating the compliance matrix from $\bar{\mathbf{C}}$ (Eshelby (1957); Lee and Paul (2005)). The Eshelby analysis predicts increases of $\sim 11\%$ and $\sim 24\%$ for the 7Al-1Si and 6Al-2Si composites, respectively . Thus, the computed elastic stiffening upon introduction of relatively stiff Si particles is roughly consistent with, but somewhat lower than, analytic estimates. The lower values may be due to the additional compliance from the highly-mismatched Al-Si interfaces in a small-grain material; grain boundary compliance in single-phase materials reduces overall stiffness in the 5 nm grain size range (Latapie and Farkas (2003)) so a similar grain-size-dependent

effect should exist in nanocomposites.

Although within one set of identical orientations the effective modulus increases steadily but modestly with Si content, the modulus data for the composite systems shows considerable scatter. This can be partially attributed to the differing particular orientations of the Si particles. Al is relatively isotropic (modulus vs orientation ranging from 63-73 GPa) and so Al textures will not significantly influence the stiffness, consistent with our data for the two 8Al materials. In contrast, the modulus of a Si crystal with a (110) out-of-plane orientation varies from 182 GPa for loading along $(1\bar{1}1)$ to 130 GPa for loading along (001). For the 6Al-2Si material of Set 1, the Si particles have effective moduli of 180 GPa and 181 GPa, while for the 6Al-2Si material of Set 2, the Si particle effective moduli are 181 GPa and 150 GPa; this is roughly consistent with the observation that 6Al-2Si in Set 1 has a higher effective composite modulus than that in Set 1. These large fluctuations of effective modulus appearing in nanocomposites consisting of only a few grains should disappear in systems with more grains. The 7Al-1Si composites show a smaller dependence on the Si orientation, due to the dominant isotropic behavior of Al and the role of Al/Si interfaces.

4.3 Plastic Deformation Mechanisms

The onset of non-linearity in the stress-strain curves in Figures 4.2 and 4.3 correlates well with the generation of dislocations or grain boundary motion; therefore we define the yield stress by these two indications. The inclusion of Si increases the material yield stress. The 8Al polycrystals yield at $\sim$ 1.5 GPa, the 7Al-1Si nanocomposites yield at $\sim 1.5 - 2.5$ GPa, and the 6Al-2Si nanocomposites yield at $\sim 2.5 - 3.0$ GPa. Beyond the onset of non-linearity around 2-3% strain and up to

significant plasticity levels ($\sim 4.5\%$) the stress-strain responses of the 8Al and 7Al-1Si nanocomposites with the same orientations are quite similar. However, the actual deformation mechanisms are quite different. Figures 4.4a,b,c show the contours of effective strain E_e(See Chap. 2) for nanocomposite Set 1 at $\sim 4.6\%$ applied strain. The 8Al nanocrystal shows several dislocations emitting from the grain boundaries and distributed grain boundary sliding/shearing, similar to behavior found by Farkas *et al.* (2002) for (110) columnar Ni at a similar grain size. In contrast, the 7Al-1Si and 6Al-2Si nanocomposites with the exact same grain orientations show essentially no dislocations in the Al grains and only a small amount of sliding/shearing along the Al-Al grain boundaries. Rather, most of the deformation in the nanocomposites is due to sliding/shearing along the Al/Si interfaces. The 6Al-2Si nanocomposites show even less activity within the Al and more distributed deformation among the more-prevalent Al/Si interfaces as compared to the 7Al-1Si materials. The reduction of dislocation activity at essentially the same strain level accounts for the higher yield stresses exhibited for the higher-Si-content composites. Figures 4.5a,b,c show the contours of effective strain E_e for nanocomposite Set 2 at $\sim 3.7\%$ applied strain, $\sim 1\%$ lower than that in Set 1, Figure 4.4. Set 2 thus shows much less dislocation activity that is similar among the samples. But, the general observation that the 8Al polycrystal has more deformation along the Al/Al grain boundaries while the 7Al-1Si and the 6Al-2Si nanocomposites show deformation primarily along the Al/Si interfaces is the same as found for Set 1. Similar to Set 1, the introduction of a second Si particle causes the deformation to be spread more evenly across the Al/Si interfaces. The remaining nanocomposite simulations with other random grain orientations show similar trends.

The inclusion of Si particles thus reduces the generation of dislocations in Al

grains, which leads to higher yield stresses exhibited for the higher Si content composites. The inclusion of Si particles also reduces the relative motion of the Al grains by decreasing both sliding/shearing along the grain boundaries and dislocation from the boundaries, but this is largely compensated by severe deformation at the Al/Si interface. Since both dislocation and grain boundary mechanisms are suppressed, which are the types of deformation mechanisms suggested to replace one another as grain size decreases, this phenomenon may be independent of grain size. The change in deformation mechanism upon introduction of Si particles and the accompanying increase in yield stress thus imply the potential for enhanced hardness in Al-Si nanocomposites. We discuss this conclusion vis a vis recent experiments later.

4.4 Nanocomposite Failure Processes

Upon attaining $\sim 5\%$ strain, all the materials studied here begin to show significant dislocation activity and increased Al/Al grain boundary sliding, suggesting that the Si particles can no longer inhibit these deformation mechanisms at high stresses. At strains of $\sim 5.5\%$, all the materials are on the verge of failure or localization, as indicated by a decreasing stress with increasing applied strain (Figures 4.2 and 4.3). Interestingly, the material failure strength, defined as the maximum stress, is nearly the same for all systems so that the Si additions provide little or no additional strength in tensile simulations. Nonetheless, the mechanisms of failure in the 8Al and in the Al-Si nanocomposites are completely different. Briefly summarizing the results shown below, the two 8Al nanocrystals show similar void generation at triple junctions or grain boundaries accompanied by localized shearing, followed in one case by propagation of a transgranular crack and in the other case by linkage of voids along the grain boundaries, leading to failure. In contrast, the Al-Si nanocomposites all show increasing localized deformation at the Al-Si interfaces, leading to void

generation and ultimate debonding at one of those interfaces.

The failure strength of the Al polycrystals reaches values of $\sim$ 3 GPa. Figure 4.6 shows the distribution of tensile stress σ_{xx} and the atomic structure before and after fracture, along with the effective strain mapping after fracture in the two Al polycrystals. The areas of alternating high and low stress along the grain boundaries represent the grain boundary mismatch; the more important stress contours are those extending over many atoms and representing stress in response to the applied loading. The two 8Al materials show different failure modes. The 8Al in Set 1, which contains predominantly low angle boundaries, first exhibits grain coalescence and annihilation of some triple junctions as seen in simulations of nanocrystalline Pd, (Haslam *et al.* (2001)) and, Ag-Ni (Qi and Cheng (2004)), followed by formation of a brittle crack initiating at a stress concentration (circle in Figure 4.6a1) near the annihilated triple junction and propagating in a grain having planes aligned perpendicular to the loading axis. The 8Al in Set 2, which has all high angle grain boundaries, fails by the coalescence of grain boundary voids into a crack, similar to MD simulations of nanocrystalline Ni Farkas and Curtin (2005). Near both cracks, a localized shear-band-like deformation appears with the crack growth, as shown in both Figure 4.6a3 and 4.6b3.

In the Al-Si nanocomposites, failure is dominated by local orientations and stress concentrators at particular Al/Si interfaces that lead to void generation and failure. Failure is thus similar to that seen for Al/Si bimaterials discussed in Chap. 3 and differs from the crack growth accompanied by shear bands found in the Al polycrystals. Figures 4.7a-d show the tensile stress distribution for the four different 7Al-1Si materials just before or at failure, $\sim$ 5.5% strain. In contrast to the uniform distribution of stresses near the grain boundaries in the Al polycrystals (Figures 4.5,4.6), the stresses for the composite are concentrated within the Si particle, leading to higher stresses at

the Al/Si interfaces. Failure occurs by void formation at a particular interface in each material. Figures 4.8a-d show the interface damage in the 7Al-1Si nanocomposites at a deformation of $\sim 7.5\%$ strain, using the effective strain mapping to clearly show the damage. The various samples are at different stress levels, and conveniently show the progression of damage. Figure 4.8b, at the highest stress of 2.8 GPa, shows the early stage where several voids have formed at Al/Si interfaces. Figures 4.8a,c, at a lower stress of 2.5 GPa, both show one major crack formed along one Al/Si interface after void coalescence. Figure 4.8d, at the lowest stress of 1.3 GPa, shows total separation of two Al/Si interfaces. In contrast to the 8Al case, there is no localized shear band accompanying the crack growth. Instead, the crack grows only by void coalescence at the Al/Si interface.

To assess the nanocomposite failure more quantitatively, we have analyzed the tensile stress normal to each failing Al/Si interface by transforming the stress tensor for each 7Al-1Si composite into the appropriate orientation. Figures 4.9a-d show the tensile component of the rotated stress tensor that is normal to the failing interface, with the star indicating the failing interface. The stresses acting normal to the interfaces that first exhibit voids are $\sim 4-5$ GPa, which are $\sim 1-2$ GPa higher than the remote loading. This stress concentration is attributed predominantly to the stress concentration caused by the elastic mismatch between the stiff particle and the softer matrix. The Eshelby analysis is also used to predict the stress concentration at the interface. The concentration is determined from:

$$\begin{aligned}\sigma_{ij} =&(1+\beta B)\sigma^A_{ij} - B(\sigma^A_{ik}n_k n_l + \sigma^A_{lk}n_k n_i) + \frac{B}{1-\nu}\sigma^A_{jk}n_j n_k n_i n_l \\ &+ \frac{1-2\nu}{3(1-\nu)}B\sigma^A_{jk}n_j n_k \delta il - \frac{1-2\nu}{3(1-\nu)}A\sigma^A(n_i n_l - \frac{1}{3}\delta_{il}\end{aligned} \tag{4.3}$$

where σ_{ij}^{A} is the remote load, n_i is the interface normal at the point of stress concentration and ν is Poisson's ratio for the matrix. A and B are defined as:

$$A = \frac{\kappa_p - \kappa_m}{(\kappa_m - \kappa_p)\alpha - \kappa m} \tag{4.4}$$

and

$$B = \frac{\mu_p - \mu_m}{(\mu_m - \mu_p)\beta - \mu_m} \tag{4.5}$$

where κ_m, μ_m and κ_p, μ_p are the bulk and shear moduli for the matrix and particle respectively and α and β are:

$$\alpha = \frac{1}{3}\frac{1+\nu}{1-\nu}, \beta = \frac{2}{15}\frac{4-5\nu}{1-\nu} \tag{4.6}$$

The analysis predicts that the elastic mismatch generates a stress concentration of ~ 1.5. At the average maximum remote load of 2.8 GPa, the local interface tensile stress is thus predicted to be 4.3 GPa, consistent with the observed magnitudes of the local stresses shown in Figure 9. Differences in geometry, the effects of triple points Tvergaard and Hutchinson (1988); Picu and Gupta (1996), and interfacial compliance (Gao (1995)) can modify this result, but the simple analysis rationalizes the observed stress concentrations.

Proceeding further, the interfaces that fail for three of the 7Al-1Si nanocomposites are Al(110)/Si(331) , Al(113)/Si(335) , and Al(221)/Si(113), which were previously examined in the bimaterial simulations (Table 3.1). The strengths of these interfaces are $\sim 4-5$ GPa, i.e. in the same range as the local stresses acting on these boundaries at the point of failure (see Figure 4.9. The nanocomposite interfaces also fail similarly to the bimaterial samples, with voids nucleating at the interface, leading to debonding with some Al remnants adhering to the Si grains after the crack has opened. Therefore, these lower-strength, but well-formed and annealed Al/Si interfaces control the

onset of failure in the Al-Si nanocomposites.

For the 6Al-2Si nanocomposites, the failure modes and strengths are very similar to those of the 7Al-1Si composites. The stresses within Si particles are larger and distributed more evenly relative to the 7Al-1Si, but the normal interface stresses are comparable. Failure is initiated at one of the boundaries in the form of voids. The nanocomposite with two adjacent Si particles is similar to the nanocomposite with two separated particles. There is thus little effect of Si content on the mechanism or strength of the nanocomposite over the range of Si content studied here.

4.5 Experimental Comparison

As noted early, there are new experimental results available for the hardness and modulus of thin-film Al-Si nanocomposites fabricated by co-deposition via sputtering (Olk and Haddad (2006); Olk *et al.* (2006)). These films consisted of 5-15nm Al crystallites embedded in an amorphous Si (aSi) matrix with Si content from 17 to 65 at% and $\sim$ 10% Oxygen content, believed to exist as amorphous SiO2. These materials differ from those studied here in numerous ways: (i) our microstructure is the inverse of the experimental one, (ii) we use crystalline Si (cSi), (iii) our Si contents are 10 at% (7Al-1Si) and 19.6 at% (6Al-2Si), (iv) our Al grain size is at the low end of the experimental range, (v) our materials contain no oxide phases. Thus, only rough comparisons can be made and we restrict our discussion to the low-Si content materials.

The measured elastic modulus of 55-100 GPa is in the range of our predicted values. Overall, there is no clear trend of increasing modulus with increasing Si content in the experimental data, which could be due to porosity, low modulus of amorphous Si Tan *et al.* (1972) and/or oxide phases , or significant surface roughness. Of more interest is the flow behavior. Materials with $\sim$ 20 at% Si show a hardness of

$H \sim 3$ GPa, suggesting a yield stress of $H/3 \sim 1$ GPa as compared to our simulated yield stresses of $\sim 2.5 - 3.0$ GPa. The measured hardness values also increase with increasing Si content, qualitatively consistent with the simulations although over a different range of Si content.

In general, the simulation yield strengths are higher than the experimental values; this is consistent with most studies of nanocrystalline materials and can be attributed to several factors. The simulated materials have defect-free grains so that deformation mechanisms are limited to the grain boundaries whereas the experimental materials likely have defects in the grains that can contribute to early plastic deformation and lower yield stresses. The other defects, such as porosity and oxide phase in the experimental materials may contribute other effects. There are other trends and features in the experimental data with regard to, for example, Al crystallite size, that are beyond the scope of our considerations here. However, using the present results as a baseline, we are now developing simulation microstructures to investigate the role of grain size and other microstructures for Al-Si nanocomposites.

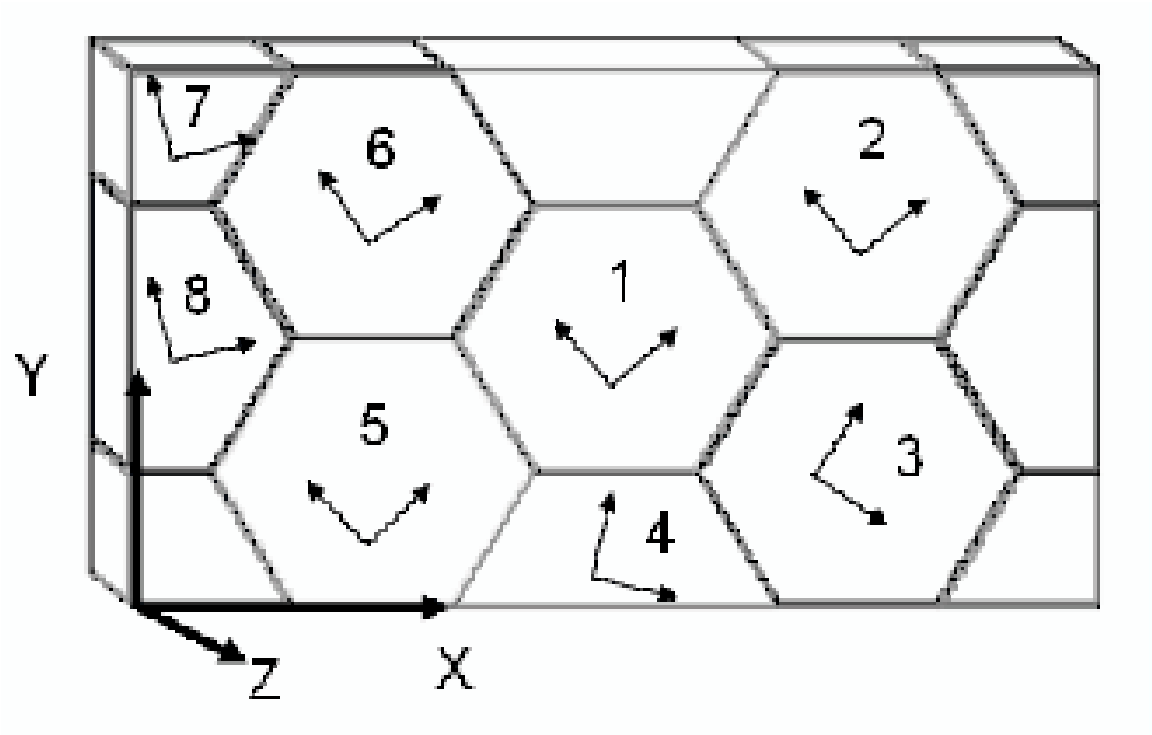

Figure 4.1: Schematic of periodic cell construction for the Al/Si nanocomposites.

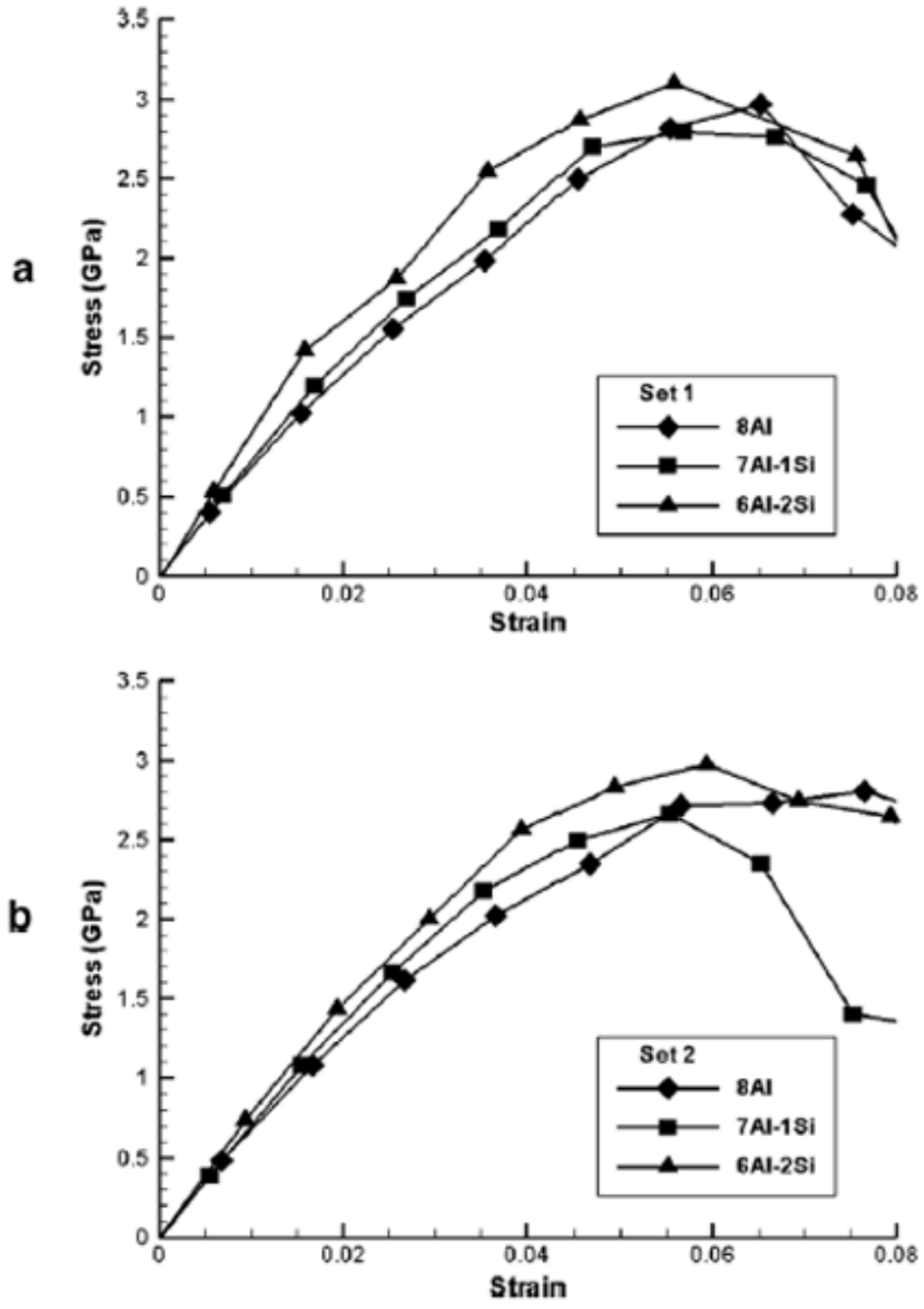

Figure 4.2: Stress-strain curves for Al-Si nanocomposites: a) Set 1 ; b) Set 2.

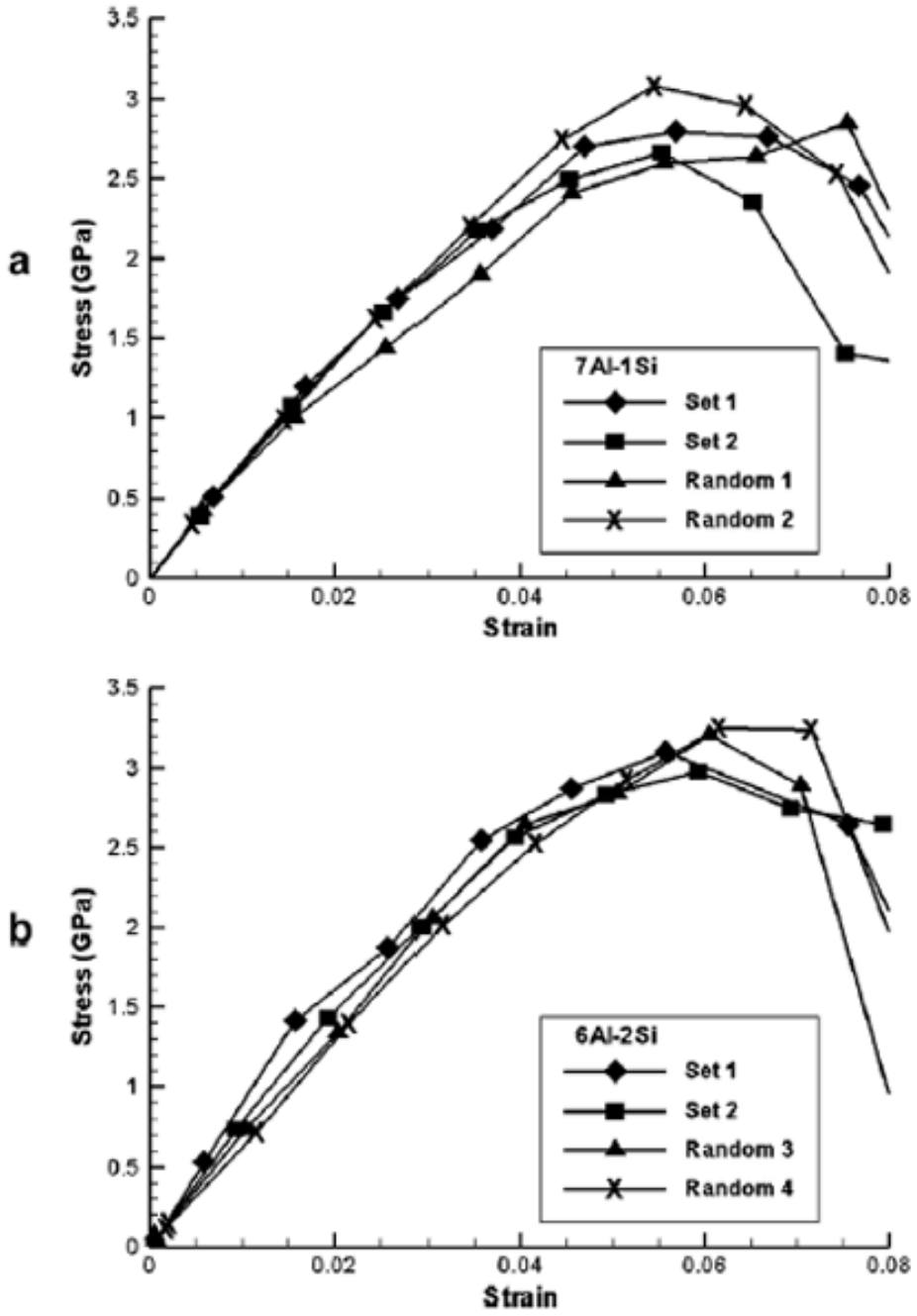

Figure 4.3: Stress-strain curves for Al-Si nanocomposites: a) 7Al-1Si samples ; b) 6Al-2Si samples.

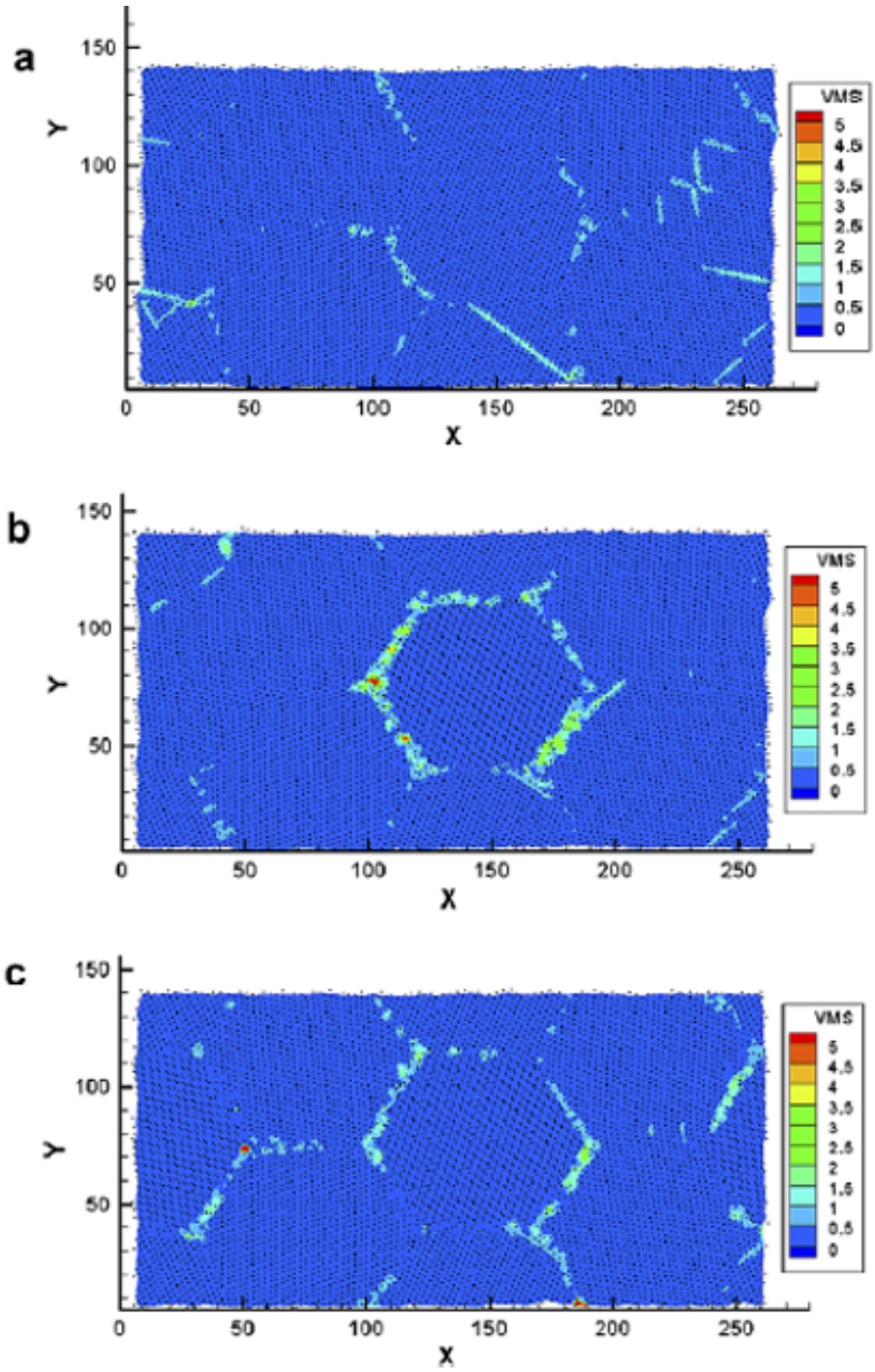

Figure 4.4: Effective strain mappings in Set 1 nanocomposites at $\sim$ 4.6% strain: a) 8Al, 4.5% strain; b) 7Al-1Si, 4.7% strain c) 6Al-2Si, 4.6% strain.

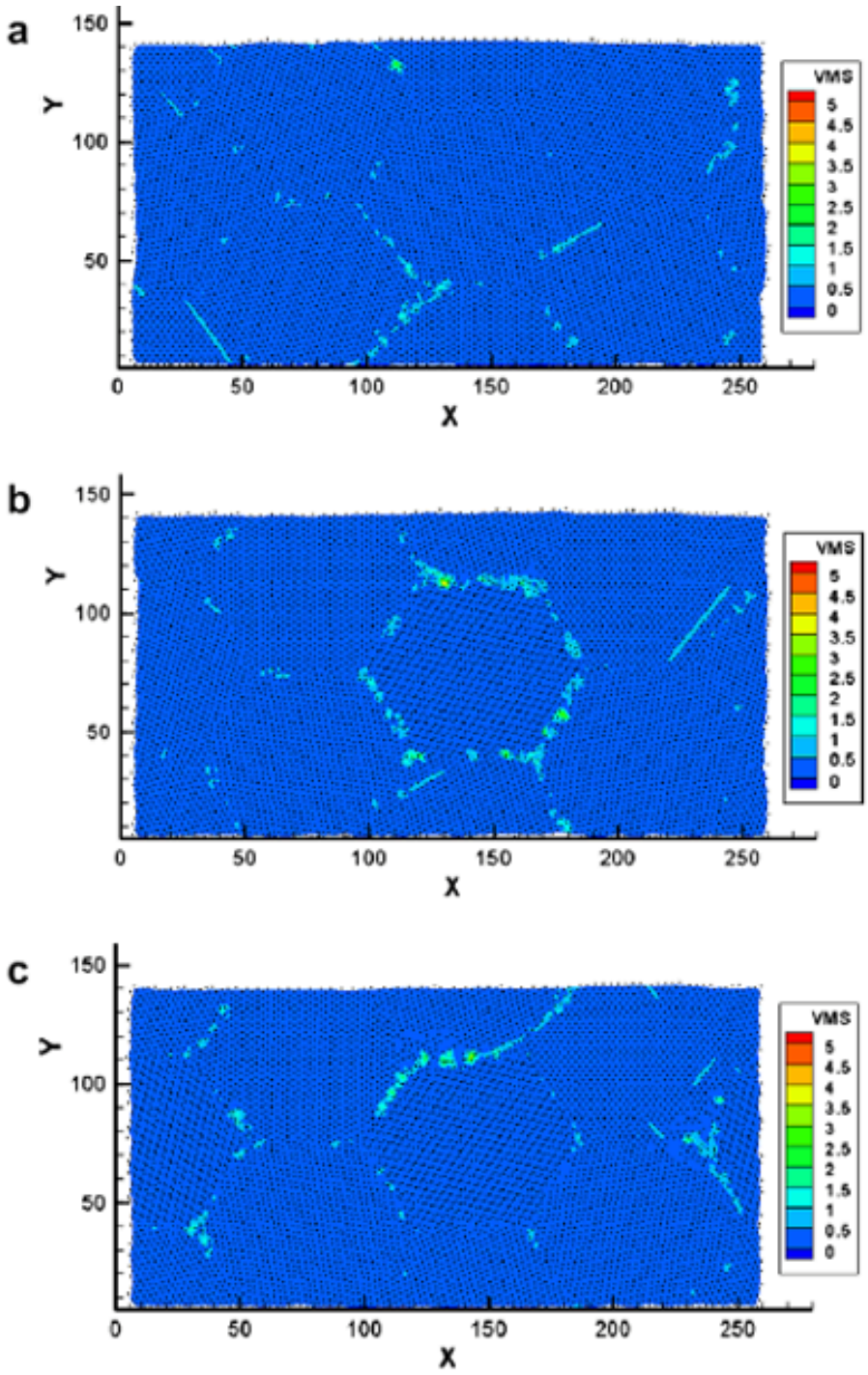

Figure 4.5: Effective strain mappings in Set 2 nanocomposites at $\sim$ 3.7% strain: a) 8Al, 3.7% strain; b) 7Al-1Si, 3.5% strain c) 6Al-2Si, 3.9% strain.

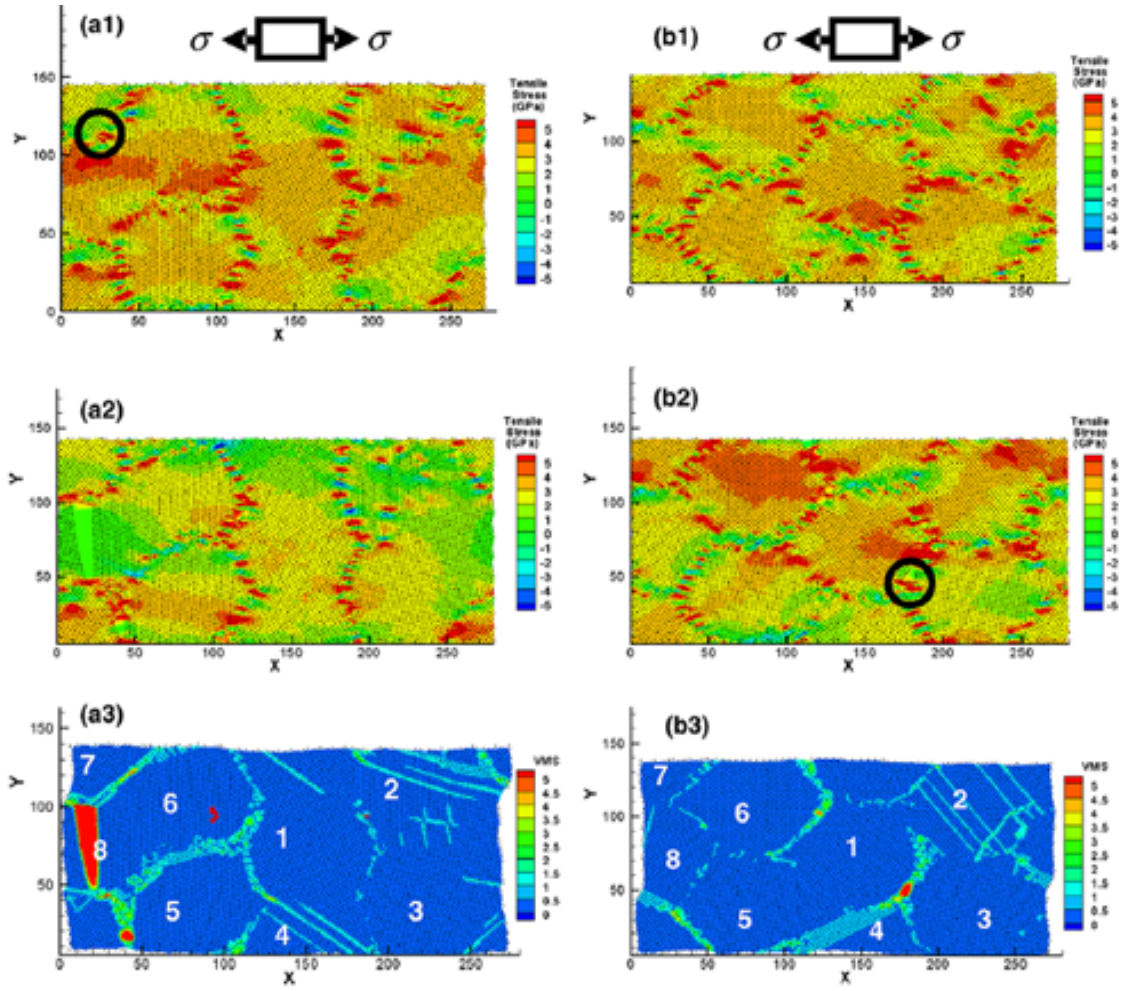

Figure 4.6: Tensile stress σ_{xx} and effective strain mapping distribution in 3 Al nanocrystal materials: a1) Set 1 at, 5.5%; a2) and a3) Set 1 at 8.5%; b1) Set 2 at, 5.7% b2) and b3) Set 2 at 8.7%.

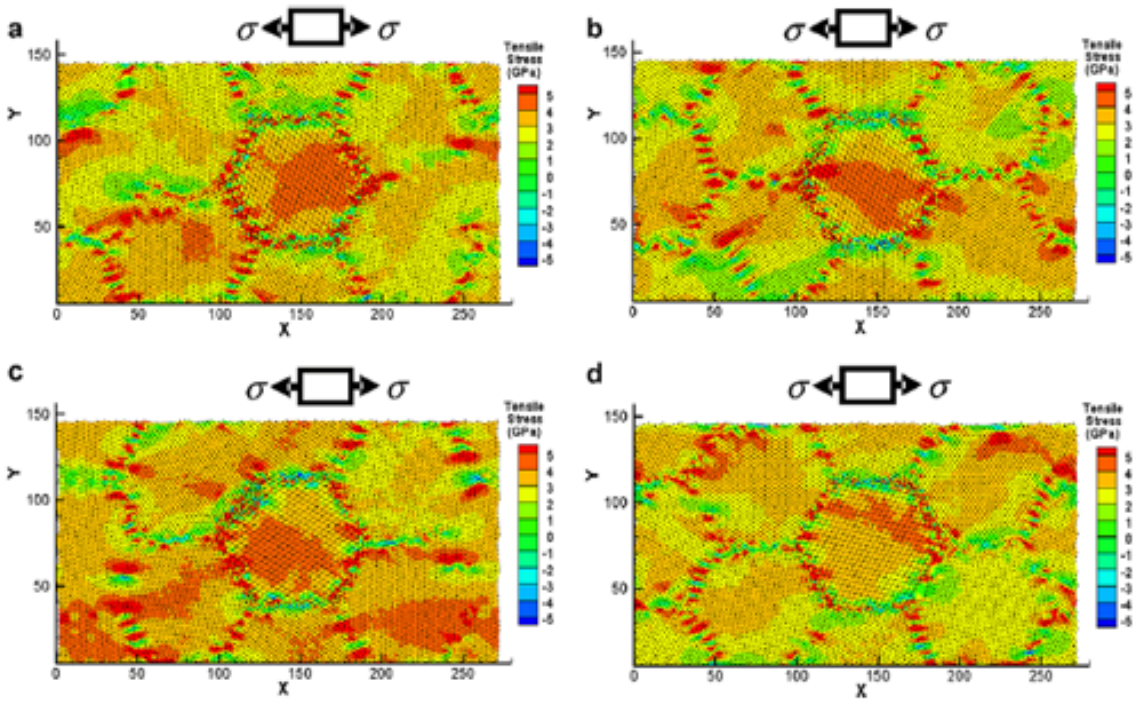

Figure 4.7: Tensile stress σ_{xx} distribution for the four different 7Al-1Si nanocomposites around 5.5% strain: a) Set 1 at 5.7%; b) Random 1 at 5.6%; c) Random 2 at 5.5%; d) Set 2 at 5.5%.

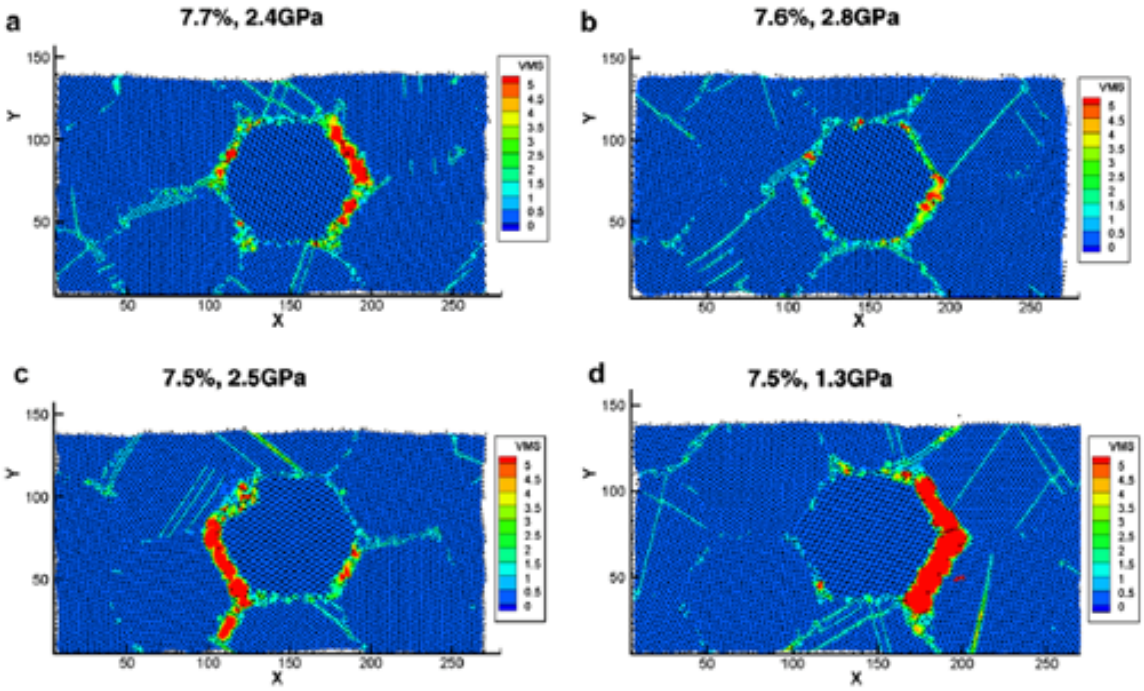

Figure 4.8: Effective strain mappings for 7Al-1Si nanocomposites with significant failure: a) Set 1; b) Random 1; c) Random 2; d) Set 2.

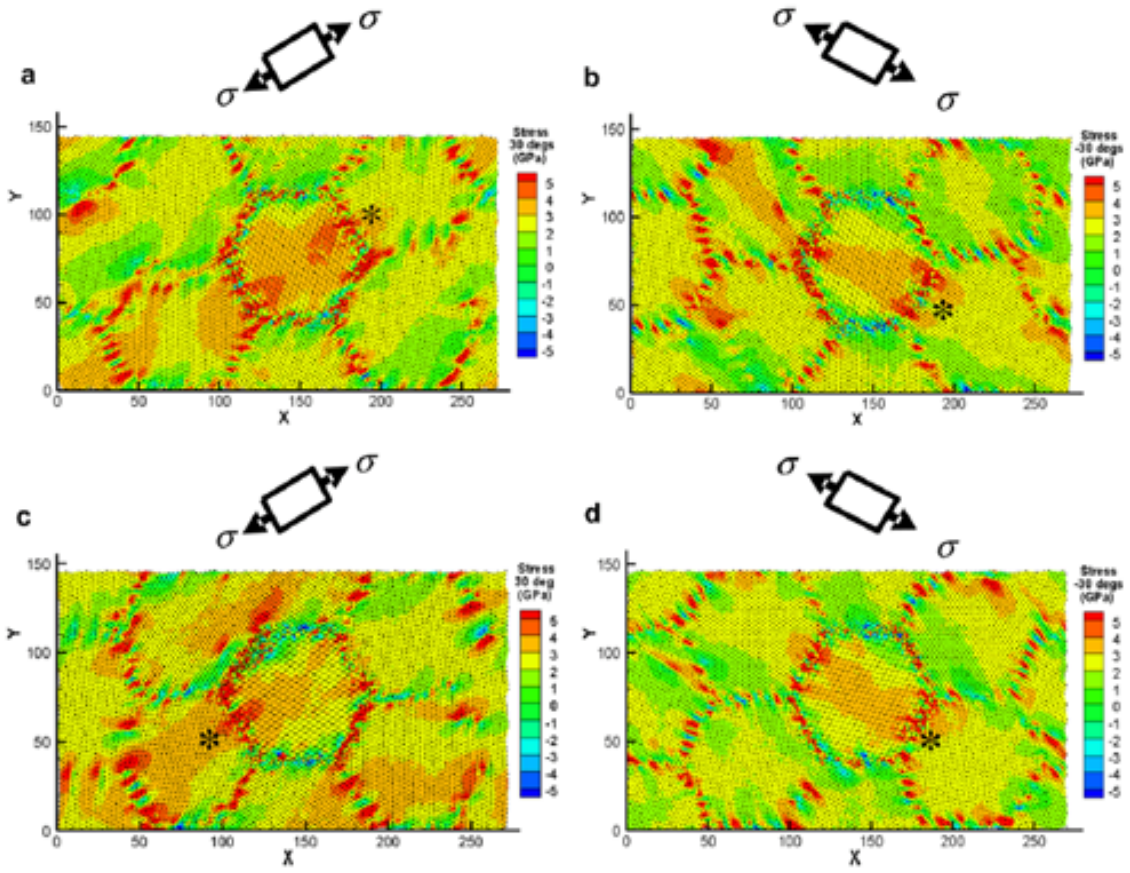

Figure 4.9: Tensile stress distribution along rotated axis shown, corresponding to the normal stress across the failing interface, in a) 5.7% strain of Set 1, b) 5.6% strain of Random 1, c) 5.5% strain of Random 2 and d) 5.5% of Set1.

Chapter 5

Molecular Dynamic Results of Single Asperity Indentation

To study the plastic response of nanorough surfaces, the compression of extremely well-characterized nanoscale asperities in the form of Au pyramids, similar to those of the Wang experiments, are studied using large-scale molecular dynamics simulations. Simulation results of nanoscale pyramids under compression over contact lengths between $\sim 4 - 40$ nm are presented here. The contact area and force are accurately calculated during deformation, leading to predictions for the hardness (contact pressure) versus contact size that show nearly-quantitative agreement with experimental hardness versus contact size and that exhibit a scaling of $H \approx \ell_c^{-0.32}$. As found in the experiments, the MD hardness is also independent of the initial contact size and depends only on the current edge length. The MD simulation also allows for the deformation mechanisms to be determined through visualization. The simulations are extensive, not only including large sizes, large initial contact lengths, and large depths of indentation, but also including variations in temperature and stacking fault energy (by using different interatomic potentials).

5.1 EAM Potentials and MD Parameters

To initial confirm the potentials being used for these simulations were indeed the Auu3 and Au2 potentials the elastic constants of each must be checked. In order to check the potentials a simulation of a Au cube is constructed with dimensions of $a_o \times a_o \times a_o$ with four atoms. The cell employs full periodic boundary conditions and fixes the pressures to be zero using the Nose-Hoover barostat. The cube is slowly compressed to determine the (001) Youngs moduli and Poissons ratios for each potential. The resulting pressure vs. depth for each potential are shown in Figure 5.1. Since the moduli and ratios match the expected results perfectly we are confident the potentials are being implemented correctly and indeed they are the potentials we expect. Note that the moduli do not stay linear for very large displacements. Non-linearity becomes significant at strains of $\sim 1\%$. The non-linerity is due to the nature of the eam potential. The potential has an energy well that is only linear for very small deformations away from the equilibrium lattice constant. The experimental stacking fault energy for Au is 32 mJ/m^2 which would make Au2, with a stacking fault energy of 31 mJ/m^2, an obvious choice as the better potential to use in these simulations. Unfortunately, when this work was started the Au2 potential was not available, so the majority of the MD simulations are performed using the Auu3 potential. The effects of using different potentials will be discussed in the results section.

Beyond defining the potentials used for these simulations it is also necessery to define the damping cofficients for the Nose/Hoover thermostat. Damping parameters from Ch. 2 are defined as $Q = 10$ and $t_s = 0.25$ for ~ 0 K and $Q = 500$ and $t_s = 0.5$ for 300 K.

5.2 Au Pyramid structure

As-fabricated pyramids are built using the appropriate temperature-dependent lattice constant and are then relaxed for 200-2,000 ps at temperature until the energies, pressures, and temperatures converge in the absence of any applied loads. The pyramid is then compressed by an indenter of radius R through an applied force acting between the indenter and any Au atoms of the form $f(r) = -k(r-R)^2$ for $r < R$ and $f = 0$ for $r > R$ where r is the distance from the atom to the center of the indenter. We use a force constant $k = 100$ (eV/nm) and $R = 10,000$ nm to model a nearly rigid, nearly flat indenter. Different force constants have been studied and changes in this value do not affect the results. The indenter is displaced downward at a rate of 0.01 nm/ps. Note that for the largest pyramid, the simulation has been carried out to an indentation depth of 5.7 nm, which required 320 hours of CPU time on 400 Apple G4 processors on the Virginia Tech System X High-Performance Computational Facility.

The total force f_t is measured during indentation as the sum of the forces acting between the indenter and all the Au atoms. The contact area A is determined numerically using the projected area of all atoms interacting with the indenter. The numerical scheme accounts for slight overlaps and the non-symmetric deformations which occur at large indentation depths not included in simple volume conservation approximations. Other methods can be used to determine the contact area: such as counting the atoms in contact with the indenter and multiplying by a constant area, but the method used does not significantly affect the results significantly. The hardness is then $H = f_T/A$. When making comparisons to the experiments and to explain scaling effects, however, a more useful measure is the contact edge length ℓ_c. Since the contact area is nearly square at all times, $\ell_c = \sqrt{A}$ is accurate for the MD simulations. At large sizes where the existence of discrete steps on the facetted

surface becomes of less importance, the edge length can be related to the indentation depth δ through the average pyramid facet slope m as $\ell_c = [\ell_{ci} + 2\delta/m]$ where ℓ_{ci} is the initial contact edge length. The experiments discussed later determine ℓ_c through geometric considerations assuming constant volume plastic deformation as described by Wang *et al.* (2006).

Two types of fully three dimensional Au pyramid asperities are constructed with four sides comprised of (114) or (118) facets truncated near the peak to form a square top surface. Top and bottom surfaces have [001] normals, as shown schematically in Figure 5.2. The pyramid is truncated on the lateral sides, where dislocations never venture, to optimize the volume of material participating in the plastic deformation. Truncating the sides of the pyramid also optimizes the parallel computing. Since parallel MD simulations divide the volume of the simulation equally between processors, as opposed to dividing the atoms, it is more computationally efficient to reduce free space. Periodic boundary conditions are applied on the lateral (x and y) sides with a controlled zero pressure. Defining the pressure on the sides of the pyramid to be zero allows for expansion in the lateral directions and more accurately models a free pyramid. A small flattened region around the edge of the pyramid is included to eliminate the sharp angles that would otherwise exist due to the periodicity and that would cause spurious dislocation nucleation during testing. The vertical (z) displacements of the bottom three atomic layers of the pyramid are fixed at zero. The top surface is loaded by a nearly-flat indenter as described above. Several different pyramid sizes and shapes were studied to check scaling effects and to examine the influence of the fixed boundary location on the pressure and force. The details of the different simulations geometries are shown in Table 5.2. The important pyramid dimension is the initial contact length along the top surface; which controls the pressure necessary for the onset of plasticity and the ultimate scaling of the hardness. The edge

Table 5.1: Dimensions and important factors for each of the seven different MD simulations analyzed; T is the temperature, h is the height and b is the base length.

Pyramid	Potential	Facet	ℓ_c(nm)	T (K)	h (nm)	b (nm)	Atoms
1	Auu3	(114)	1.7	1	16.8	78.5	2,877,990
2	Auu3	(114)	1.7	1	42.1	91.4	15,603,067
3	Auu3	(114)	1.7	300	16.8	78.5	2,877990
4	Auu3	(114)	4.6	1	41.5	91.4	15,602,754
5	Auu3	(114)	8.6	1	63.8	130.1	50,506,734
6	Auu3	(118)	1.7	1	11.4	79.3	2,365,870
7	Au2	(114)	1.7	1	16.8	78.5	2,877,990

lengths studied here range between $\ell_{ci} = 1.7 - 8.6$ nm. The pyramids have heights that range between 17 to 60 nm, resulting in atom totals of 2,877,990 to 50,506,734. Two different slopes are examined: the (114) facets represent the majority of the simulations and a (118) faceted pyramid is studied to assist in the understanding and development of the energetics model.

5.3 MD Loading vs. Indentation Depth

Figure 5.3 shows the force versus depth for three simulations with the same initial $\ell_{ci} = 1.7$ nm but different heights and temperatures. The vertical line indicates the indentation depth ($\sim$2 nm) for which the dislocations in the smallest simulation reach the bottom of the simulation cell. The results show that the proximity of the fixed boundary has no affect on the results even beyond when the first dislocation reaches the bottom boundary. All subsequent simulation results shown here occur prior to this point and are unaffected by the boundary conditions, and thus effectively simulate infinite pyramids. The forces are determined in post-processing from the atomic configuration at a given instant and thus show some fluctuations relative to time-averaged forces. For an edge length of 1.7 nm a force of 10 nN can fluctuate by $\pm$0.5 nN corresponding to atomic vibrations of 0.004 nm. These fluctuations are small and

usually average out over a surface with some atoms closer and others further away. At small contact lengths, we obtain data every picosecond so as to capture the first drop in force and subsequently obtain data every 5-10 ps. Closer examination of the force data at small depths reveals slight differences in the depth at which the first drop occurs. It is unclear what exactly causes these differences. Only a very small amount of the differences in depth is due to elasticity ($\sim 1\%$), which is determined from a simple continuum model with similar geometries to the MD models. Without elasticity the only other possible cause of these differences is fluctuations in pressure. The first drop occurs at a depth of 0.25 nm and 0.35 nm for pyramids with heights of 16.8 and 42.1 nm, respectively. However, the forces at which these events occur are nearly the same. This motivates the use of contact edge length as a size measure in preference to simply the depth of indentation.

5.4 Effect of Temperature on MD

It is also important to examine the effect of temperature on the material response for the asperities. Most of the simulations are run at 1K in order to extract data relatively free of high frequency fluctuations. However to make comparisons with experimental work performed at room temperature, a single simulation is run at 300K. The load vs. depth for this simulation is also shown in Figure 5.3. As expected, there are larger fluctuations in the 300K simulation but the general force response is nearly identical to that obtained at lower temperatures. This result is not surprising since it has previously been shown that at low temperatures the mechanical properties of Au do not change significantly (Imura and Saka (1983); Zhang *et al.* (1995)). The simulations at both temperatures are run at high loading rates (10 m/s) compared to the experiments, and so thermally-activated phenomena remain largely prohibited even at 300K. Keeping this issue in mind, we will nonetheless compare simulations

at 1K with experimental data.

5.5 Pressure/Hardness Results

While force is an important measurement it does not capture the material response and size-scaling. Thus, the rest of the data will be presented in terms of contact pressure/hardness. The effective hardness is easily determined by dividing the force by the contact area, as mentioned previously. Now with both forces and areas measured, the pressure/hardness is calculated. The results are shown in Figure 5.4 as hardness (contact pressure) vs. contact edge length for four (114) pyramids with varying initial edge contact lengths and heights at T = 1K. The hardness initially increases rapidly with minimal change in contact length as the pyramid deforms elastically. Slight fluctuations arise due to the pressure modulations at the periodic boundaries and the large free surface area but they do not affect the pressures needed to induce plastic events nor the deformation mechanisms. At higher loads, the system stabilizes and the fluctuations dampen out quickly. Following the initial increase, the pressure reaches a critical value at which time a drop occurs. In previous studies of indentation these drops in load and pressure have been shown to accompany a plastic event in the form of a dislocation nucleation, Nix and Gao (1998). The exact deformation for this simulation will be discussed later. For initial edge lengths of 1.7, 4.6 and 8.6 nm, the first plastic events occur at pressures of 8.0-8.7, 5.2 and 3.6 GPa respectively. Thus, the pressure for the first plastic event decreases with increasing initial contact edge length, i.e. there is a size-scaling phenomenon. After a pressure drop, the pyramid then undergoes re-loading with a rapidly increasing pressure indicative of no change in contact area until another plastic event occurs. The second plastic events require pressures of 10.2-10.6, 7.1 and 5.5 GPa, for the three sizes, respectively. The pressure for the second event also decreases with increasing initial contact edge

length. Moreover, the pressure for the second plastic event is actually larger than for the first event, an unexpected phenomenon that must be understood mechanistically and quantitatively. We argue below that this hardening occurs due to dislocation interaction energies that are absent for the first plastic event. The scaling for the first two plastic events are shown in Figure 5.5 with scalings of $H \sim \ell_c^{-0.45}$ and $H \sim \ell_c^{-0.4}$ respectively. Each discrete plastic event results in a pressure drop followed by another elastic loading until the next critical pressure is reached again followed by a plastic event. This sequence continues clearly for several discrete plastic events up to $\ell_c \sim 15$ nm, beyond which the pressure drops and subsequent reloadings become more irregular and influenced by noise in the force and area measurements. The exact pressures at nucleation for larger edge lengths are also approximate since data is only collected every 10 ps and the nucleation events can occur between the data points. While exact hardnesses are not known the scaling of the hardness should still be captured. While the initial peak pressures and subsequent drops are of interest, the most important feature of the material response is that all the simulations converge to a common absolute magnitude and size-scaling with increasing contact length. Figure 5.4 shows that by $\ell_c = 10$ nm all simulations have the same response. This size-scaling would not be apparent if the data were examined with respect to indentation depth. Thus, the hardness of the material depends only on the current contact area or edge length after an initial transient stage. Hence, the hardness is independent of the prior history of deformation, i.e. there is a unique size-scaling of the hardness. This result is in general agreement with experiments as shown later.

5.6 Deformation Mechanisms

Several stages of deformations are depicted in Figure 5.7a-c where only atoms with a high centro-symmetry parameter, Kelchner *et al.* (1998) i.e. atoms not in a perfect

FCC structure, are shown. The first onset of plasticity is always the formation of a stacking fault half octahedron (SFHO) (Figure 5.7a), created by the simultaneous nucleation of four $a/6(112)$-type partial dislocations along the four (111) planes intersecting the four contact edges of the specimen. The SFHO consists of stacking faults, on each of the (111) planes, that intersect along [110] directions to form energetically favorable junctions with a $a/3[100]$ Burgers vector bounded by the top (001) surface. Figure 6.3 shows a schematic of the SFHO structure and the burgers vectors involved in the formation of the structure. For the largest contact length studied here, 8.6 nm, the nucleation occurs at the corners of the top surface as two Shockley partials spread along the adjacent (111) planes with the [110] junction. With increasing pressure and indentation depth, a second SFHO is nucleated from the now-larger contact edge, in what is the beginning of a sequence of nested SFHOs that form with increasing indentation depth.

Under further compression, the [100] junctions can act as sources for the formation of new partial dislocations which emit into the body with Burgers vectors in the direction of the facet surface, as seen in Figure 5.7b. The emission occurs for each (111) plane in either direction but all four partials always extend in the same clock/counter-clock wise direction for the four different planes. Further emissions can also occur in opposite directions to the previously nucleated partials. Once emission begins there are many complicated interactions between the dislocation structures with previously nucleated dislocations and subsequent nucleations. These extra dislocations form and annihilate, but are inhibited by the subsequent SFHO formation, as seen in Figure 5.7c where spreading for a majority of the stacking faults has been suppressed while others have expanded past the last SFHO and a full dislocation has been created. After the first few SFHOs, the expansion of the stacking faults can also act as barriers for the formation of a subsequent perfect SFHO

These interactions can also have an effect on the nested nature of the SFHOs. Once dislocation nucleation begins the interior SFHOs can begin to rotate to form twins between interior and exterior SFHOs. Since the nested SFHOs, in some cases, are separated only by a single plane of atoms, it is energetically favorable to eliminate the stacking fault spacing that could only be one atomic plane. A rotating of one of the nested SFHOs relative to the next nearest SFHO eliminates the space between the stacking faults and results in a twin boundary. Figure 5.8 shows how the surface atoms dissipate the high energy structures with rotation and twinning. The twinning results in a healing on the opposite face of the SFHO and also creates a surface step that is associated with the partial dislocation that was previously emitted from the junctions. The formation of steps confirms that the nucleated dislocations have a different Burgers vector than those nucleated to form the SFHOs.

As the dislocation activity continues via nucleation of new dislocations the spreading begins to take on a four-fold symmetry as specific (111) planes begin to dominate the slip. Figure 5.9 shows the deformation of the atoms with a high centro-symmetry parameter as seen from the bottom of the pyramid once the four-fold symmetry has begun to develop. The deformation is seen to develop in a controlled manner moving short distances in a fairly symmetric fashion as suggested by the spatial range of the elastic stresses. Figure 5.10 just how the range of the maximum resolved shear stress in the pyramid is quite limited. Due to the self similar structure of the pyramid the range of the stress field should have the same shape independent of the edge length which limits the range of the driving force for dislocations to a function dependent on the current edge length. Beyond the range of the dislocations the formation of full dislocations is seen in Figure 5.9 which further suggests an ultimate change in deformation mechanisms away from the spreading of partial dislocations with large stacking faults.

5.7 Effect of Geometry and Potential on MD Hardness

The simulations presented thus far have focused on the most common pyramid structure found on polished surface using a single atomic potential. While (114) faceted pyramids are the most energetically favorable surface asperities other geometries do exist randomly on polished surfaces. Also, the potential used thus far, Auu3, is a reasonable potential for elastic response but under estimates the stacking fault energy which might influence nucleation pressures and hardness convergence. In order to determine what affect each of these factors has on the MD simulations, different simulations are performed on a (118) faceted pyramid as well as a (114) pyramid using the Au2 potential with a more realistic stacking fault energy (31 mJ/m^2). The results for these simulations are shown with respect to the (114) faceted pyramid using the Auu3 potential in Figure 5.11. The (118) pyramid has the same initial contact edge length as the smallest (114) pyramid but has a larger $\Delta L = 2.02$ nm which accounts for the shallower geometry of the facet. The larger ΔL is clearly seen in the hardness data with jumps in edge length of 2.02 nm accompanying each hardness drop, rather than alternating values of 0.86 and 1.44 nm. For the (118) pyramid the first pressure necessary to induce plasticity is approximately the same as that for the (114) pyramid. The fact that the initial peak pressures are so close suggests that the first pressure is a nucleation process purely dependent on the current edge length and does not depend on the structure after deformation. This will be discussed further in the next section. The pressure after nucleation, on the other hand, is substantially lower than that of the (114) pyramid. This large drop again will be discussed further in the next chapter but should be dependent on the fact that the change in contact area after the first nucleation is much larger for the (118) pyramid versus the (114).

Again the important aspect of the MD simulations is that the hardness eventually converges to a similar value to that of the (114) pyramid at larger edge lengths which again suggests that the scaling eventually only depends on the current edge length.

The simulation using the Au2 potential has nearly the exact same response as the Auu3 potential as seen in Figure 5.11. The peak pressures and hardness convergence do not show any significant differences. The similarities suggest that the stacking fault energy does not have any significant influence on the response of the asperity up to energies of $\gamma_{sf} = 0.32$ eV/mJ^2. These stacking faults are still small relative to the energies of other models. To determine the true influence of stacking fault energie a study of a material with a much larger value should be studied.

5.8 Unloading of Single Asperity

For contact problems the permanent plastic deformation is always an important aspect of analysis. By unloading the pyramids at different stages of the deformation, the amount of permanent plastic deformation can be determined as well as the unloading modulus of the system. The unloading has been checked at several different stages of indentation including after the first SFHO nucleation, after three SFHOs have been nucleated, and finally just before dislocations reach the bottom of the simulation the load vs. displacement curves are shown in Figure 5.12 with the "x"'s representing the three unloading points. For the first unloading after the nucleation of the first SFHO, the structure simply returns to its initial structure with no permanent plasticity. Along with the structure returning to its initial structure the energy is also completely recovered. Any energy lost due to motion of dislocations is small and thus the indentation process at this point is completely reversible. The second unloading, after three SFHOs have been nucleated is not reversible but shows very

little permanent plasticity. The difference for this unloading is that a single dislocation has passed beyond the nested SFHOs. The pyramid does return to perfect internal fcc structure but there is net mass transport via the dislocations nucleated from the SFHO junctions and the twinning from the top to the sides of the pyramid. This is represented by the 12.53 eV of unrecovered energy which is the difference in areas under the loading and unloading curves as calculated from Figure 5.12. The final unloading, however, shows significant permanent plasticity, as seen in Figure 5.13 with much of the material transported to the facets resulting in a much larger final contact area. This is related to so-called trench filling, an important feature in understanding nanoscale friction. The hysteresis due to this atomic rearrangement is large. At a depth of 3.3 nm the $\ell_{ci} = 1.7$ nm simulation has reached a current edge length of $\ell_c = 52$ nm and the total energy input to the system is $\sim 12 \times 10^3$ eV. Upon unloading $\sim 4 \times 10^3$ eV are recovered which leaves $\sim 8 \times 10^3$ eV of unrecoverable energy. Some of this energy is stored in the system in form of dislocations and geometric changes associated with change in total energy of the MD system which is ~ 1130 eV . This leaves a significant amount of energy that has been dissipated due to either dislocation motion. This difference in energy must be that which was dissipated by the Nose-Hoover modeling methods which dampen the energy to control the temperature and the pressure.

5.9 Comparing MD with Experiments

To elucidate the scaling of the hardness with the contact length and to make a connection with the experiments by Wang *et al.* (2006), Figure 5.14 shows the hardness versus contact edge length for four pyramids with initial contact edge lengths of 36.2, 36.3, 46.3 and 78.2 nm compared to the MD results in a log-log plot. The

initial edge lengths are not seen in the data due to the data appearing in a log-log form. The initial contact length for the experiments was deduced using a local stiffness approach Wang *et al.* (2006). Due to the self-similar nature of the pyramids when the contact areas for the pyramids are the same the local stiffness for each pyramid will be the same. Knowing this fact allows for calibration of the contact area for different size pyramids. The experimental data shows the same trend as the MD results: an initial transient rise during flattening of the as-fabricated pyramid top that is presumably accompanied by some initial dislocation nucleation, followed by a power-law softening of the pressure versus contact edge length. The gap in size scale between simulations and experiments is less than a factor of 3; the simulations extend to 37 nm and the experiments, although starting as small as 36 nm, begin showing power-law softening at $\sim$ 100 nm. Not only is the softening trend similar between the simulations and experiments, but the absolute magnitude of the pressure differs by less than a factor of 2 between the end of the simulations and the beginning of the experiments, with the data sets able to be connected by a single smooth curve. This level of agreement between MD and real experiments is unprecedented, and is due to three factors: (i) the exceptional uniformity of the real fabricated pyramids with regard to structure, single-crystal nature and orientation, and the absence of pre-existing dislocations, all of which are reproduced in the MD model, (ii) the ability to perform normal compression tests on these samples, and (iii) the ability to perform large-size MD simulations with extensive amounts of deformation.

Comparing the simulations and experiments in more detail, both show power-law scaling, but with different exponents. The experimental hardness scales with a range of $H \approx \ell_c^{-0.55} - \ell_c^{-0.91}$ and has an average value of $H \approx \ell_c^{-0.75}$, which is somewhat softer than the MD data, which scales as $H \approx \ell_c^{-0.32}$. Power-law scaling is not expected a priori, although a variety of power-law behaviors have been observed in different

experiments, due to material characteristic lengths and other mechanisms Greer *et al.* (2005); Greer and Nix (2005); Sieradzki *et al.* (2006); Volkert and Lilleodden (2006). One example of this is the indentation of (001) Au single crystals Nix *et al.* (2007). This data is also shown in Figure 5.14 by squares and triangles. These experiments were performed using a Berkovich indenter with a tip radius of 45 nm. While the data was initially reported in terms of depth this can easily be converted to an edge length for the known indenter geometry. The geometries between the Berkovich indenter and the pyramids are surprisingly similar and should result in increases of contact area that are approximately the same at a given depth of indentation. The indentations show a response nearly identical to the experiments performed on the pyramids. The indentations also approach the values of the MD with a $H \approx \ell_c^{-0.5}$ scaling. The indentation data further supports that at small length scales the size-scaling depends on the edge length. Clearly to fit, a single (nonpower-law) smooth curve through the entire set of data, experimental and simulation, requires a curve with multiple slopes representing varying scaling parameters. The varying scaling parameters with increasing pyramid size suggest a possible mechanism change from MD to experiments. Thus the deformation mechanisms observed in the MD, which lead us to a model for the size-scaling of the hardness is discussed next.

The MD and experiments result in several key findings. First, the initial and second peak pressures scale with the edge length as $H \approx \ell_c^{-(0.4-0.5)}$. Second, the second peak pressure is higher than the first nucleation pressure. Third, the hardness ultimately converges to a common scaling that is independent of deformation history with $H \approx \ell_c^{-.35}$. Fourth, there are well defined dislocation structures which store the plastic energy and the size is set by the edge length. Fifth, the majority of the energy is either reversible or stored in dislocation structures and little is dissipated in dislocation motion. Finally, there is a transition in the scaling between

the MD and Experimental lengths which could be due to a mechanism transition to the nucleation of full dislocations from the preexisting SFHO structures. Now with the deformation mechanisms understood, the scaling as well as local features of the pressure are explained through the development of an energetic model.

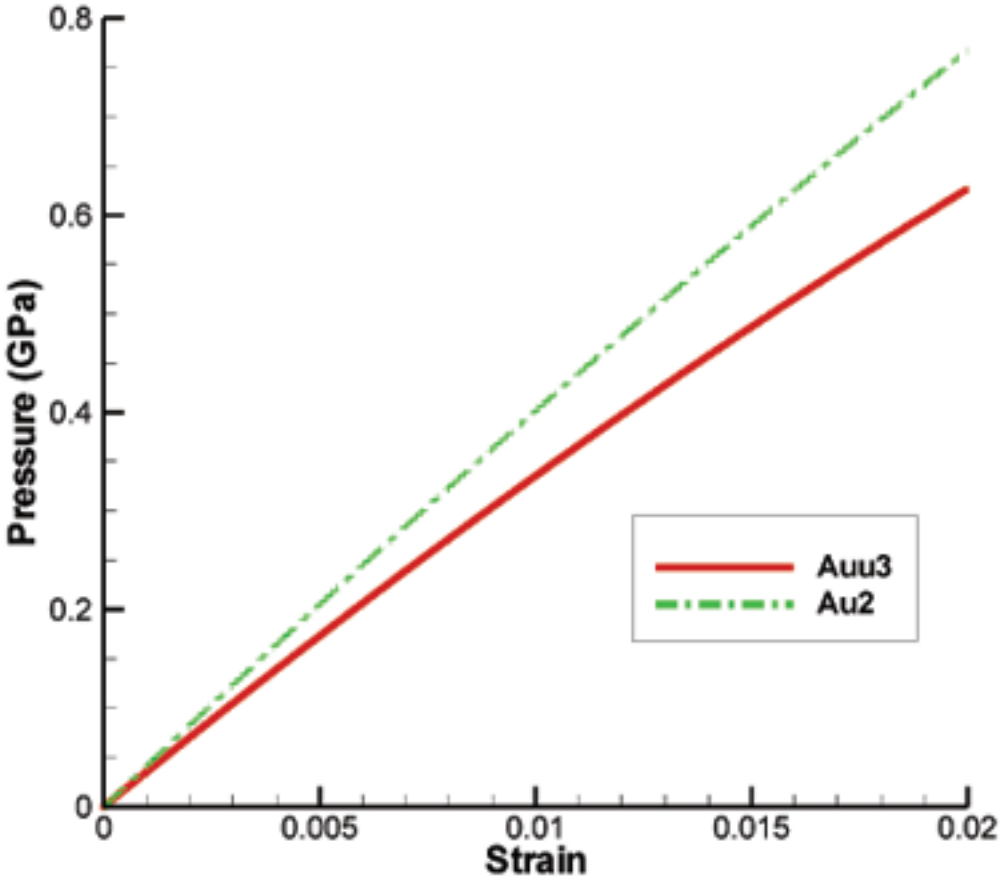

Figure 5.1: Stress-Strain curves for the Auu3 and Au2 potentials for compression in the (001) directions. The (001) Young's Modulus is determined from a linear fit at small strains.

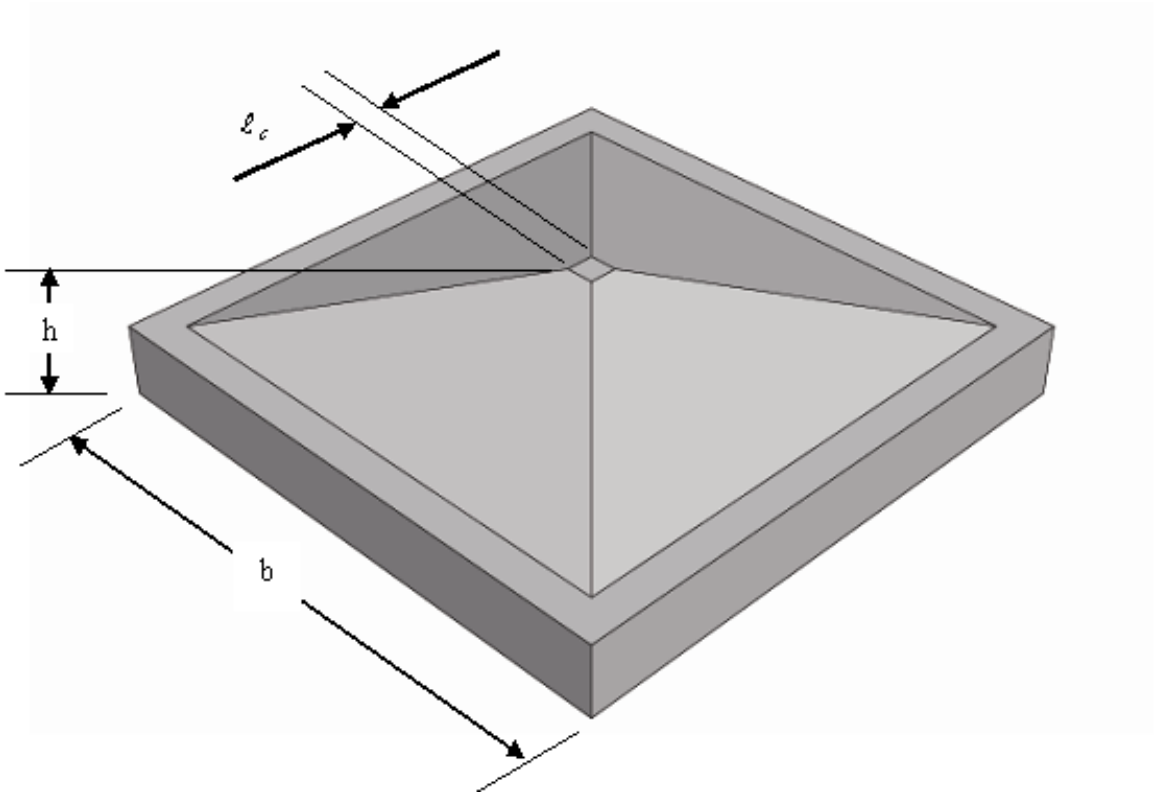

Figure 5.2: Schematic of molecular dynamic simulation. With base size b, total height h and initial contact edge length ℓ_c.

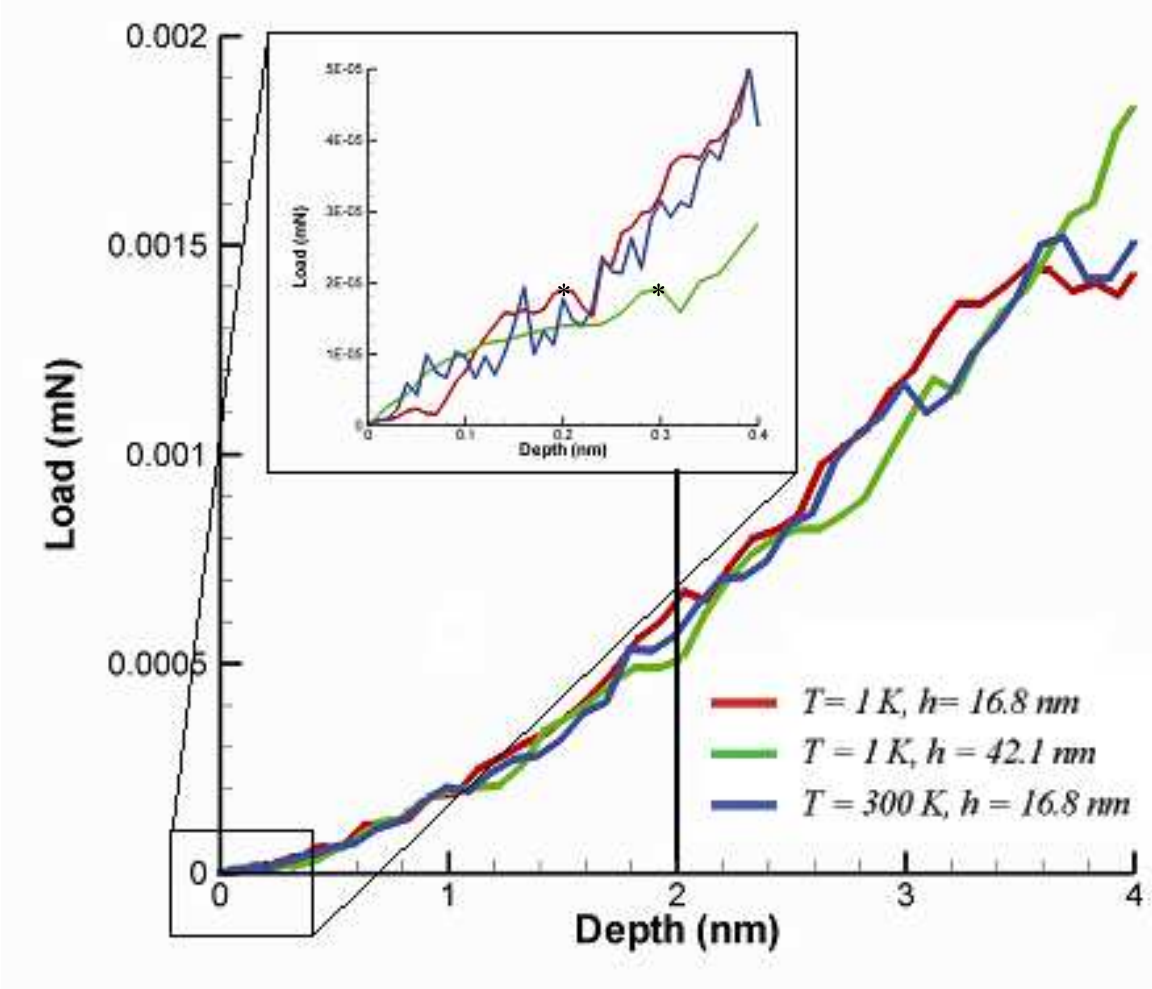

Figure 5.3: Force-displacement curve for three simulations with the Auu3 potential and initial edge length of 1.7nm with different total sizes and run at different temperatures, as defined by Table 5.2; with the inset showing a blow up of the response at small displacements including the first force drop which occurs at the same load for large and small systems.

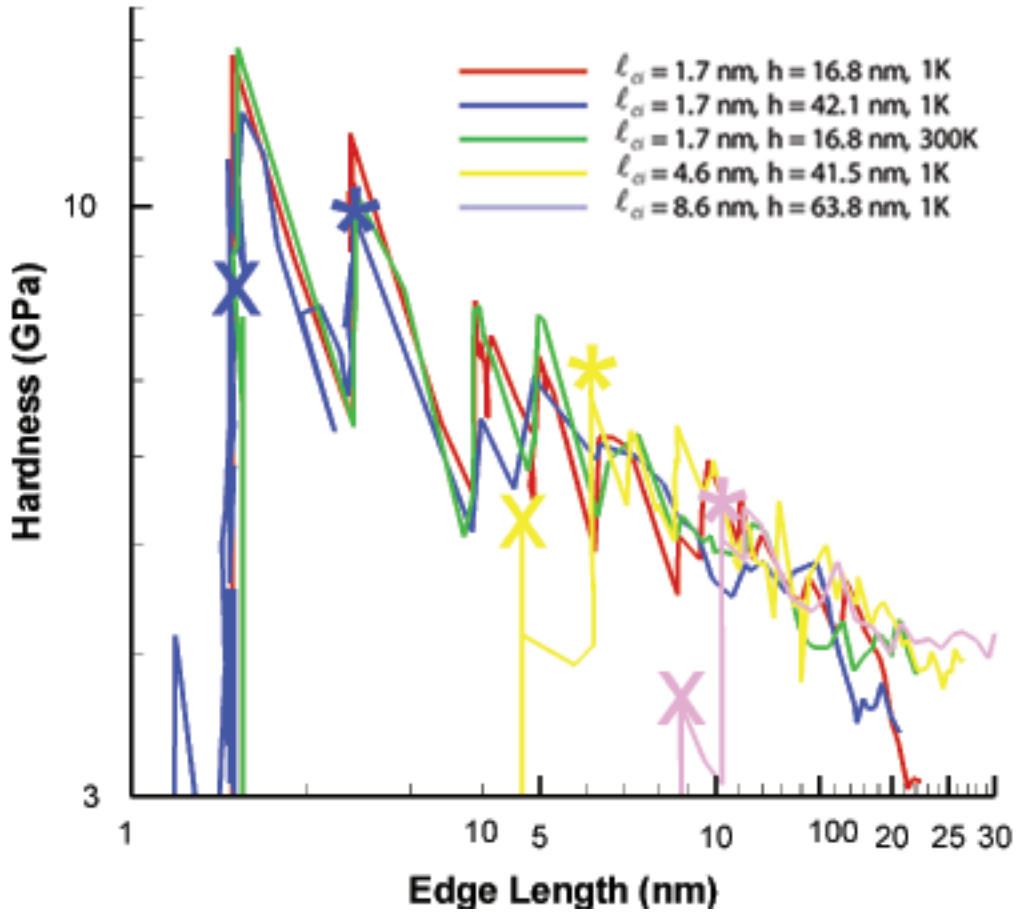

Figure 5.4: Hardness for the 5 different MD simulations of (114) pyramids performed using the Auu3 potential. The first peak hardnesses are labeled with an "x" while the second peak hardnesses are labeled with a "*".

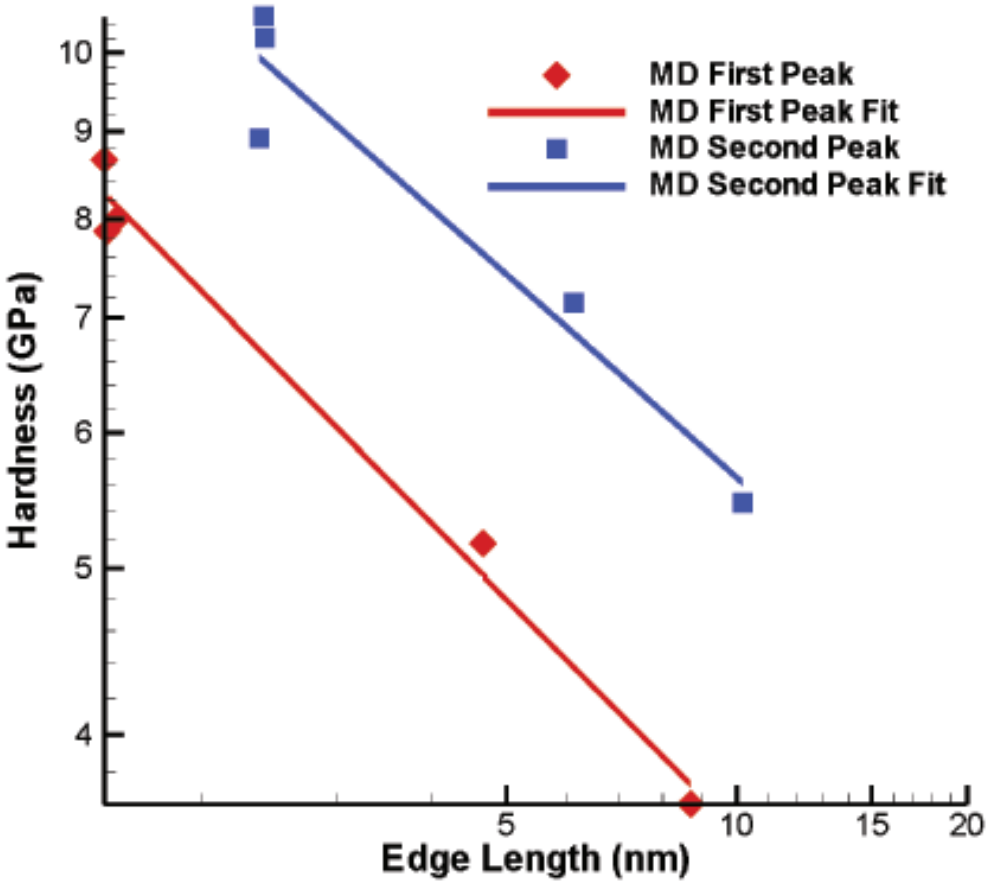

Figure 5.5: Scaling for the first two hardness peaks of the MD simulations as a function of edge length. The scaling for the first peak (red) is $H \sim \ell_c^{-0.45}$ and the second peak (blue) is $H \sim \ell_c^{-0.4}$.

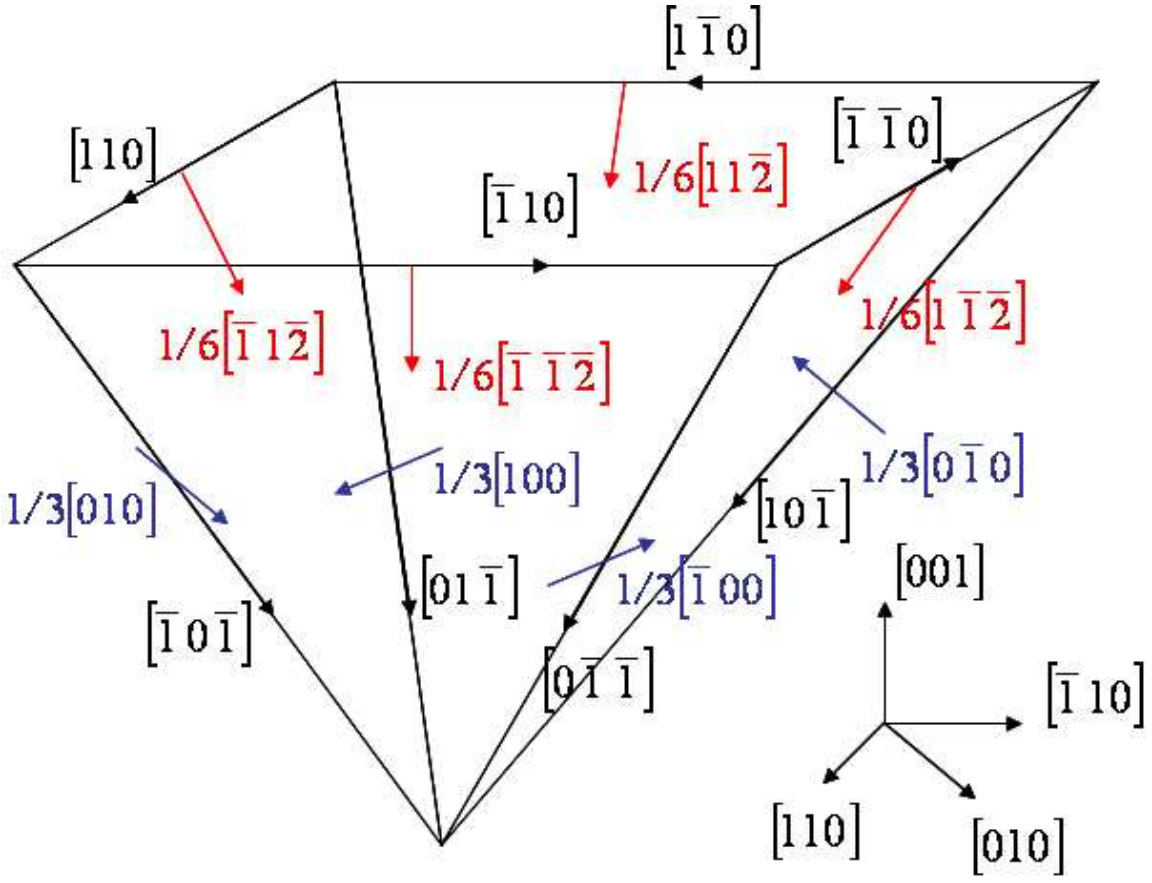

Figure 5.6: Schematic of the stacking fault half octahedron burgers vectors and line senses, line sense (black arrows) and burgers vectors for the initial partial dislocations (red arrows), and [001] junctions formed (blue arrows).

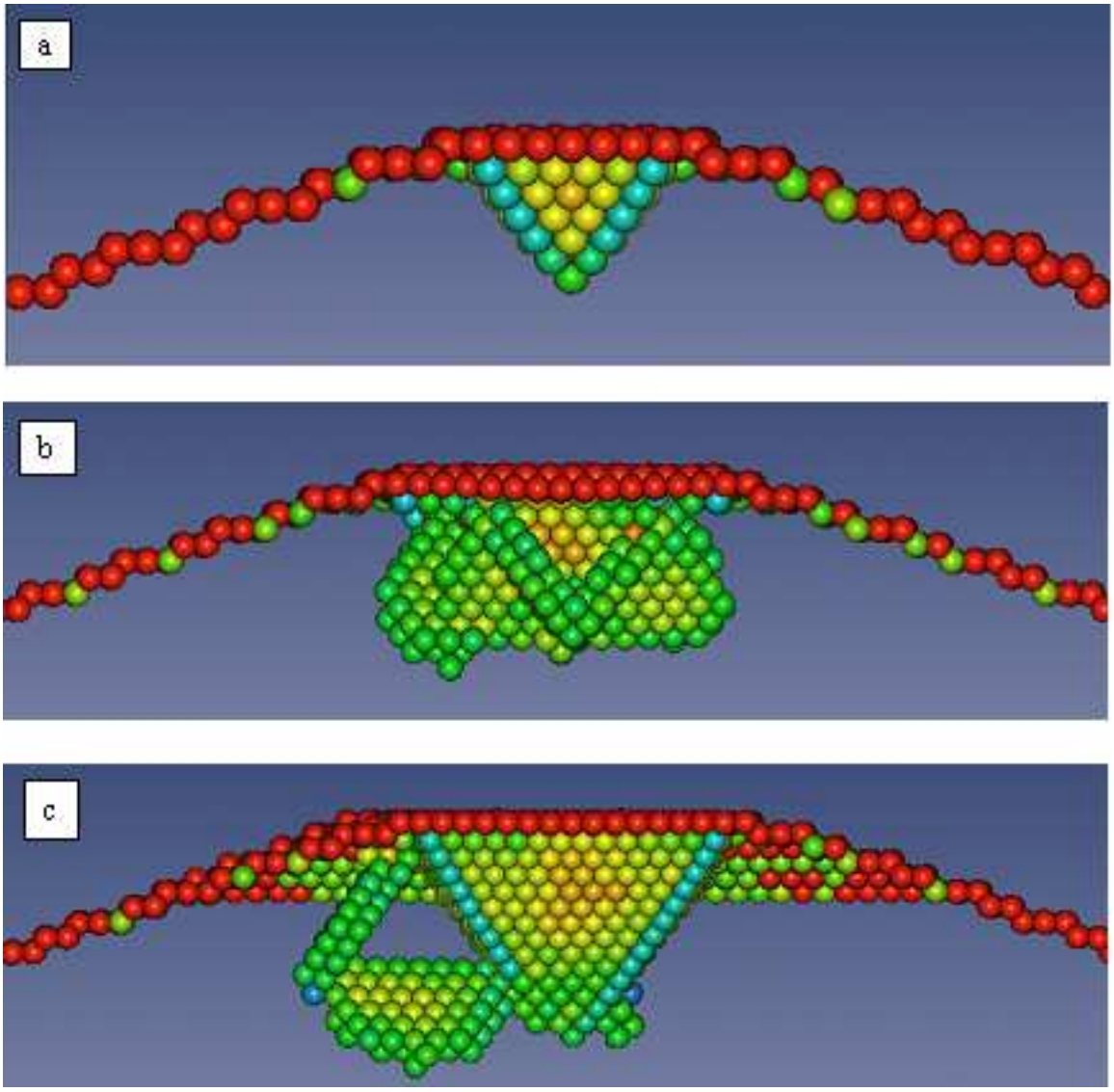

Figure 5.7: Views of the atomic structure after various depths of compression; a) after the first SFHO; b) showing early stages of dislocation nucleation from SFHO junctions; c) after formation of the third SFHO, showing formation of one full dislocation loop. Colors are assigned based on the Centro-Symmetry parameter Kelchner *et al.* (1998).

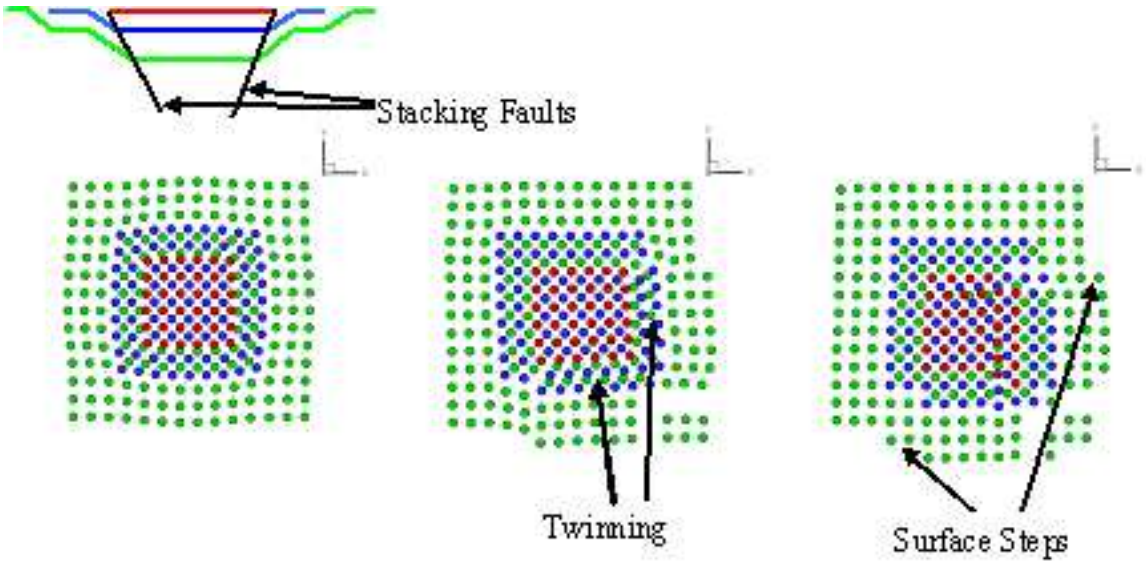

Figure 5.8: Images of the surface atoms evolution during the compression; a) the first and second layers have been injected into the third layer; b) twinning and rotation begin which annihilate some of the stacking faults; c) the rotation and twins result in dislocations passing to the facets resulting in surface steps. Atoms are colored according to their initial layer position from top to bottom: Red-Blue-Green.

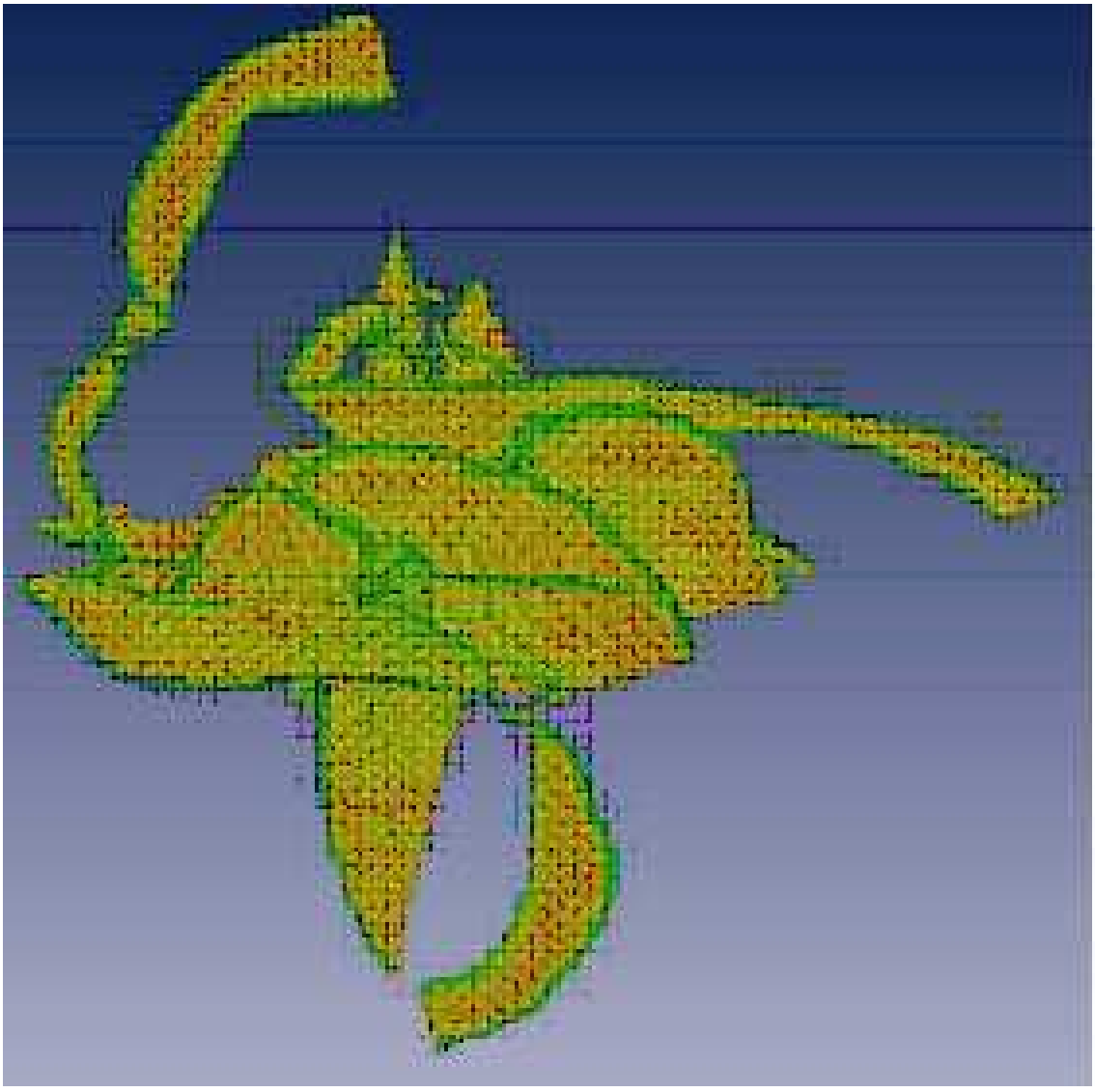

Figure 5.9: Deformation at a late stage of compression, as viewed from underneath the pyramid. Colors are again assigned based on the Centro-Symmetry parameter Kelchner *et al.* (1998).

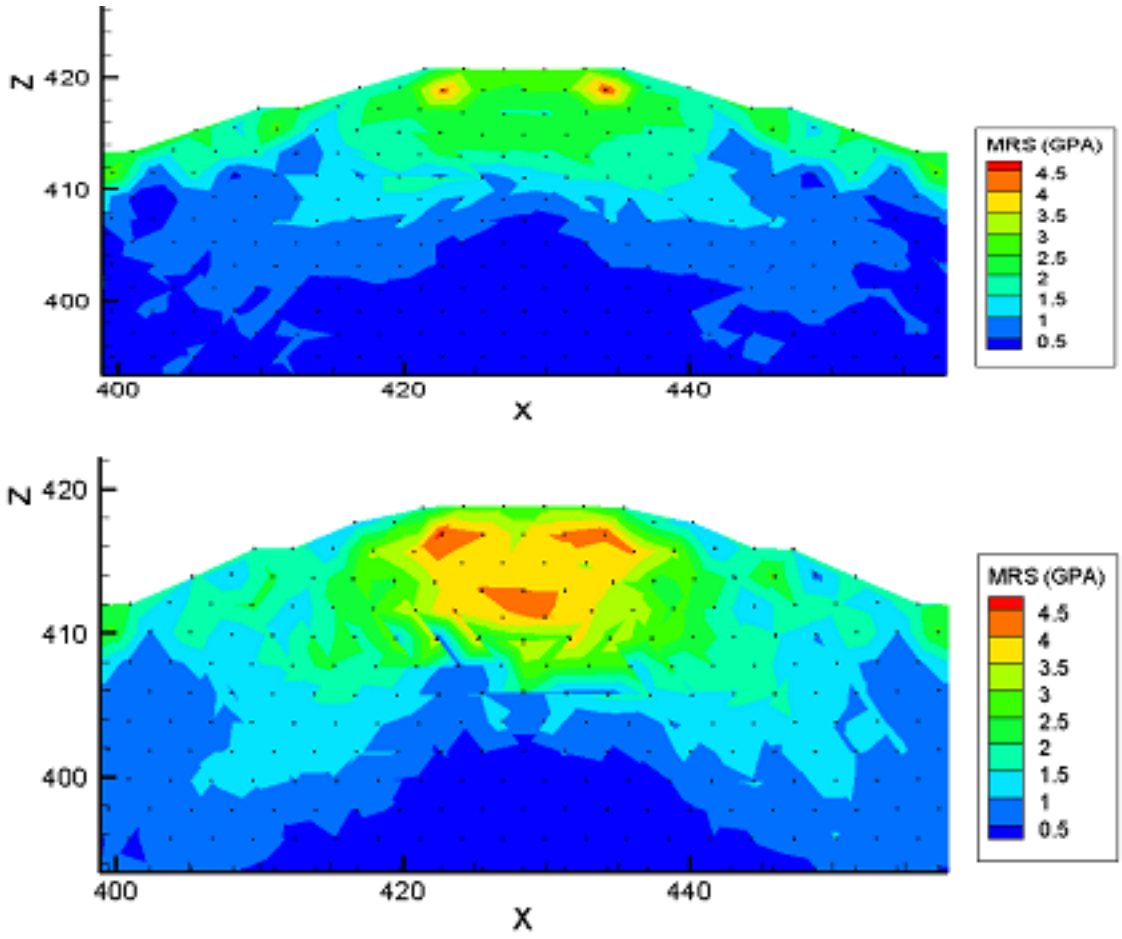

Figure 5.10: The maximum resolved shear stress(MRS) determined by the molecular dynamics; a) just before the first SFHO nucleation; b) just after the nucleation of the first SFHO

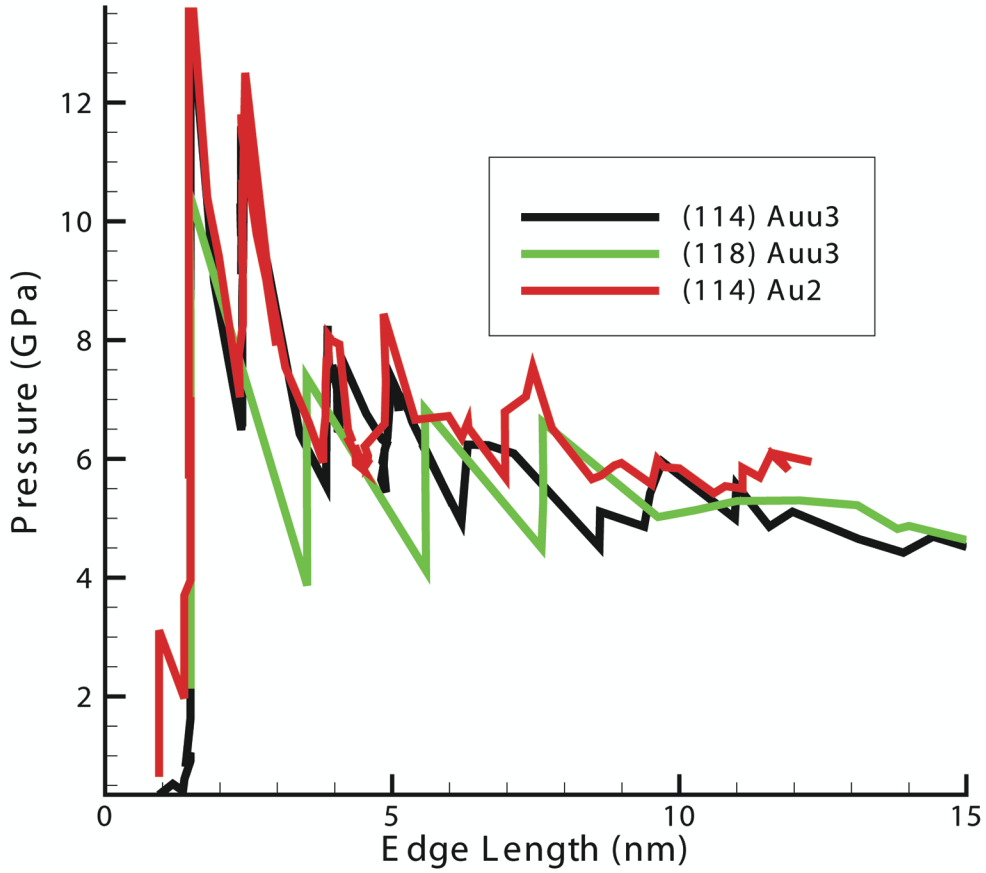

Figure 5.11: Hardness for two MD simulations run with 1) different geometry,(118) facets, and 2) a different potential, Au2, compared with the $h = 16.8$ nm (114) control pyramid. The (118) pyramid has the same $\ell_c = 1.7$ nm as the control pyramid while the Au2 potential simulation uses the exact same atomic structure as the control.

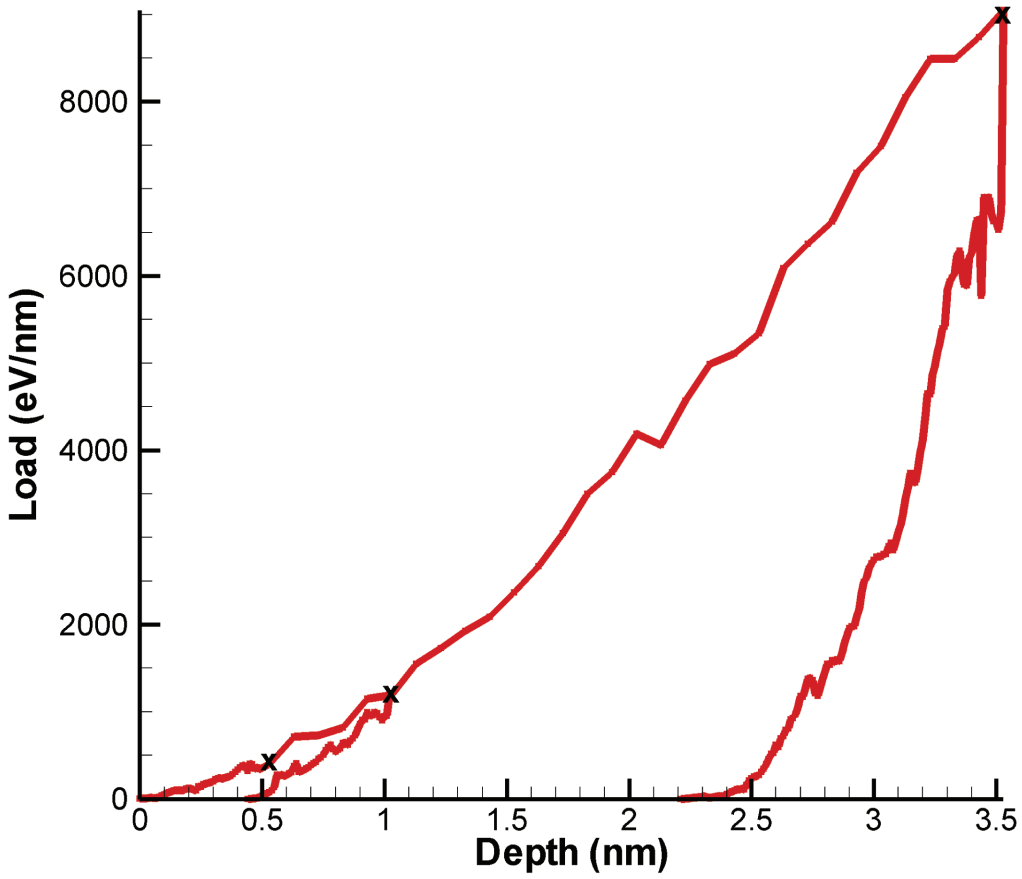

Figure 5.12: Unloading of the pyramid, with $\ell_c = 1.7$ nm and a height of 16 nm, at three different positions marked by the "x"s, i) after the first SFHO formation, ii) after three SFHOs and iii) after a significant amount of plasticity.

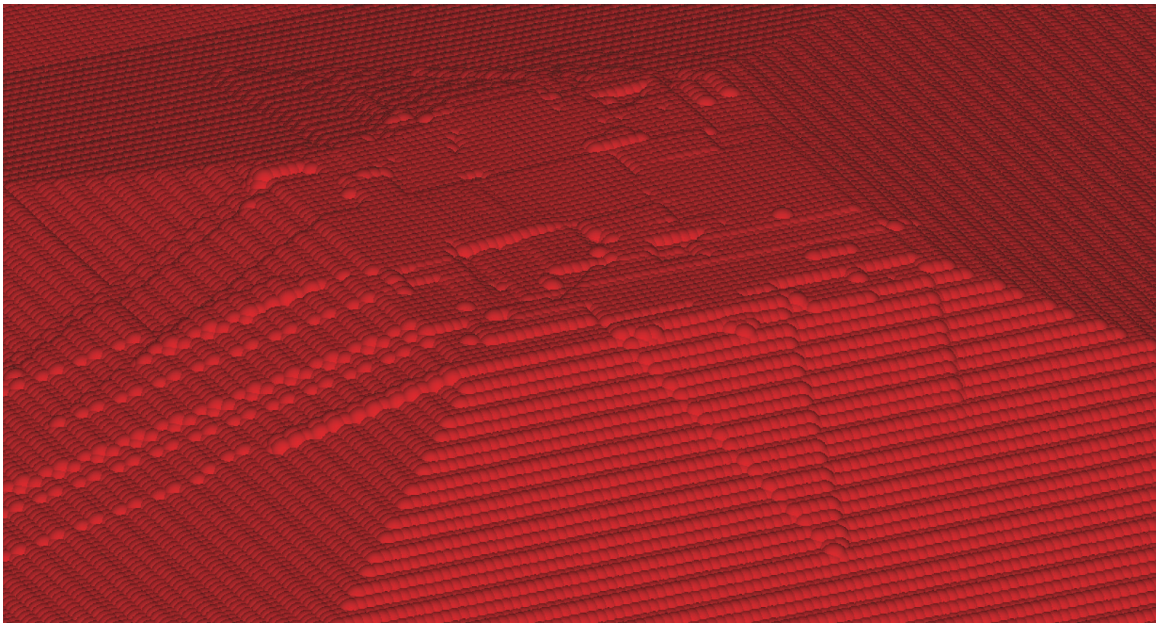

Figure 5.13: Atomic positions of surface atoms after unloading of the structure with clear surface steps and permanent plastic deformation.

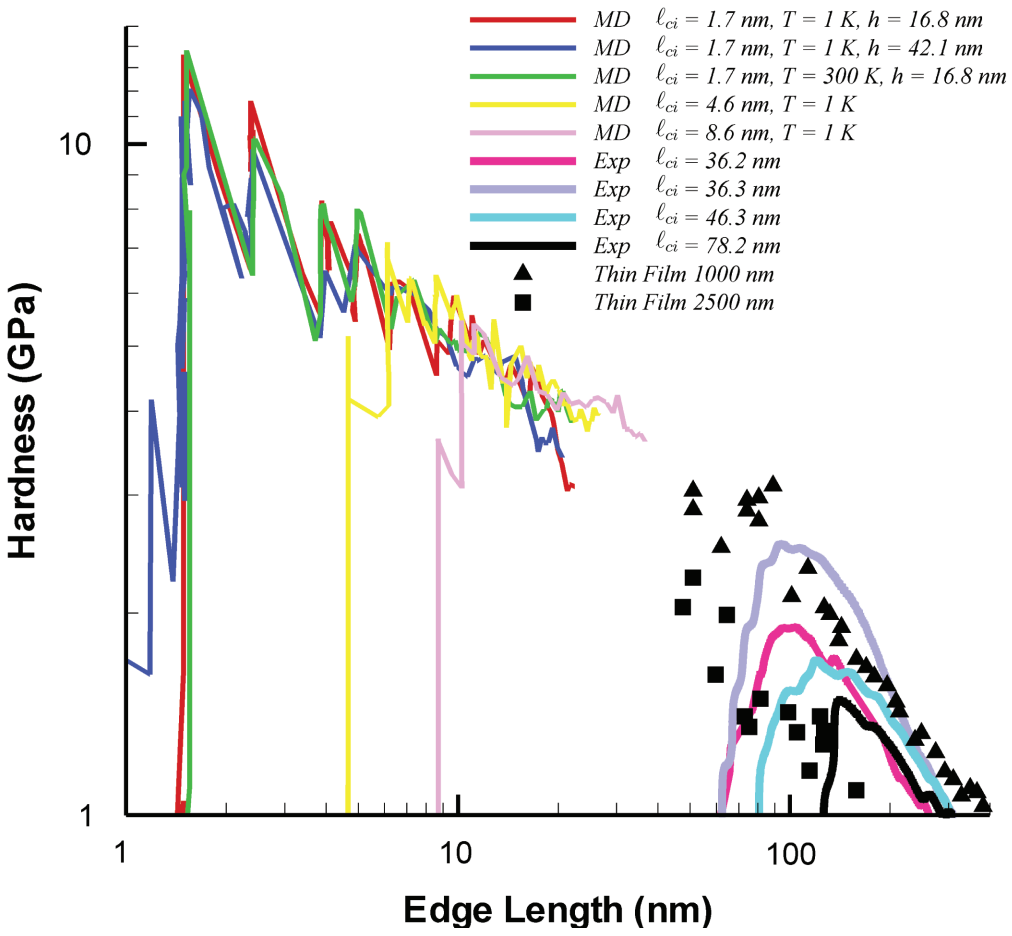

Figure 5.14: Log-log plot of the hardness vs. edge length for the MD simulations the Wang and Nix experiments.

Chapter 6

Energetic Model for Size-Dependent Plasticity

6.1 Development of Energetic Model

6.1.1 Energetic Model Formulation

The deformation mechanisms controlling plasticity during compression of a nano-asperity are now well defined from the MD simulations. Based on the observed deformation mechanism of stacking fault half octahedrons (SFHOs), an energy-based model is developed to predict the minimum pressure necessary to form a sequence of SFHOs, and thus obtain the scaling of hardness versus contact size for lengths of 10 nm $< \ell <$ 100 nm. The model determines the applied force necessary to provide sufficient energy to nucleate each successive SFHO into the material containing the prior SFHO structures, and is conceptually similar to the model of Gerberich *et al.* (2006).

The total energy inequality compares the change in external loading to the change in elastic energy plus the energy associated with injecting new dislocations in the form

of an SFHO as shown schematically in Figure 6.1. The general energy inequality for the process is

$$\delta W_{ext} > \delta U_e + \delta U_{dis} + \delta U_\tau + \delta U_S \tag{6.1}$$

Here, $\delta W_{ext} = f\Delta u$ is the external work done on the system by the indenter and $\delta U_e = U_e^f - U_e^i$ is the difference between final and initial stored elastic energies. Furthermore, δU_{dis} is the total energy change in the dislocation structure, including the self energy of the new SFHO, the image interactions with the pyramid, and interactions between the dislocations in the SFHO, and interactions with prior SFHOs. The term δU_τ is the work done by SFHO dislocation motion against the applied field and δU_S is the change in surface energy associated with loss of atomic ledges on the surface due to injection of the SFHO into the bulk of the pyramid. Below, we evaluate each energy term in detail.

At contact length ℓ_c and applied force $f = P\ell_c^2$, the stored elastic energy before nucleation is

$$U_e^i = (\alpha\ell_c^3)(P_i^2/2E) = \alpha f^2/2\ell_c E \tag{6.2}$$

where E is the elastic modulus for the (001) crystal orientation and α a dimensionless compliance parameter which sets the effective volume for the elastic strain energy. After nucleation, the geometry and force changes yield an elastic energy of

$$U_e^f = (\alpha(\ell_c + \Delta L)^3)(P_f^2/2E) = \alpha(f + \Delta f)^2/2(\ell_c + \Delta L)E \tag{6.3}$$

where Δf is non-zero under constant displacement conditions (see below). The change in elastic energy is the difference of Eqs. 6.3 and 6.2.

The energy associated with introducing a new SFHO structure, δU_{dis}, is comprised of two major components, the SFHO self energy and the interaction energies among all the SFHO dislocations. From simple geometry, each SFHO generates a

total dislocation line length of $4\ell_c$ with energy $4w_{self}\ell_c$ where w_{self} is the core energy per unit length of the [100] dislocations making up the SFHO. Each SFHO also generates a total stacking fault area of $\sqrt{3}\ell_c^2$ with energy $\sqrt{3}\gamma\ell_c^2$ where γ is the stacking fault energy. The core and stacking fault are associated with the energy of the final structure only. The image energy per unit length of each dislocation in the SFHO is due to interaction with the free surface during insertion of the SFHO, and is denoted by w_{im}. The interactions among all the various dislocations are complicated and difficult to handle exactly. Symmetry of the SFHO structures in the pyramid permits some simplifications, and a few assumptions will be made to capture the most important interaction energies. First, all interaction energies will be excluded except those between the four dislocations comprising a single SFHO, denoted as w_{sfho}, and those between a newly nucleated dislocation in the SFHO and the N nearest parallel dislocation in the previously-formed SFHOs, denoted as $w_{||}$, where N will be chosen below.

The work necessary to move the dislocations, U_τ, is defined through an average shear stress τ acting over the slip plane. The shear stress is related to the applied load as $\tau = C_\theta \cos\theta f/(\sqrt{3}\ell_c^2)$, where C_θ is a parameter accounting for the averaging of the stress over the area $\sqrt{3}\ell_c^2$ of the slip planes and θ is the angle between the applied load and the slip plane. Once τ is determined, the work done in moving the partial dislocations forming an SFHO is determined through $U_\tau = Ab_p\tau$, where A is the swept area $\sqrt{3}\ell_c^2$ and b_p is the partial burger's vector. Combining all of the above terms yields the work to move the dislocations of $U_\tau = C_\theta b_p \cos\theta f$.

The final component of energy is the change in surface energy, δU_s arising from the annihilation of an atomic ledge. We denote the ledge energy per unit length as E_L. The total length of annihilated edge is the same as the length of nucleated dislocation, $4\ell_c$, and hence $\delta U_s = 4\ell_c E_L$.

We insert the various energy contributions into Eq 6.4 and rearranged such that external work and initial internal energy are on the left side of the inequality while the internal work and final energies of the system after the formation of a new SFHO are on the right side. To simplify the notation, we factor out the edge length ℓ_c and write the total of the interaction and ledge energies per unit length as $W = w_{self} + w_{sfho} + w_{||} + w_{im} - E_L$. The energy inequality then reads

$$f\Delta u + \frac{\alpha f^2}{2\ell_c E} > \frac{\alpha(f+\Delta f)^2}{2(\ell_c+\Delta L)E} + \sqrt{3}C_\theta b_p \cos\theta f + \sqrt{3}\gamma\ell_c^2 + 4\ell_c W \tag{6.4}$$

At small f, the inequality cannot be satisfied. As f increases, a critical value is reached at which there is equality, indicating that it is energetically feasible for a new SFHO to exist in the system. Equality in the energy equation thus sets a lower bound for the force necessary to nucleate the next SFHO. Upon formation of the new SFHO, the pyramid has a new edge length $\ell_c + \Delta L$ and new internal energy and dislocation structure.

With the energy now described generally, we examine loading under the conditions of constant force and constant displacement. Neither case describes the actual loading exactly due to the finite elasticity of the indenter that has not been included in the energy, thus the two cases represent limiting situations, usually differing by small terms. For constant force, $\Delta f = 0$ and the displacement change Δu must be computed as follows. The total displacement consists of elastic and plastic components $\Delta u = \Delta u_e + \Delta u_p$. The change in elastic displacement is $u_e^i - u_e^f$ where $u_e^i = \alpha f/E\ell_c$ and $u_e^f = \alpha f/E(\ell_c + \Delta L)$. The change in plastic displacement is simply the z component of the burgers vector for the nucleated partial dislocations, $u_p = b_p \cos\theta$. Thus the displacement change is

$$\Delta u = u_e^f - u_e^i + u_p = \frac{\alpha f}{E(\ell_c+\Delta L)} - \frac{\alpha f}{E\ell_c} + b_p\cos\theta = \frac{-\alpha f \Delta L}{E\ell_c(\ell_c+\Delta L)} + b_p\cos\theta \tag{6.5}$$

For constant displacement, $\Delta u = 0$ and we must compute the change in force Δf. The total displacement is again defined by an elastic and plastic component, but now with a change in the force and zero total displacement. Specifically,

$$0 = u_e^f - u_e^i + u_p = \frac{\alpha(f + \Delta f)}{E(\ell_c + \Delta L)} - \frac{\alpha f}{E\ell_c} + b_p \cos\theta \tag{6.6}$$

Solving for Δf gives

$$\Delta f = \frac{f\Delta L}{\ell_c} - \frac{b_p E(\ell_c + \Delta L)\cos\theta}{\alpha} \tag{6.7}$$

We can now write the energy equality equation for either loading condition. For constant force, we use Eq 6.5 to obtain the energy balance

$$\frac{\alpha f^2}{2E\ell_c} - \frac{\alpha \Delta L f^2}{E\ell_c(\ell_c + \Delta L)} + b_p \cos\theta f > \frac{\alpha f^2}{2E(\ell_c + \Delta L)} + C_\theta b_p \cos\theta f + 4W\ell_c + \sqrt{3}\gamma\ell_c^2 \tag{6.8}$$

while for constant displacement we use Eq 6.7 and $\Delta u = 0$ to obtain

$$\begin{aligned}\frac{\alpha f^2}{2E\ell_c} - \frac{\alpha f^2 \Delta L}{E\ell_c(\ell_c + \Delta L)} + b_p \cos\theta f - \frac{\alpha}{2E(\ell_c + \Delta L)}\left[\frac{f\Delta L}{\ell_c} - \frac{b_p E\cos\theta(\ell_c + \Delta L)}{\alpha}\right]^2 \\ > \frac{\alpha f^2}{2E(\ell_c + \Delta L)} + C_\theta b_p \cos\theta f + 4W\ell_c + \sqrt{3}\gamma\ell_c^2\end{aligned} \tag{6.9}$$

Solving for the force at equality and dividing by the contact area ℓ_c^2 yields the corresponding hardness (contact pressure) at nucleation of the next SFHO. For constant force, we use Eq 6.8 to obtain

$$P_c^+ = \frac{Eb_p \cos\theta(1 - C_\theta)(1 + \frac{\Delta L}{\ell_c})}{\alpha \Delta L}\left[1 \pm \sqrt{1 - \frac{2\alpha\Delta L(4W/\ell_c + \sqrt{3}\gamma)}{E(1 + \frac{\Delta L}{\ell_c})[b_p \cos\theta(1 - C_\theta)]^2}}\right] \tag{6.10}$$

while for constant displacement, we use Eq 6.9 to obtain

$$P_c^+ = \left(\frac{Eb_p \cos\theta (1 - \frac{C_\theta}{1+\frac{\Delta L}{\ell_c}})(1 + \frac{\Delta L}{\ell_c})}{\alpha \Delta L} \right) \cdot \left[\pm \sqrt{1 - \left[\frac{2\alpha \Delta L (4W/\ell_c + \sqrt{3}\gamma)}{E(1 + \frac{\Delta L}{\ell_c})^2 [b_p \cos\theta (1 - \frac{C_\theta}{1+\frac{\Delta L}{\ell_c}})]^2} + \frac{\Delta L}{\ell_c (1 - \frac{C_\theta}{1+\frac{\Delta L}{\ell_c}})} \right]} \right] \tag{6.11}$$

Eqs. 6.10 and 6.11 give the pressure necessary for nucleation. The pressure after nucleation is determined for constant force conditions through the change in geometry, $P_c^- = P_c^+ \ell_c^2/(\ell_c + \Delta L)^2$ and for constant displacement conditions the changes in force and geometry, $P_c^- = (P_c^+ \ell_c^2 + \Delta f)/(\ell_c + \Delta L)^2$.

There are two differences in the critical pressure between the two loading conditions, both related to $\ell_c \sim \Delta L$. The first difference is between C_θ and $C_\theta/(1+\Delta L/\ell_c)$ which becomes negligible for large edge lengths. The second difference is an extra term in the constant displacement solution inside of the square root proportional to $\ell_c \sim \Delta L$. Since this term has a similarly $1/\ell_c$ scaling to the other term in the square root, it leads to a constant shift in the prediction of the hardness, relative to the constant force case, at large ℓ_c. The consequence of these extra terms at small edge lengths will be discussed in more detail below.

There are a few critical observations regarding the pressures in Eqs. 6.10 and 6.11 since there is a square root in the results. The combinations of physical quantities assigned to many of the constants in Eqs. 6.10 and 6.11 makes it possible to end up with imaginary solutions under specific conditions. Figure 6.2 shows the pressure for a unity edge length normalized by the leading coefficients of Eq. 6.10 versus the normalized energy associated with the SFHOs for $C_\theta \neq 0$. This figure shows that Eq. 6.10 establishes an upper and lower limit to the pressure as well as a maximum SFHO energy which can be accommodated for any given edge length. The upper

and lower limits are defined by choosing the positive and negative values of Eq. 6.10 respectively. If the energy associated with the SFHO is zero, i.e. $4W/\ell_c + \sqrt{3}\gamma = 0$, then two solutions exist to the function: first, the trivial solution of $P = 0$ and secondly, the solution of $P = 2Eb_p \cos\theta(1 - C_\theta)(1 + \Delta L/\ell_c)/\alpha\Delta L$.

The two results are the upper and lower limits and any values of pressure between these limits will provide enough energy for the discrete deformation to take place. The lower limit is straightforward to understand, with out a minimal amount of energy no work can be done. The upper limit on the other hand is a little less intuitive, since the total change in elastic energy has a quadratic dependence on the pressure (force) and is negative, eventually with increasing force accommodating the elasticity requires more energy than will be available once the energy just to move the dislocations is accounted for, establishing the upper limit. Again examining Figure 6.2 by increasing the energy, or introducing the energies associated with the SFHO, the two solutions for the force approach each other and eventually reach a point at which they meet. This meeting point establishes a limit for a ratio of the available energies. The energy ratio must be ≤ 1 leading to

$$4W/\ell_c + \sqrt{3}\gamma < \frac{Eb_p[\cos\theta(1 - C_\theta)]^2}{2\alpha\Delta L} \tag{6.12}$$

Which again is again saying that the energy stored by the SFHO and its fields must be less than or equal to the available elastic energy. The same can be done for constant displacement considerations where the maximum energy is defined by

$$4W/\ell_c + \sqrt{3}\gamma < \frac{Eb_p[\cos\theta(1 - C_\theta)]^2}{2\alpha\Delta L}\left(1 - \frac{\Delta L}{\ell_c(1 - C_\theta/(1 + \Delta/\ell_c))}\right) \tag{6.13}$$

The constant displacement is missing energy from external work that can offset some of the change in elastic energy so this condition is generally more stringent than that

of Eq. 6.12. When the energy of the dislocation structure is added, the conditions under which the energy balance can be satisfied are yet more stringent.

We now examine the scaling of the pressure for $\ell_c >> \Delta L$. For constant force, the highest order term ℓ_c is that associated with the stacking fault energy. However, the magnitude of this energy is much smaller than that of the other terms out to large ℓ_c corresponding to the range of experiments. Hence, it can be neglected for practical purposes. This is consistent with our MD results for a Au potential with a much higher stacking fault energy that shows nearly identical response to the low-stacking fault simulations. The scaling of the pressure is thus controlled by the dislocation interaction energy plus ledge energy term $4W/\ell_c$. For large ℓ_c, we can then expand the square-root term in the critical pressure to lowest order and obtain an estimate of the scaling. For the constant force case (the constant displacement case is similar), we obtain

$$P_c^+ = \frac{4W/\ell_c}{b_p \cos\theta(1 - C_\theta)} \tag{6.14}$$

In this result, the structural compliance α does not appear, so that the elasticity changes are negligible in this limit. The energy input is controlled by the external work, which is consumed in creating and moving the new SFHO. If W is independent of ℓ_c then the model predicts a scaling of $1/\ell_c$, which is much faster than observed in the MD or experiments. However, as we will see below, the dislocation interaction energies scale with a sum over ln(length) and can contribute non-negligibly at moderate edge lengths, 10 nm $< \ell_c <$ 100 nm. Furthermore, the expansion of the square root to lowest order is not sufficiently accurate in this size range, and corrections further decrease the scaling with ℓ_c.

With the general results of the energy model now established, and broad trends and limits identified, we now turn to evaluation of the specific energy contributions

in the model to make predictions for comparison against the simulations and experiments.

6.1.2 Dislocation Energies

Eqs. 6.10 and 6.11 show that the hardness (pressure) is a unique function of the current contact length, the dislocation energetics (γ, W), elastic modulus (E), and geometry $(\alpha, \Delta L)$. To make quantitative predictions for the pressure, each of these quantities must be evaluated. We start here with the dislocation interaction energies, which dominate the scaling in the large edge length limit.

The self energy of the dislocation is approximated from elasticity as Hirth and Lothe (1968)

$$w_{self} \approx \mu b^2/4\pi(1-\nu) \tag{6.15}$$

The energies $w_{sfho},\ w_{||}$, and w_{im}, are functions of the length of the dislocations. The interaction energy between any two coplanar dislocations is given by Hirth and Lothe (1968)

$$\begin{aligned} W_{12} = \frac{\mu}{4\pi}\{&(b_1\cdot\xi_1)(b_2\cdot\xi_2) - 2[(b_1\times b_2)\cdot(\xi_1\times\xi_2)] \\ &+ \frac{1}{1-\nu}[b_1\cdot(\xi_1\times e_3)][b_2\cdot(\xi_2\times e_3)]\}I(x_\alpha, y_\beta) \\ &+ \frac{\mu}{4\pi(1-\nu)}[(b_1\cdot e_3)(b_2\cdot e_3)]\{R(x_\alpha, y_\beta) \\ &- \cos\theta[x_\alpha \ln t(x_\alpha, y_\beta) + y_\beta \ln s(x_\alpha, y_\beta)]\} \end{aligned} \tag{6.16}$$

The Burgers vectors b and line senses ξ for the SFHOs in the present problem are defined as shown in Figure 6.3. The remaining functions are integrals are given by

$$I(x,y) = x\ln\frac{R+y-xcos\theta}{x} + y\ln\frac{R+x-ycos\theta}{y} \tag{6.17}$$

$$R^2(x,y) = x^2 + y^2 - 2xycos(\theta) \tag{6.18}$$

$$t = xcos\theta - y + R \tag{6.19}$$

$$s = ycos\theta - x + R \tag{6.20}$$

The summations of $\alpha, \beta = 1, 2$ are of the form

$$I(x_\alpha, y_\beta) = I(x_1, y_1) - I(x_1, y_2) - I(x_2, y_1) + I(x_2, y_2) \tag{6.21}$$

The interaction energy w_{sfho} among the four (100) dislocations making up one SFHO reduces to an interaction between one dislocation ($b_1 = a/3[100]$; $\xi_1 = 1/\sqrt{2}[011]$) with its two adjacent dislocations at $\theta = 60^o$ ($b_2 = a/3[0\bar{1}0]$; $\xi_2 = 1/\sqrt{2}[101]$) and with its one opposite dislocation at $\theta = 90^o$ ($b_2 = a/3[\bar{1}00]$; $\xi_2 = 1/\sqrt{2}[0\bar{1}1]$). At the intersection of the four dislocations (the SFHO apex) there is a singularity that is not realistic at the atomic level, and so a small length of each dislocation is excluded from the interaction calculation and accounted for below by an additional junction energy parameter. Figure 6.4 shows the computed interaction energy per unit length of dislocation for various excluded lengths ranging from $b/4$ to $2b$, and is scales approximately as $w_{sfho} \propto ln(\Delta L/\ell_c)$. The interaction energy $w_{||}$ for a new SFHO dislocation interacting with the parallel dislocations of the preexisting SFHOs follows the same general formula, but is simplified due to the parallel geometry and the equal burgers vectors and line senses (Figure 6.5). The interaction between a pair of such parallel dislocations is given by

$$\begin{aligned} W_{||} = (&\frac{\mu}{4\pi}(b_1 \cdot \xi_1)(b_2 \cdot \xi_2) + \frac{\mu}{4\pi(1-\nu)}\{(b_1 \cdot e_3)(b_2 \cdot e_3) \\ &+ [(b_1 \times \xi_1) \cdot e_3][e_3 \cdot (b_2 \times \xi_2)]\})I(x_\alpha, y_\beta) \\ &+ \frac{\mu}{4\pi(1-\nu)}(b_1 \cdot e_3)(b_2 \cdot e_3)R(x_\alpha, y_\beta) \end{aligned} \tag{6.22}$$

with

$$I(x,y) = R - \frac{1}{2}(y-x)\ln s + \frac{1}{2}(x-y)\ln t \tag{6.23}$$

$$R(x,y) = \left[(x-y)^2 + \delta^2\right]^{1/2} \tag{6.24}$$

$$t = R + x - y \tag{6.25}$$

$$s = R + y - x \tag{6.26}$$

where δ is the normal distance between the pair of dislocations. The interaction is then simplified further since $b_1 \cdot \xi_1 = b_2 \cdot \xi_2 = 0$, $(b_1 \times \xi_1) \cdot e_3 = e_3 \cdot (b_2 \times \xi_2) = 0$, and $b_1 \cdot e_3 = b_2 \cdot e_3 = a/3$.

For a generic newly nucleated SFHO the parallel dislocations have lengths of $x_1 = 0$, $x_2 = \ell_c$, $y_1 = \delta$, and $y_2 = \ell_c - \delta$. With $b = a/3$, a single parallel interaction per unit length of new dislocation is

$$w_{||} = \frac{\mu b^2}{4\pi(1-\nu)\ell_c}\left[I(x_\alpha, y_\beta) + R(x_\alpha, y_\beta)\right] \tag{6.27}$$

Substituting in ℓ_c and δ results in:

$$\begin{aligned} w_{||}\frac{4\pi(1-\nu)\ell_c}{\mu b^2} &= 4\sqrt{2}\frac{\delta}{\ell_c} - 4\sqrt{1 - 2\frac{\delta}{\ell_c} + 4\left(\frac{\delta}{\ell_c}\right)^2} \\ &+ \frac{\delta}{\ell_c}\ln\left[\frac{(\sqrt{2}-1)\left(\sqrt{1 - 2\frac{\delta}{\ell_c} + 2\left(\frac{\delta}{\ell_c}\right)^2} + \frac{\delta}{\ell_c} - 1\right)}{(\sqrt{2}+1)\left(\sqrt{1 - 2\frac{\delta}{\ell_c} + 2\left(\frac{\delta}{\ell_c}\right)^2} - \frac{\delta}{\ell_c} + 1\right)}\right] \\ &+ \frac{1}{2}\ln\left[\frac{\sqrt{1 - 2\frac{\delta}{\ell_c} + 2\left(\frac{\delta}{\ell_c}\right)^2} - \frac{\delta}{\ell_c} + 1}{\sqrt{1 - 2\frac{\delta}{\ell_c} + 2\left(\frac{\delta}{\ell_c}\right)^2} + \frac{\delta}{\ell_c} - 1}\right] \end{aligned} \tag{6.28}$$

As the edge length becomes large relative to the spacing $\delta/\ell_c << 1$, a power series

expansion yields the asymptotic result

$$w_{||} = \frac{\mu b^2}{4\pi(1-\nu)} \left[2 \ln \left(\frac{2\ell_c}{\delta} \right) - 4 \right] \tag{6.29}$$

which is in excellent agreement with the full expression of Eq (6.22). Figure 6.6 shows the comparison of Eq 6.29 with the exact solution for a newly nucleated SFHO with the nearest previously nucleated SFHO as the edge length, ℓ_c of the new SFHO increases. The fluctuations are associated with the changes in $2\delta = \Delta L = 0.86,\ 1.44$ nm for the (114) pyramid facet. Again the figure shows how well the approximate solution compares to the full solution from Eq 6.28. The total interaction of a new SFHO dislocation with N previous parallel dislocations is obtained by summing the energy due to each interaction with a spacing for the ith interaction,δ, equal to the sum of the j previous incremental increases in the dislocation spacing, $\Delta L_j/2$, between the new SFHO and the ith, $\delta = \sum_{j=1}^{i} \Delta L_j/2$, resulting in a total interaction energy of:

$$w_{||} = \frac{\mu b^2}{4\pi(1-\nu)} \sum_{i=1}^{N} \left[2 \ln \left(\frac{4\ell_c}{\sum_{j=0}^{i} \Delta L_j} \right) - 4 \right] \tag{6.30}$$

The actual result of changing N will be discussed later. The energy associated with image forces is calculated as the interaction of a dislocation with its image dislocation across the (assumed flat) pyramid surface, and employs the same general interaction expressions used to determine w_{sfho}. In this case, a dislocation with $b_1 = a/6[020]$, $\xi_1 = 1/\sqrt{2}[\bar{1}0\bar{1}]$ interacts with the image dislocation having $b_2 = a/6[020]$, $\xi_2 = 1/\sqrt{2}[\bar{1}01]$ and $\theta = 90^o$. The resulting energy per unit length is $w_{im} = \mu b^2(\sqrt{2} - 2)/4\pi(1-\nu) = (\sqrt{2}-2)w_{self}$.

All of the interaction energies consist of the dislocation core energy, defined in Eq 6.15, multiplied by either a constant or a term depending on the geometry $(\Delta L, \ell_c, \delta)$. A comparison of all the energies versus edge length is shown in Figure 6.8, where $w_{||}$ is the energy between the nearest previously nucleated SFHO. Even for the single near-neighbor interaction, $w_{||}$ is the largest energy term and increases with increasing edge length. With the inclusion of additional dislocations beyond near-neighbor as in Eq 6.30, $w_{||}$ is clearly the dominant energy in the nucleation process and has the strongest dependence on edge length.

6.1.3 Ledge Energy

To calculate the ledge energy per unit length E_L a simple periodic MD simulation is run with two parallel free (001) surfaces each containing a ledge. For this system the total energy is $E_T = E_{COH}N + \gamma_{001}A + E_L\ell_e$ where E_{COH} the cohesive energy per atom, N is the number of atoms, $\gamma_{(001)}$ is the (001) surface energy per unit area, A is the total surface area of both free surfaces, and ℓ_e is the total length of both ledges. For this potential, the cohesive energy is $E_{COH} = -3.93$ eV/atom but the (001) surface energy is not known. A supplementary simulation was performed to calculate the surface energy using the same geometry as above but without the ledges so that the total system energy is $E_T = E_{COH}N + \gamma_{(001)}A$. The total energy is determined by running the simulation using NPT dynamics at 1 K and zero lateral pressure and the resulting surface energy is $\gamma_{(001)} = 5.79$ eV/nm^2, exactly the value reported in the literature by Foiles *et al.* (1984). Computation of E_T for the first system with the two ledges then leads to a ledge energy per unit length of $E_L = 0.32$ eV/nm. This energy is fairly small compared to the dislocation interaction energies, except at the very smallest length scales.

6.1.4 Determination of α

We use elasticity theory to compute the value of the pyramid structural compliance parameter α. We assume the pyramid to be a homogeneous, anisotropic, linearly elastic material and use a finite element model (FEM) to compute the response under an applied compressive load. The elastic constants of the Auu3 EAM potential are C_{11} = 183 GPa, C_{12} = 153 GPa and $C44$ = 45 GPa. The dimensions for the simulation are exactly the same as those of the largest MD simulation having $\ell_c = 8.6$ nm. Symmetry permits for the reduction of the sample to a 1/4 model with the following boundary conditions: fixed normal displacement of the (100) and (010) and free opposite $(\bar{1}00)$ and $(0\bar{1}0)$ surfaces. The use of free surfaces is not quite the same as the periodic boundary conditions used in the MD simulations but the boundaries are far enough from the loading that the results should not be affected. The bottom surface is also held fixed in the (010) direction as in the MD simulations. The indentation is simulated as a uniform displacement of the top surface.

The FEM calculation provides the elastic strain energy in the pyramid as a function of the applied force. To compute α, we thus equate the strain energy obtained from the FEM model to the definition of the strain energy in Eq 6.2 and use the FEM-computed force. This yields $\alpha = 0.35$ for the (114) pyramid. The elastic response is independent of initial contact length and boundary locations due to the local strain field and the self-similarity of the pyramid. The computed value of α is thus relevant for any (114) pyramid. However, there are some differences between the MD and the FEM that cannot be accounted for: (i) the non-linearity in the atomic potentials at high loads, (ii) the surface elasticity of the atomistic pyramid surfaces, and (iii) the stepped nature of the facets. The latter two effects are likely small.

To ensure accuracy of the FEM results in the presence of singularities near the

edges of contact, we compare separate FEM results against the known analytic solution for a cylindrical flat punch. The force of cylindrical punch with radius r on an isotropic infinite solid, at a depth of h is $f = 2Ehr/(1-\nu^2)$. The energy stored in the material is found by simply integrating the force with respect to h, yielding

$$U = \int f dh = \frac{Eh^2 r}{(1-\nu^2)} \tag{6.31}$$

Writing the depth as a function of force gives $h = f(1-\nu^2)/2Er$ which can be inserted into Eq 6.31 along with the contact edge length for the circular punch, $\ell_c = 2r$ to give $U = f^2(1-\nu^2)/2E\ell_c$. Before the analytic energy expression can be compared to Eq 6.2 the force of Eq 6.2 is divided by the appropriate contact area for a cylindrical punch, $\pi\ell_c^2/4$, rather than the contact area for a square punch, ℓ_c^2. Making the necessary area adjustment leads to $U = P^2\alpha\ell_c^3/2E = 8f^2\alpha/\pi^2\ell_c E$. Setting these two results equal yields $\alpha = (1-\nu^2)\pi^2/16 = 0.478$. An FEM simulation of the same problem gives the same value to within numerical accuracy. Using elastic constants for the Au2 EAM potential, we expect $\alpha = 0.481$ and again the FEM predicts the correct value. These values of α are much higher than the (114) pyramid due to geometry and isotropy. We used the FEM simulations to compute α for a square punch on a flat surface and for indentation of a (118) pyramid. Using the Auu2 elastic constants for a flat punch having the same contact area as the (114) pyramid results in an α almost exactly the same as that for (114) pyramid. Similarly, indentation of the (118) pyramid yields nearly the same value of α, with very minor differences that are within the range of values seen by simply changing the resolution of the mesh at the corners of the indentation. Figures 6.9a-c show the normal stress distribution along one of the simulations symmetric faces. In all cases, most of the stress is concentrated just below the indenter and off at a 45^o angle from the edge of the contact. Since the stress field does not change the α value will not change either.

We attempted to use the MD results directly to determine α but this is not sufficiently accurate. We compute the total change in the atomistic energy between each nucleation event should be equal to the stored elastic energy as previously predicted if the deformation is linear elastic (no dislocation motion). Figure 6.7 shows the alpha values for two atomistic simulations with 1.7 and 4.6 nm initial contact edge lengths. There are large fluctuations in the initial stages of the data most likely associated with non-linear elasticity and fluctuations associated with the barostat. After the nucleation of dislocations, the estimated α values stabilize between $0 \sim 1$ but with large fluctuations. These results suggest that at small edge lengths the linear elastic approximation may not be sufficiently accurate for predicting the hyperelastic energy stored in the system.

6.1.5 Model Predictions versus MD and Experiments

To make quantitative predictions using the energy model requires values for several other parameters appearing in Eqs. 6.10 and 6.11. From the (001) atomic layer spacing and the slope of the (114) facets, geometry dictates that ΔL alternates between 0.86 and 1.44 nm. We use the known stacking fault energy $\gamma = 4.7\text{mJ/m}^2$ from Park and Zimmerman (2005) for this potential. The self energy w_{self} is not known for this EAM potential, and so is estimated from dislocation theory as noted earlier in Eq 6.15 resulting in $w_{self} = 0.77$ eV/nm.

Since $\mu b^2/4\pi(1-\nu)$ is only an approximation for w_{self} and also appears as the coefficient for all of the other dislocation energy terms ($w_{sfho},\ w_{im},\ w_{||}$), we allow for an adjustable parameter C_w to scale the dislocation energies, so that $W = C_w(w_{self} + w_{||} + w_{im} + w_{sfho}) - E_L$. To account for the length of dislocation excluded in the calculation of w_{sfho}, we allow for another adjustable parameter C_{cut} so that $w_{sfho} \propto [\mu b^2/4\pi(1-\nu)](\ln(\Delta L/\ell_c) + C_{cut})$. This approximation is not exact since C_{cut} will

scale with the edge length of the previous nucleation but should give a reasonable representation of the neglected energy. We recall that there is a third parameter $C_\theta < 1$ relating the applied force to the resolved shear stress on the slip plane, which can be estimated from the resolved shear stresses computed in the elastic FEM model. Lastly, the maximum number of dislocations N included in the parallel interaction energy, Eq 6.30, is unspecified. We consider $N = 5, 10$ below, since we do observe multiple SFHOs but also annihilation due to twinning and since we have neglected the other non-parallel dislocation interactions beyond the first SFHO.

From the asymptotic result of Eq 6.29, and neglecting the small ledge and stacking fault energies, we can see that the pressure at large ℓ_c is directly proportional to C_w and with an inverse and weaker dependence on C_θ for C_θ not approaching unity. The parameter C_{cut} adds a constant to the overall energy and thus to the predicted pressure in this regime. So, increasing any of these parameters increases the energy to form the SFHOs and increases the associated pressure. There is thus no unique fit of the several adjustable parameters to the large length data. As noted earlier, however, the size-scaling in this regime is controlled by the overall ℓ_c^{-1} modified by the logarithmic terms in the dislocation energy Eq 6.30, and is thus unaffected by the precise values of the various adjustable parameters. At smaller values of ℓ_c, the dependence is too complex to ascertain any simple dependencies.

Due to possible imaginary solutions, corresponding to insufficient initial energy and/or external work, the adjustable parameters cannot assume any values at all. C_w, C_{cut}, and/or C_θ must be chosen in order to satisfy Eqs **??**. The MD study shows the creation of SFHOs at small scales and very high loads, so the true energy inequality must be satisfied. Moreover, since we observe $\ell_c^{-1/2}$ scaling for the nucleation of the first SFHO, we expect SFHO formation in this regime to be controlled by an additional energy barrier, not included in our model, such that the total available

energy is above the minimum necessary. Lastly, the elastic FEM study shows the expected stress concentrations near the edge of contact that can drive nucleation of SFHOs over the local energy barrier presented by the material's innate resistance to interplanar slip.

Nonetheless, we fit the constant force model to the MD result for the first SFHO nucleation at the smallest edge length, $\ell_c = 1.7$ nm, expected to be the most challenging regime for the model, and simultaneously fit to the large-length limit in the range of the experimental data. We obtain the results for the pressures before and after each successive SFHO nucleation at small scales in Figures 6.10 and for the larger length scales in Figure 6.11. Figures 6.10a and 6.11a are for $N = 10$, $C_w = 0.7$, $C_\theta = 0.2$, and $C_{cut} = 2$ corresponding to a cut-off of $2b$ for w_{sfho} from Figure 6.4 while Figures 6.10b and 6.11b are for $N = 5$, $C_w = 1.0$, $C_\theta = 0.2$, and $C_{cut} = 0.09$ with w_{sfho} energies again determined with a cut off of $2b$. These parameters are both chosen to fit the data as best as possible without giving imaginary results. Examining Figure 6.10, the results for $N = 5$ are much lower than $N = 10$. This is due to the lower value of C_{cut} which has a larger influence at small edge lengths where the SFHO junction has a more significant contribution to the total energy. For the first nucleation event, in each case, dislocation interactions are absent and so the predicted pressures are too low and exhibit ℓ_c^{-1} scaling rather than the observed $\ell_c^{-1/2}$ scaling. After the first nucleation, the dislocation interactions drive an increase in the pressure to nucleate the next SFHO, a trend qualitatively consistent with the MD results. Subsequent SFHOs are nucleated with the pressure rising, due to interactions, over some range of contact lengths but then falling at larger length scales as the increasing interaction energy per unit length is offset by the overall ℓ_c^{-1} scaling. This behavior is also qualitatively consistent with the MD results. The magnitude of the pressure drops upon SFHO nucleation, and their variation, is also generally captured by the

model at the small scales.

At larger length scales, Figure 6.11, both models predict a convergence of the pressures to a common curve, due to the dominance of the dislocation interaction energies and loss of sensitivity to those SFHOs formed earlier in the indentation. Again the $N = 5$ case has lower magnitudes relative to the experiments and the $N = 10$ predictions even though the model is adjusted to attempt to match both the MD and the experiments. For $N = 5$, the energies are just insufficient to generate the observed pressures over the entire range of size scales. In the regime $\ell_c \sim 10 - 40$ nm, for $N = 10$, the model predicts quite well both the magnitude of the pressure and the $\ell_c^{-(0.3-0.4)}$ scaling found in the MD. This scaling emerges due to a complex competition between various ℓ_c^{-1} and $\ln \ell_c$ dependencies and the changing elastic energy. At larger scales $\ell_c > 40 - 100$ nm, the scaling evolves to power laws of $\ell_c^{-(0.5-0.7)}$ with a magnitude comparable to the experiments (a feature fit, however). As discussed above the model is expected to eventually have a scaling of ℓ_c^{-1} as $\Delta L << \ell_c$ but these results show that even at edge lengths of ~ 500 nm the $\ln \ell_c$ from $w_{||}$ is still large enough to inhibit the scaling from dropping off. Overall, the model predictions indicate a transition from a nucleation-dominated regime for the early SFHOs, here $\ell_c < 10$ nm, to dislocation-interaction-dominated regime at larger sizes.

The constant displacement prediction with fitting parameters of $N = 10$, $C_w = 0.7$, $C_\theta = 0.2$, and $C_{cut} = 0.1$ is shown in Figure 6.11. Due to there being less energy available for the creation of the SFHO, particular at small edge lengths, relative to the constant force assumption it is necessary to decrease the SFHO. Since the combination of C_w and C_θ determines the magnitudes at the experimental length scales in order to decrease the energy necessary for creation the C_{cut} parameter is adjusted. The results as expected are very similar to the constant force predictions but at smaller edge lengths $\ell_c < 40$ nm the predictions are lower than the constant force predictions

due to the extra negative term in Eq 6.11 associated with the relaxing of the system towards the indenter.

We have fit the model to the first nucleation pressure at the smallest size because the energetics are the simplest: before nucleation there are no defects and after nucleation there is a single SFHO. However, this regime is likely dominated by nucleation controlled by excess energy barriers. It is thus important to show that even with much larger initial edge lengths > 40 nm the model can still predict the experimental data. Figure 6.13 shows the predictions for $\ell_{ci} = 60$ nm and $\ell_{ci} = 100$ nm, for $N = 10$. The model predicts a rise in hardness that eventually drops off and achieves a magnitude and scaling matching the experiments. The rise in pressure for the model is steeper than for the experiments, attributed to due roundness of the real pyramids. This further confirms the effectiveness of the model.

While a few assumptions are made here to obtain the good agreement between the energy model and the MD, they are not unreasonable. Since the interaction energies are the most dominant factor in the scaling and over-all behavior, the number of dislocations included in calculations is the assumption requiring the most justification. There is some number of dislocations that interact with the newly nucleated dislocations and affect the length at which the scaling transition occurs. In order for the model to correctly capture the magnitudes of the experiments the minimum number of dislocation is $N = 7$. While using $N = 7$ is capable of predicting the correct experimental magnitudes the highest real solutions predicted are much lower than the MD simulations hardnesses. If fewer dislocations are chosen the constants for C_w, C_θ and C_{cut} necessary to capture the experimental magnitudes will result in imaginary values for the MD length scale. The predictions that capture the MD and experiments the best is for $N = 10$. There is a limit to the number of interactions that can be included. With increasing N the C_w, C_θ and C_{cut} must decrease in order

to capture the magnitudes. Eventually the energies modified by the fitting parameters become much too small to be realistic. Setting a maximum value to N in this fashion suggests that dislocations eventually begin to disappear which is supported by the MD in which it is shown that dislocations annihilate and or spread eventually exiting the system through the surface.

We can also use the model to examine the role of the stacking fault energy. The EAM potential used in the MD predicts a very low stacking fault energy, 4.7 mJ/m^2. To examine the effects of the low stacking fault energy, a second EAM potential with a more realistic stacking fault energy (32 mJ/m^2) Park and Zimmerman (2005) was used in the MD, and pressure versus contact edge length is almost unchanged, indicating insensitivity to the stacking fault energy as seen in Figure 5.11 from Ch. 5. Model predictions for hardness using the new potential are compared with the MD and the experiments in Figure 6.15. Since the new potential may differ in other respects, we adjust the model parameters to fit the MD data and obtain $C_w = 0.5$, $C_\theta = 0.3$, and $C_{cut} = 2.1$ for $N = 10$; these values are rather close to those used for the original potential. Thus, the model confirms that the pressure in the MD range is independent of the stacking fault energy. The pressure is slightly different at the experimental lengths, however. For larger edge lengths, the model predicts a minimum hardness defined by the stacking fault energy. For the first potential, that limit was very small, 0.075 GPa, and hence negligible. For the more-realistic stacking fault energy, that limit is 0.52 GPa, large enough to increase the predicted scaling to $\ell_c^{-0.5}$ in the experimental size range, with magnitudes above those of the experiments. However, stacking faults annihilating and full dislocation formation begin occur at much smaller scales, as seen by the MD, so that the stacking fault energy contribution should be eliminated at larger scales. The analytic model presented above is general and can be applied to other types of deformation as long as the mechanisms are

known for the process. As an example the model is applied to the deformation of the (118) pyramid. If we apply the energy model to the (118) pyramid with the new value for $\Delta L = 2.02$ nm with fitting parameters of $C_w = 1.1$, $C_\theta = 0.2$, and $C_{cut} = 0.7$ for $N = 7$. The hardness values are slightly lower than the (114) predictions due to the larger spacing between parallel dislocations, which reduces the interaction energy and thus the pressure. Without any experimental data to compare the larger edge lengths to it is difficult to tell if these fitting parameters will indeed capture correct magnitudes at $\ell_c > 40$ nm. Even though the magnitudes are not captured as well as the (114) case, the analytic model does predict the scaling of data and sets a lower bound for the hardnesses.

6.2 Nix-Gao Predictions

For larger length scales many modelers have employed the methods of Nix and Gao to explain the size scaling due to strain gradient plasticity and the nucleation of GNDs. For reference we will compare our results to those that would be achieved through the Nix-Gao Model. As described in the Introduction the Nix-Gao model predicts a maximum shear stress through the density of dislocations present in a confined volume using the Taylor relation $\tau = \alpha_{NG}\mu b_p\sqrt{\rho_{ss} + \rho_{GND}}$ where ρ_{ss} and ρ_{GND} are the densities of statistically stored and GND dislocations respectively. Also, $\alpha_{NG} \approx 0.3$ is the Taylor factor, $\mu = 45$ GPa is again the shear modulus and $b_p = 0.17$ nm is the burgers vector for a partial dislocation unlike the energetic model which uses the burgers vectors for the SFHO junctions. For the system studied here of nanoasperities the material is primarily defect free at the onset of loading which requires $\rho_{ss} = 0$ leaving only ρ_{GND} to define all of the plasticity. During the compression of a pyramid, the SFHOs are exactly the GNDs for the analysis, and thus the total length of GNDs versus initial edge length and depth of compression can be computed analytically.

These SFHO GNDs define a length scale for the system and influence the stresses necessary to emit new GNDs and/or to expand/nucleate statistical dislocations.

Proceeding quantitatively, geometry requires the total length of the GND in an SFHO nucleated at contact edge length ℓ_c to be $4\ell_c$ and the volume of the SFHO to be $V_{sfho} = \ell_c^3/3\sqrt{2}$. SFHOs are described relative to an initial contact length of ℓ_{ci}, such that the n^{th} SFHO occurs at a compression depth of $\Delta u = na/2$, where $a/2$ is the (100) interplanar spacing, and adds an additional GND length of $4[\ell_{ci} + \Delta L(n-1)]$. For a realistic (114) ΔL will alternate between 0.86 nm and 1.44 nm as described in the previous section. Here an average of the two will be taken to simplify the model. In the previous model where dislocation spacing is required to determine interaction energies the differences in ΔL are more critical. While some detail is left out be averaging ΔL the overall scaling behavior will not be affected. Here it is important to only capture the approximate length of dislocations present in a given volume since the volume is approximated as well. So returning to the definition of ΔL relative to the slope requires $\Delta L = 2\Delta u/m$ nm for a (114) pyramid. Assuming that no twinning or annihilation exists the number of SFHOs created up to the current edge length ℓ_c is then $n = (\ell_c - \ell_{ci})/\Delta L$. These GNDs exert stresses on some volume of material surrounding this last SFHO, i.e. $V = \beta V_{sfho}$ where β is a geometric parameter as determined below. The GND density at the current contact edge length ℓ_c is thus a sum of GND line lengths from all the SFHOs formed starting from ℓ_{ci} up to the current length ℓ_c, divided by the appropriate volume, and is given by

$$\rho_{GND}(l_c) = \frac{3\sqrt{2}}{\beta \ell_c^3} \sum_{i=1}^{n} 4[\ell_{ci} + \Delta L(i-1)] = \frac{6\sqrt{2}}{\beta \ell_c \Delta L} \left[1 - \frac{\Delta L}{\ell_c} + \frac{\ell_{ci}(\Delta L - \ell_{ci})}{\ell_c^2}\right] \quad (6.32)$$

Now proceeding under the assumption of $\rho_{ss} \sim 0$, using Eq 6.32 in the Taylor formula, we obtain a resolved shear stress τ as a function of the initial and current contact edge lengths and the volume factor β, $\tau = \tau(\ell_c, \ell_{ci}, \beta)$. This resolved shear stress is

related to the contact pressure through some ratio $C_\theta = \tau/P$, leading to a predicted pressure of

$$P = \frac{1}{C_\theta\sqrt{\beta}}\alpha_{NG}\mu b_p\sqrt{\beta\rho_{GND}} \tag{6.33}$$

where $\sqrt{\beta}$ has been factored out. To obtain C_θ, we refer to Figure 5.10a which shows the resolved shear stresses resulting from an applied contact pressure with no SFHOs Since this field is self-similar with respect to contact edge length, we obtain C_θ by relating the average shear stress over the effective volume $V = \beta V_{sfho}$ to the current contact pressure. The volume, V, is selected such that it contains the atoms with relatively high shear stresses near the area of contact. Thus, C_θ depends on β; with larger β yielding smaller C_θ; the interplay between these two parameters partially cancel each other in Eq 6.33, minimizing the effect of any specific choice for β. Selecting $\beta = 2$ results in the typical volume within which other SFHOs and statistical dislocations exist, we obtain the ratio $C_\theta = 0.2$. The definition of C_θ here is nearly the same as the definition in the development of the energetic model. It is important to note that these numbers are highly dependent on specific geometry chosen to determine β as well as several other factors including the value of α_{NG} chosen. It is not clear exactly whether the maximum resolved shear stress, the average shear stress or some combination of these shear stresses for the active slip system, should be used to calculate C_θ, which will also determine what α_{NG} to use in the calculations. Using a range of well-justified choices for α_{NG} and β result in variations of the prediction of about a factor of two; the general agreement between the model and the MD/Experiments thus remains largely intact although precise numbers may vary.

The predictions of Eq 6.33 for the three different initial contact edge lengths simulated in the MD, (1.4 nm, 4.6 nm, 8.6 nm) are shown in Figure 6.16 along with the MD and experimental data. The theory, with one slightly adjustable parameter,

qualitatively predicts the hardening behavior at the very onset of deformation and the subsequent softening behavior for larger contact lengths excluding the first nucleation. Since the model requires a dislocation density in order to predict the maximum resolved shear stress the first stress cannot be determined without some sort of nucleation criterion similar to the PN and RT models. The analysis also accurately captures the convergence of the pressures for larger depths of indentation showing the dependence on current contact length only, with an ideal power law scaling of $H \approx \ell_c^{-0.5}$ for $\ell_c >> \ell_{ci}$. This predicted scaling is again between the scaling found in the MD and the experiments. Furthermore, the model provides remarkable quantitative agreement in magnitude with the MD and experimental results, aside from the differences in power-law scaling. It is very surprising that the Nix-Gao model predicts the behavior of the MD so well especially at small edge lengths. Care needs to be taken when interpreting results of the Nix-Gao model at length scales < 100 nm since the interaction energies for this model are assumed under the Taylor relation to have a fairly large distance between them relative to the lengths scales being discussed here. As shown earlier dislocations that are very close to each other will eventually result in a $1/r$ singularity that is not captured through these general interaction energies. It may just be coincidence that for this geometry the other important energetic considerations, the ledge energy and image forces, reduce the large energy from the close proximity interactions to values that are predicted by the Nix-Gao model. However, it is not surprising that the scaling for edge lengths approaching the experimental sizes is well captured. As shown for the energetics, the interaction energies eventually dominate the expression which ultimately results in $\ell_c^{-0.5}$ scaling. Another aspect of the model to consider is the fact that twinning and healing do not exist. If these were to occur then the density of dislocations would decrease as the effective volume increases resulting in further softening. Softening could also occur if full dislocation

emission is considered rather than partial as the total length of dislocation nucleated would decrease faster than the increase in burgers vector.

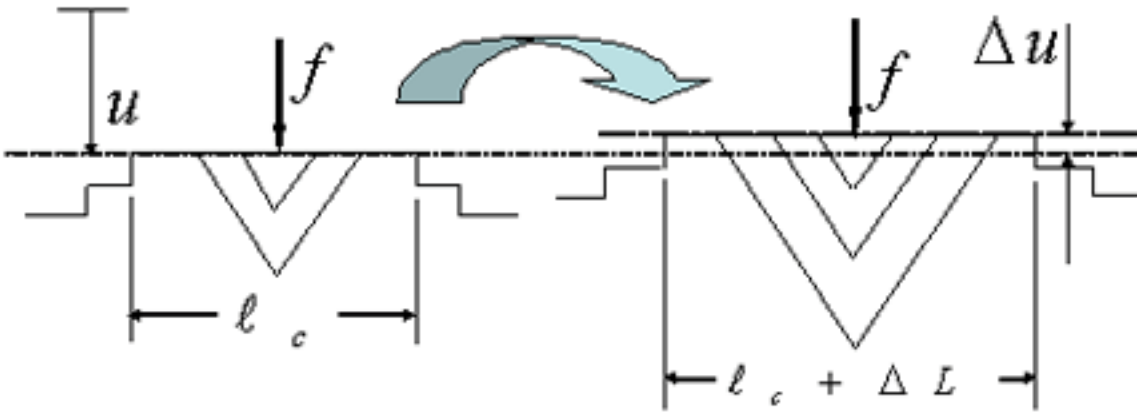

Figure 6.1: Schematic showing the deformation and dislocation structure assumed for the energetic model before and after SFHO nucleation.

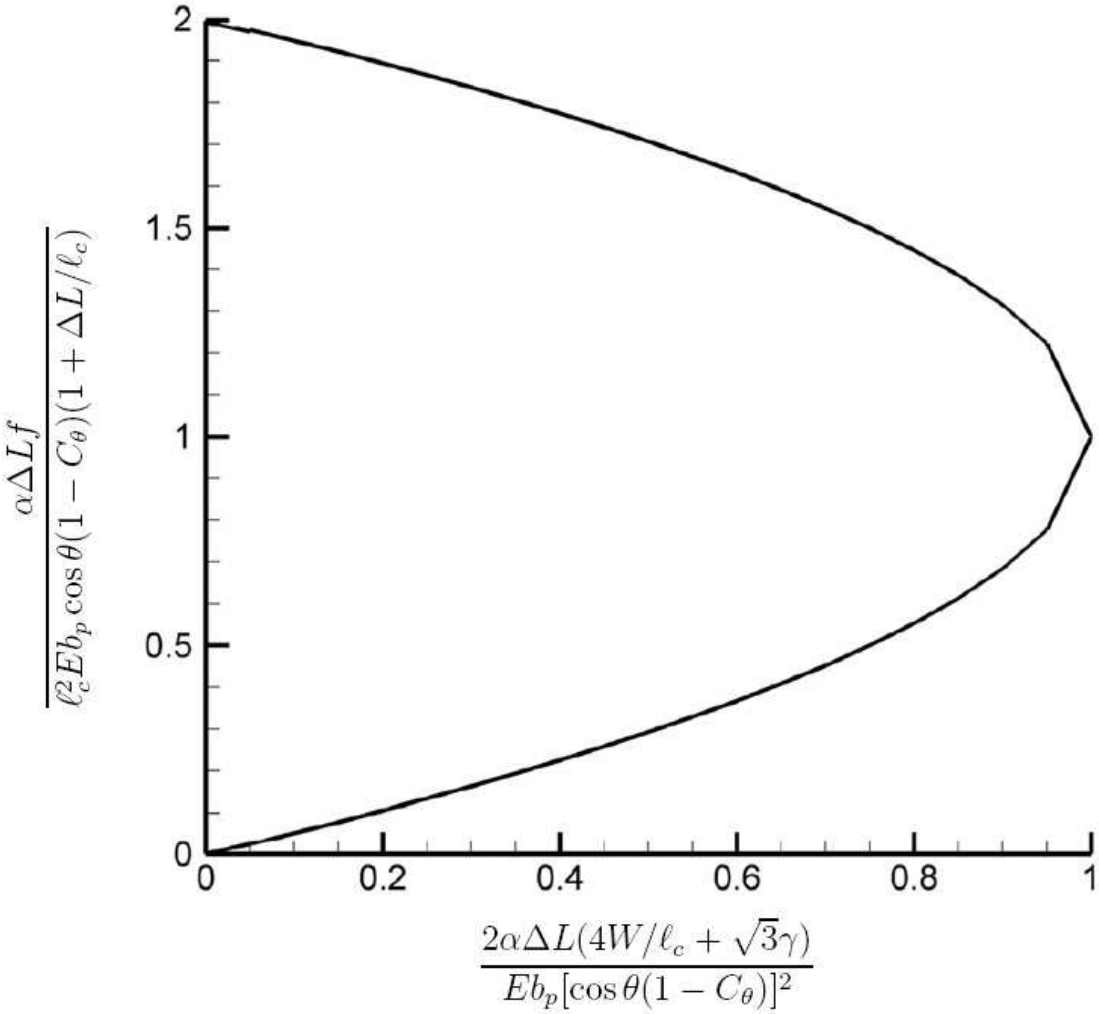

Figure 6.2: Graph showing the possible normalized forces possible by increasing the normalized energy necessary for an SFHO, for a given edge length

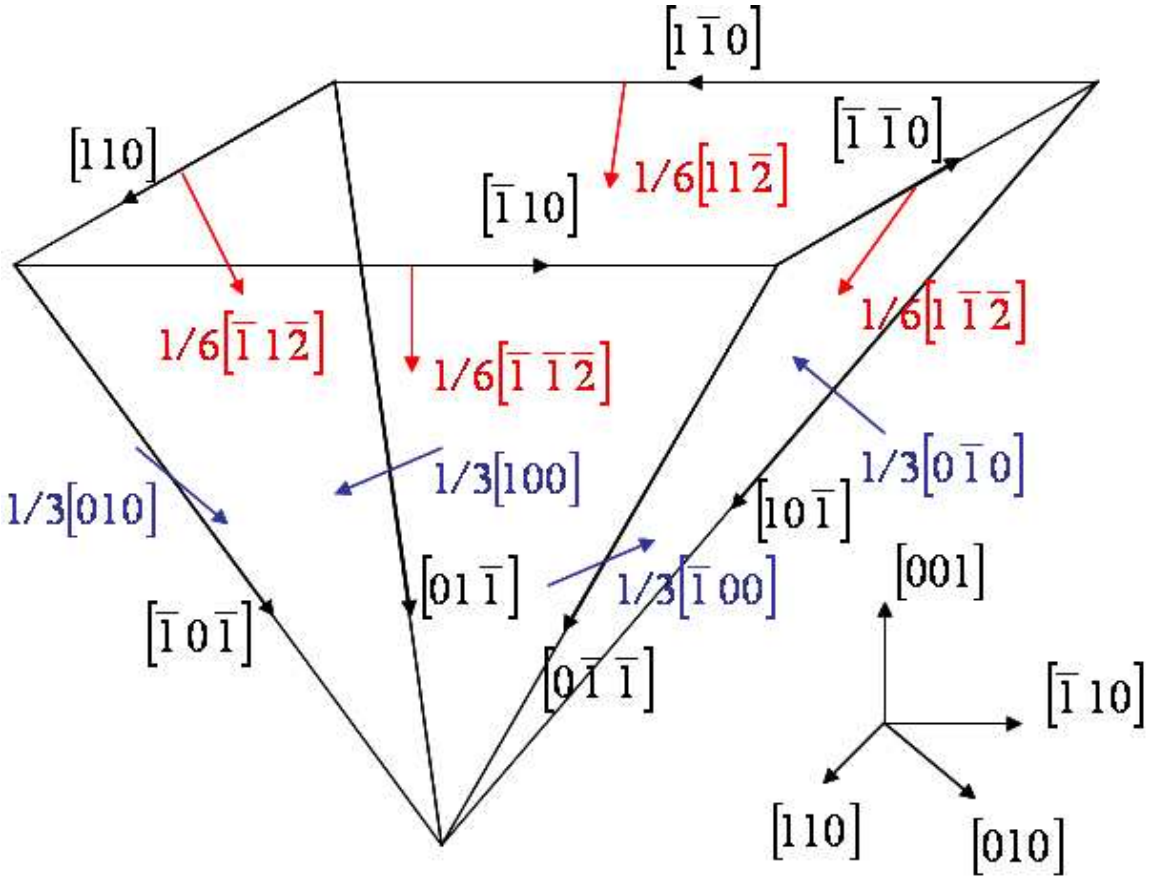

Figure 6.3: Schematic of the stacking fault half octahedron burgers vectors and line senses, line sense (black arrows) and burgers vectors for the initial partial dislocations (red arrows), and (001) junctions formed (blue arrows).

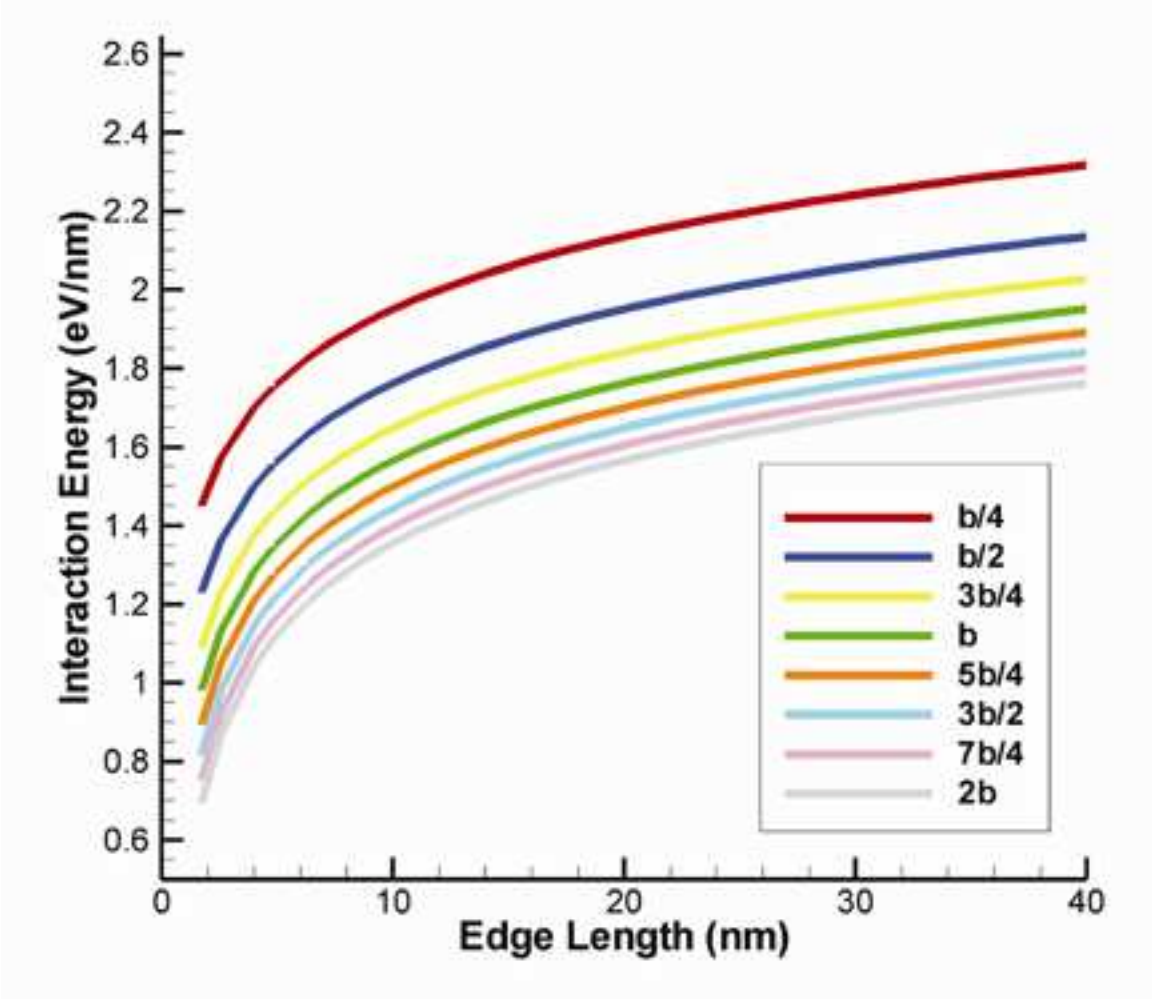

Figure 6.4: The interaction energies vs. edge length for a single dislocation in the SFHO experiences due to the other three dislocations as a function of dislocation length. Each line represents the energy for a different length of dislocation removed at the tip of the SFHO to remove the analytic singularity form the interaction energy.

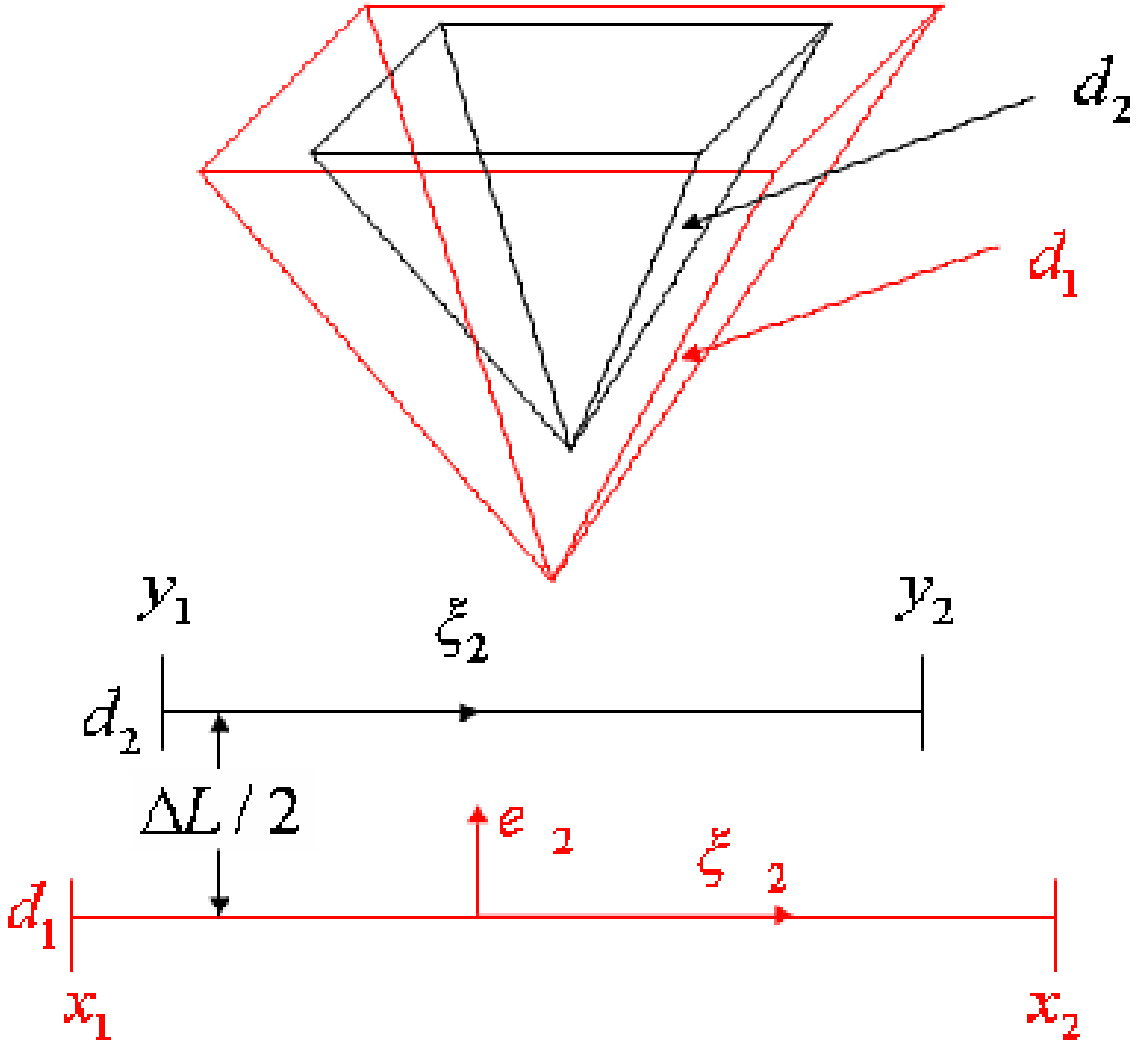

Figure 6.5: Schematic for the interaction energy of two parallel dislocations for subsequent SFHOs.

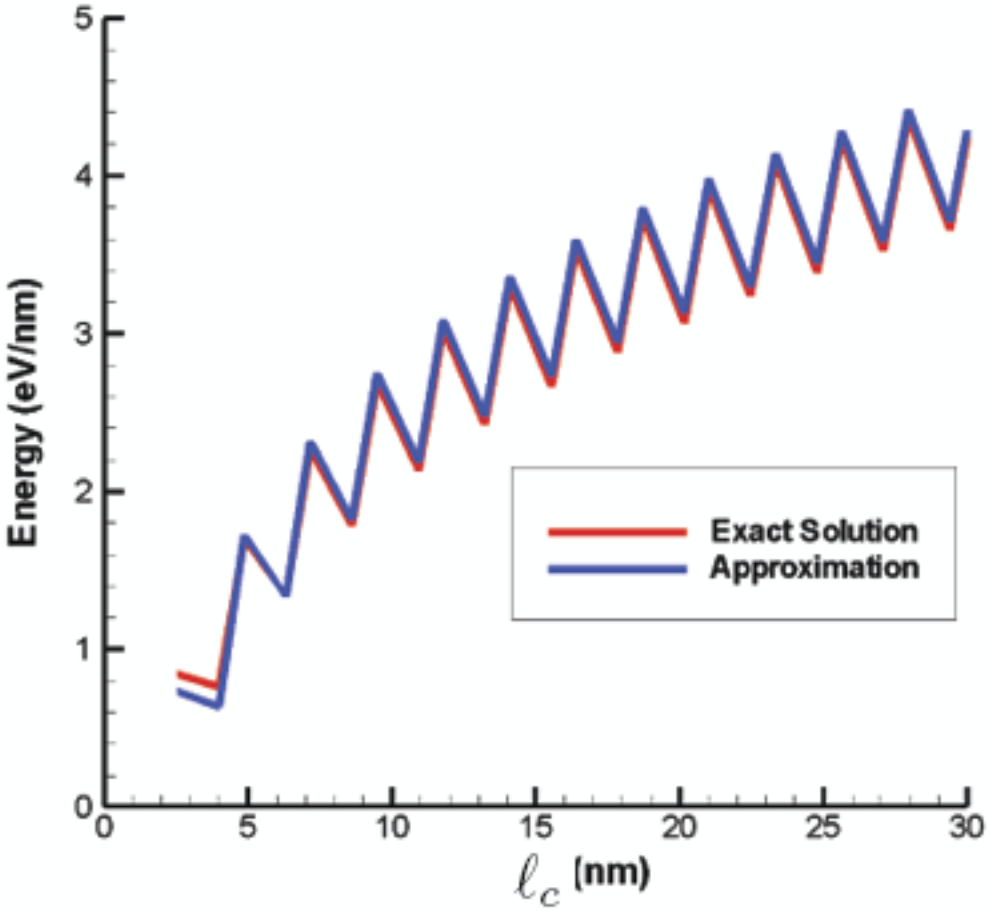

Figure 6.6: Interaction energy, $w_{||}$, for only the first interaction, $N = 1$ for increasing edge lengths, ℓ_c. The distance between the newly nucleated SFHO and the nearest previous SFHO alternates between $2\delta = \Delta L = 0.86$ and 1.44 nm as defined by the (114) facet . The red line is the exact solution while the blue line represents the approximation from Eq 6.29.

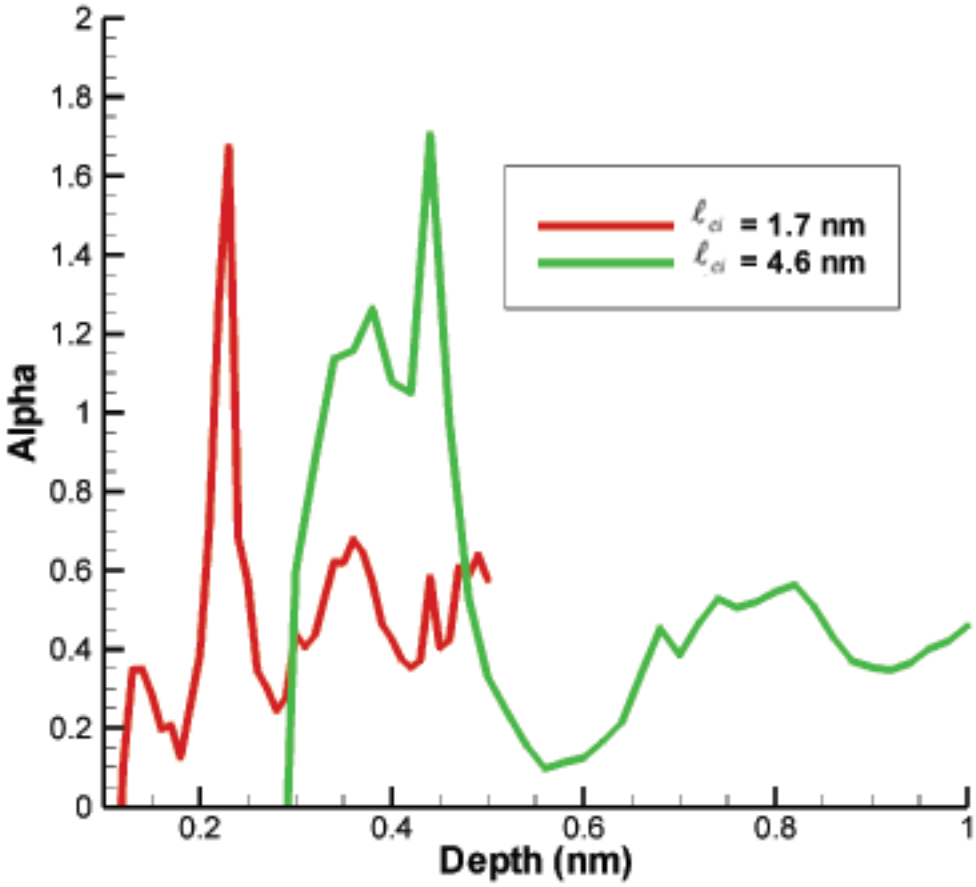

Figure 6.7: Results of α from two of the molecular dynamics simulations with $\ell_{ci} = 1.7$ nm and $\ell)_{ci} = 4.6$ nm as a function of indenter depth.

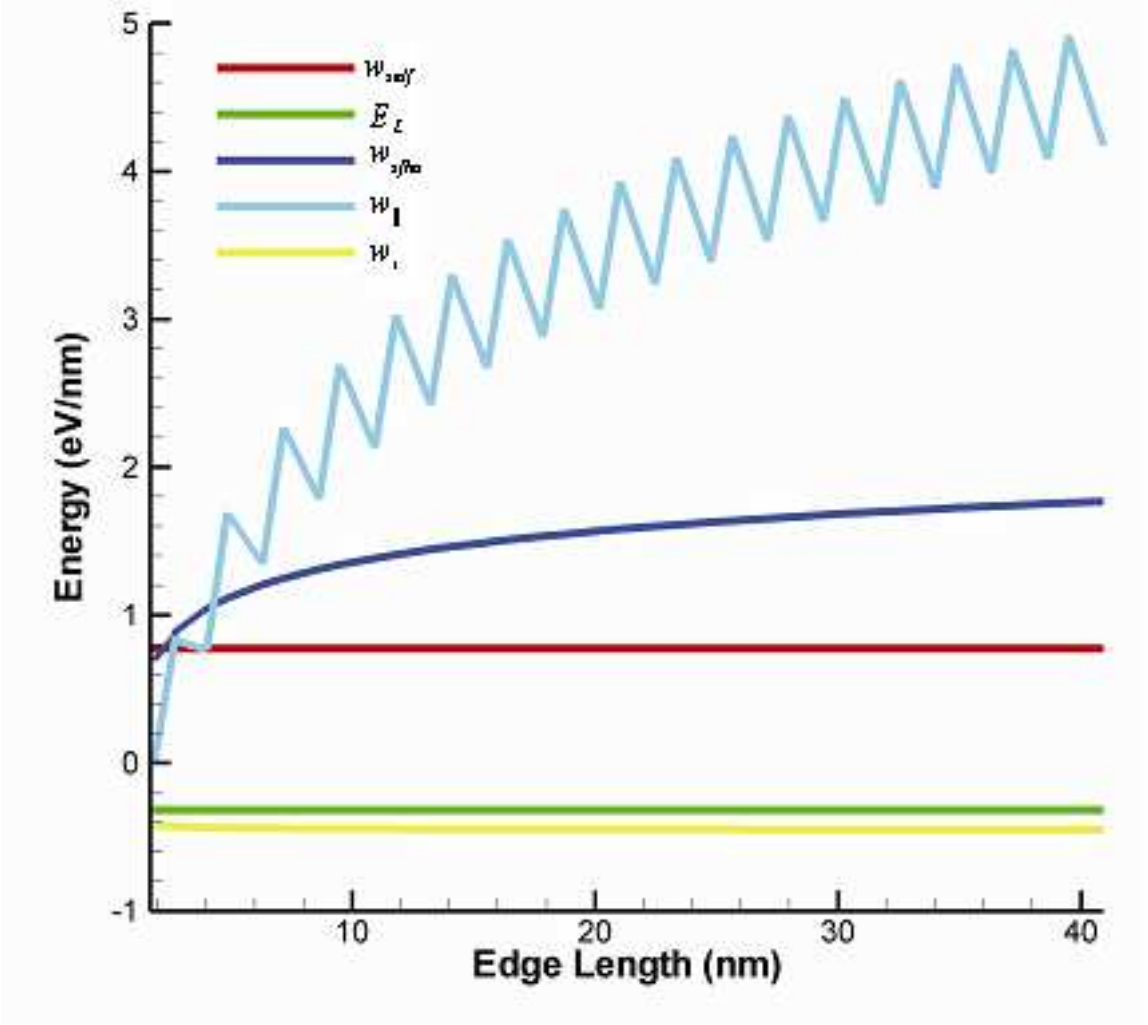

Figure 6.8: Graph of energies vs. edge length for the different interaction and self energies that contribute to making up the total energy attributed to the formation of the dislocations of a new SFHO

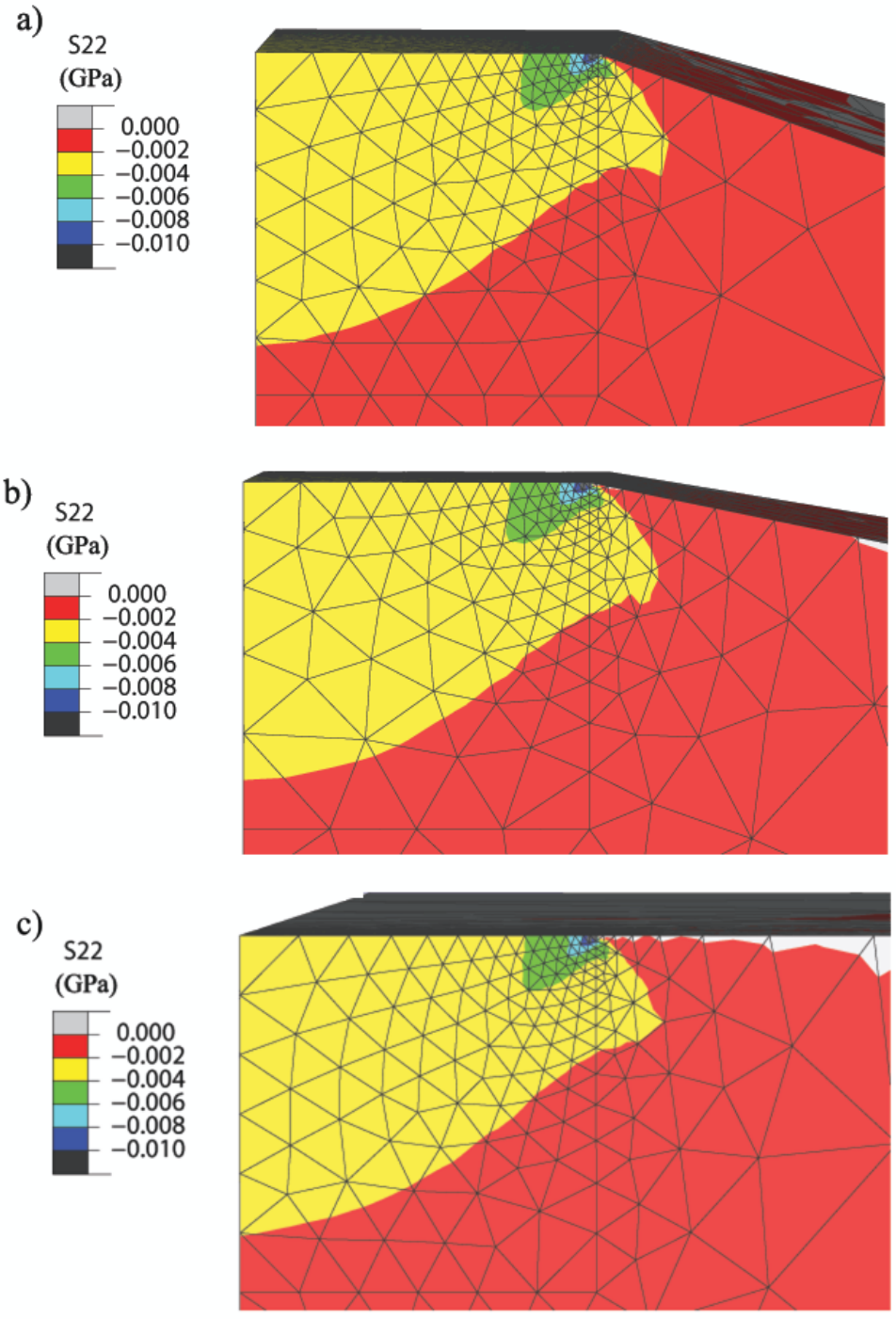

Figure 6.9: Stress distribution in the loading direction (S22) for three FEM simulations; a. (114) pyramid; b. (118) pyramid; c. Flat square punch.

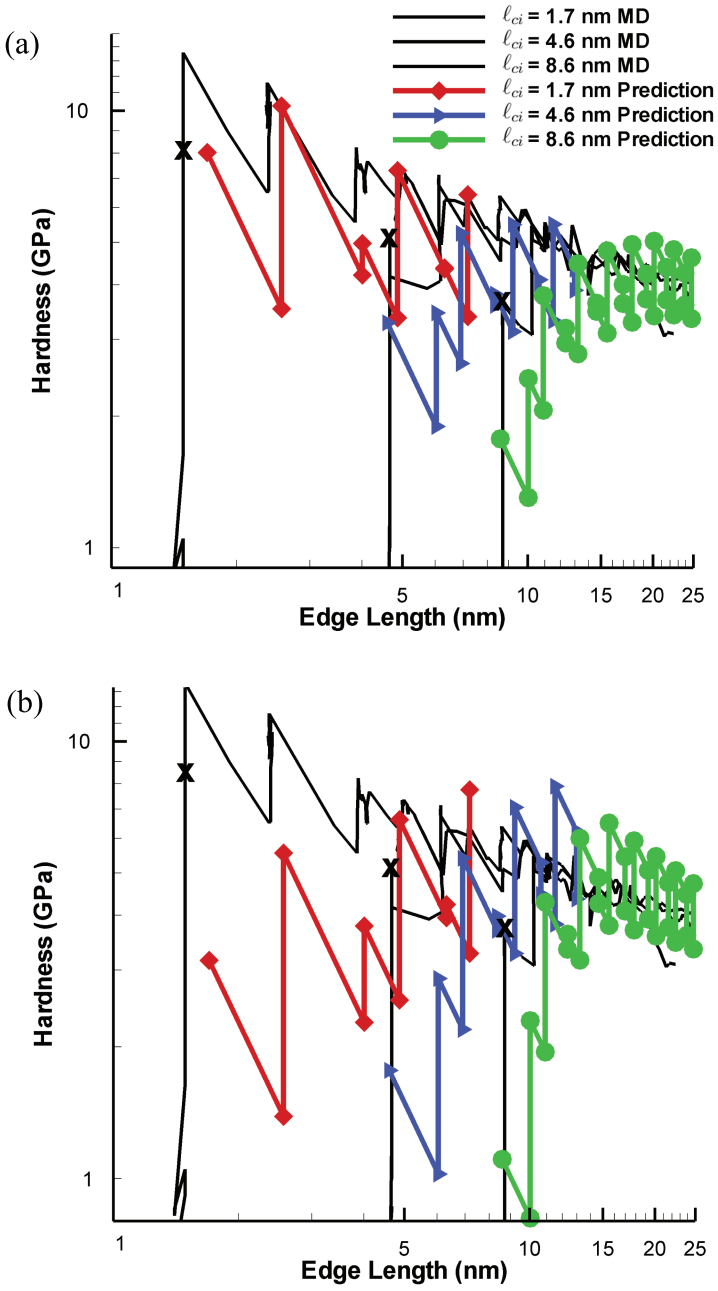

Figure 6.10: Hardness vs. contact edge lengths for nanopyramids, as predicted by the energy-based model at small contact edge lengths, showing accurate predictions of the MD for (a) $N = 10$ and (b) $N = 5$. In each case the red, blue and green lines are the energetic predictions for $\ell_{ci} = 1.7$, 4.6 and 8.6 nm, respectively. The black lines are the results from the MD simulations where the "X" marks the spot of the first SFHO nucleation pressure.

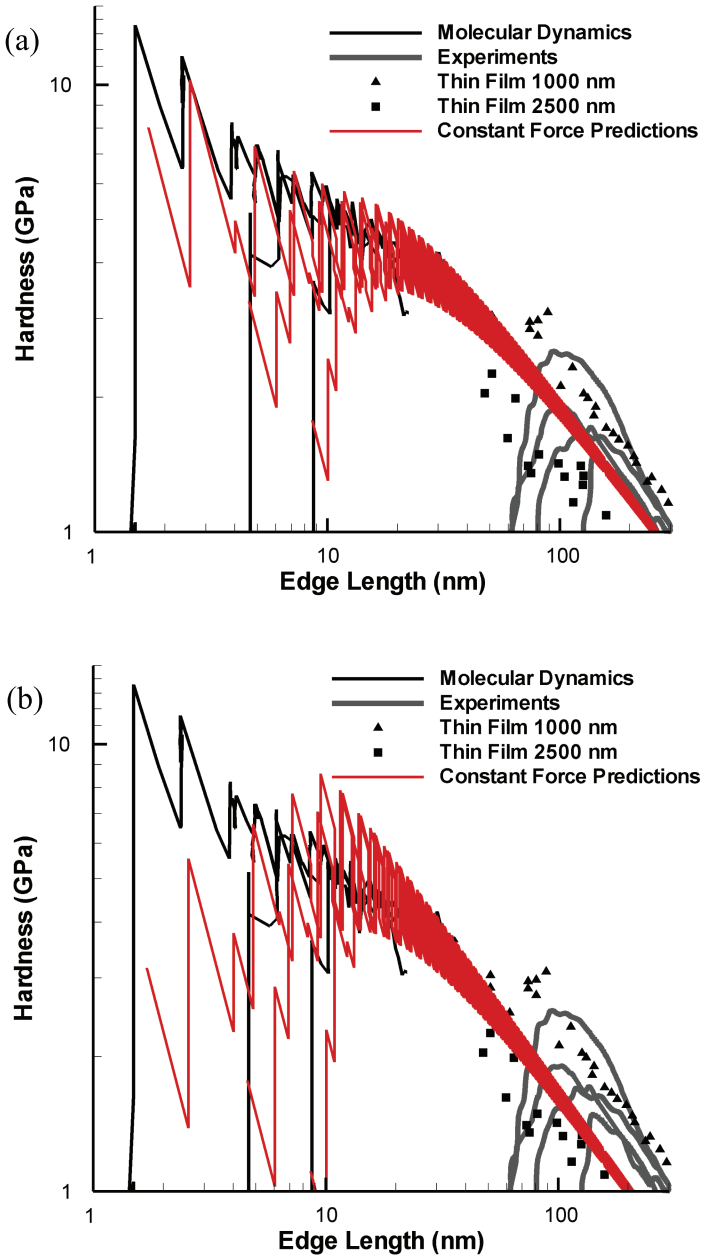

Figure 6.11: Predictions of hardness vs. edge length up to experimental length scales, with solid red lines showing pressure before nucleation and after nucleation for constant force where (a) $N = 10$ and (b) $N = 5$. Dark gray lines are the Wang *et al.* (2006) experiments performed on Au pyramids. Triangles and squares are Nix *et al.* (2007) data for Berkovich indentation of Au (001) films.

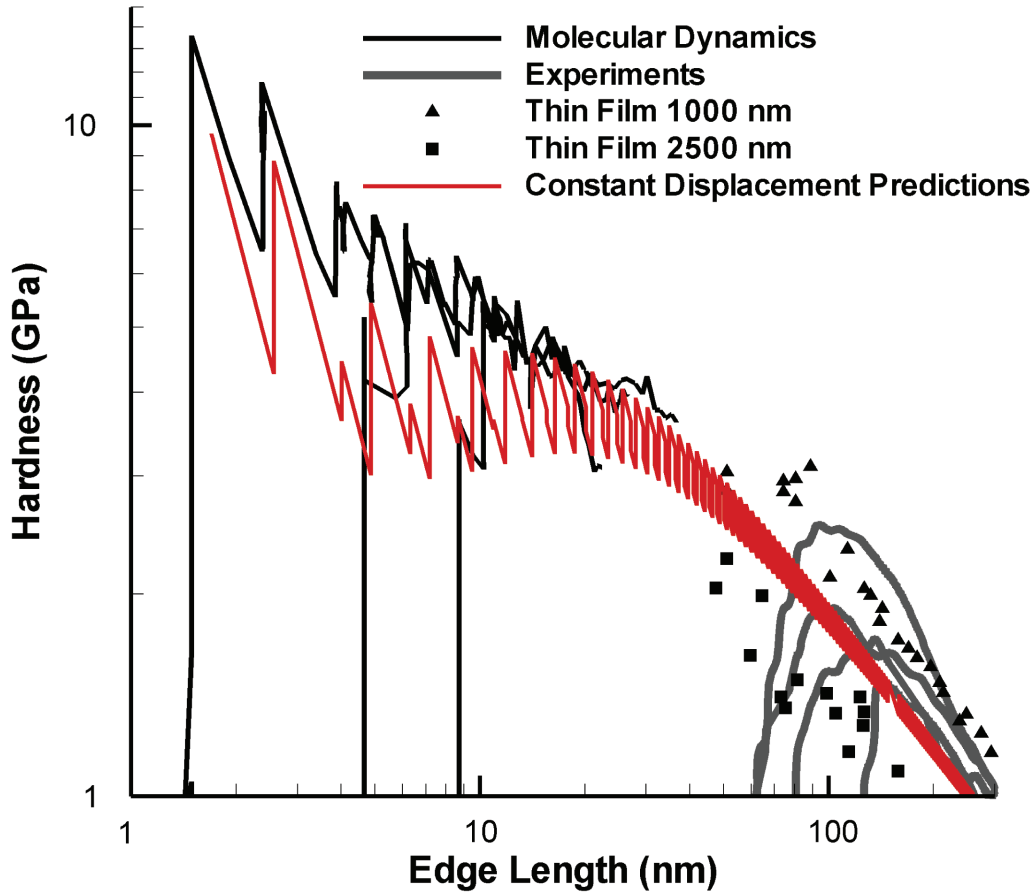

Figure 6.12: Predictions of hardness vs. edge length up to experimental length scales, with solid red lines showing only the real solutions for the pressure before and after nucleation for constant displacement. Dark gray lines are the Wang *et al.* (2006) experiments performed on Au pyramids. Triangles and squares are Nix *et al.* (2007) data for Berkovich indentation of Au (001) films.

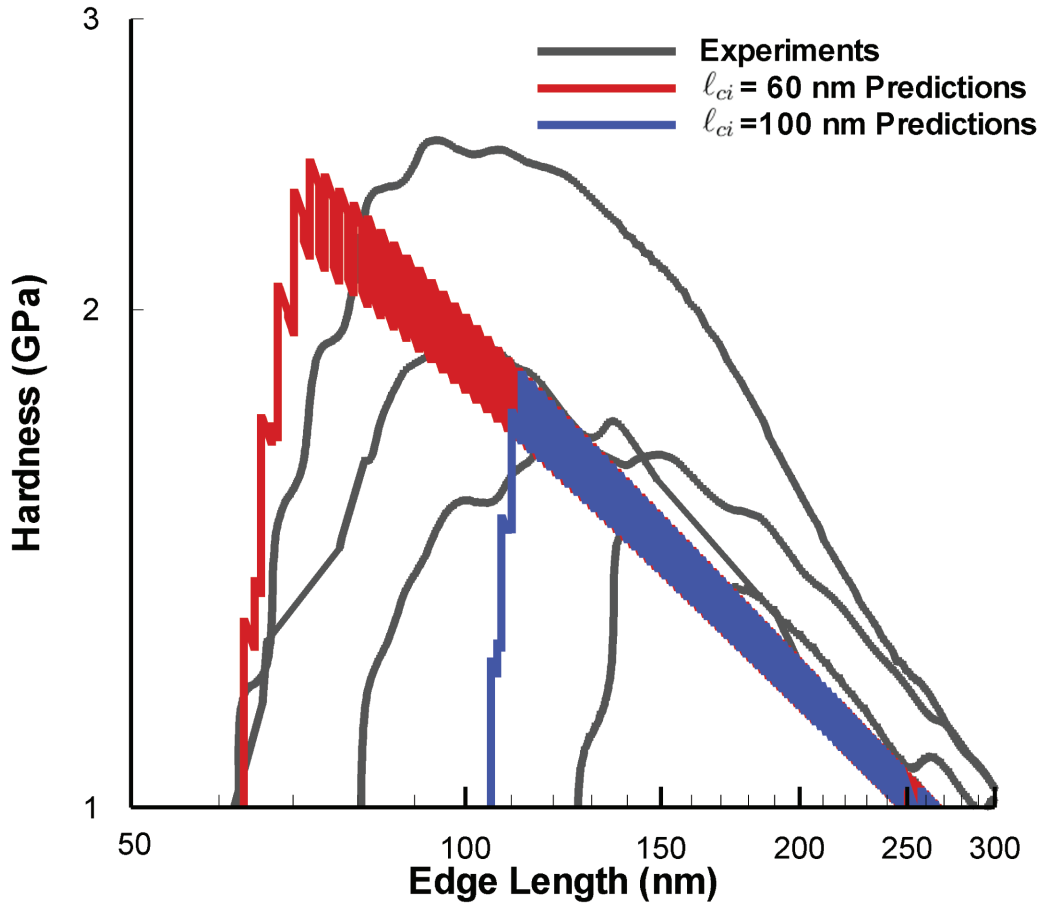

Figure 6.13: Prediction for $\ell_{ci} = 60,\ 100$ nm compared with the experimental pyramid compression. The energetic model effectively captures the magnitudes and scaling even with large initial edge lengths.

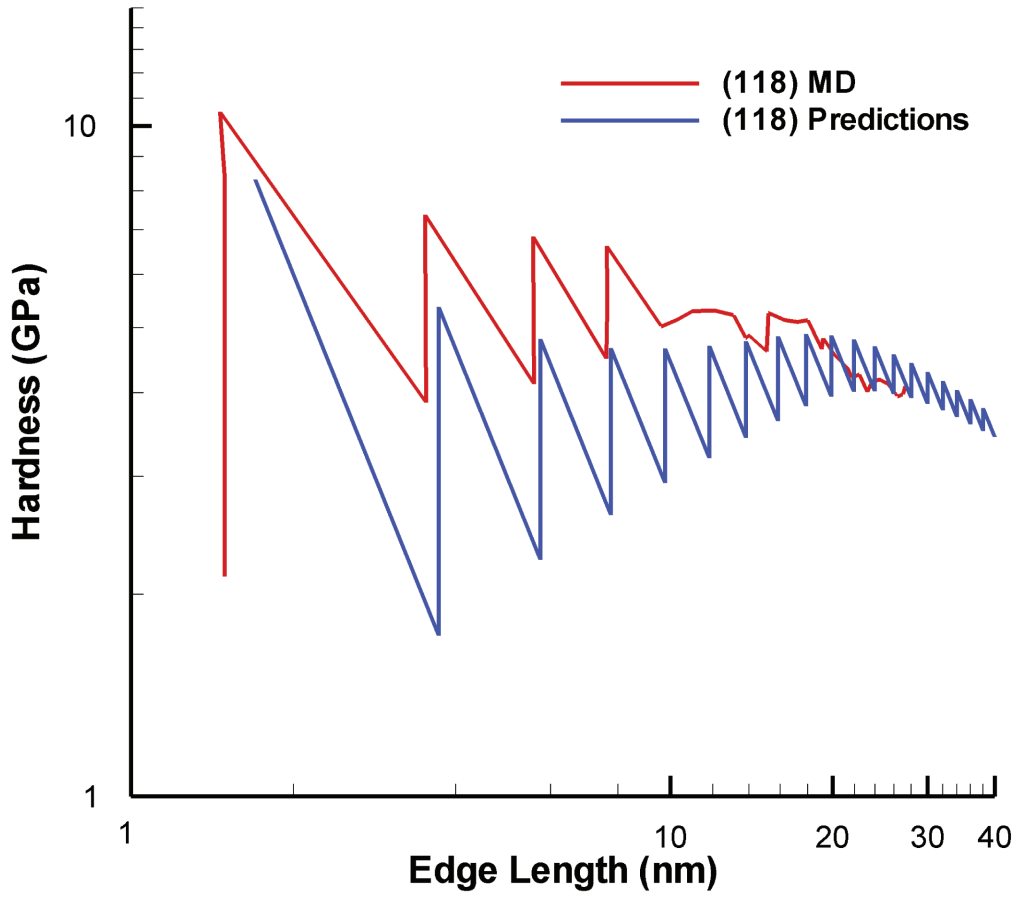

Figure 6.14: Prediction using the energetic model for the (118) faceted pyramid compared to the corresponding MD results.

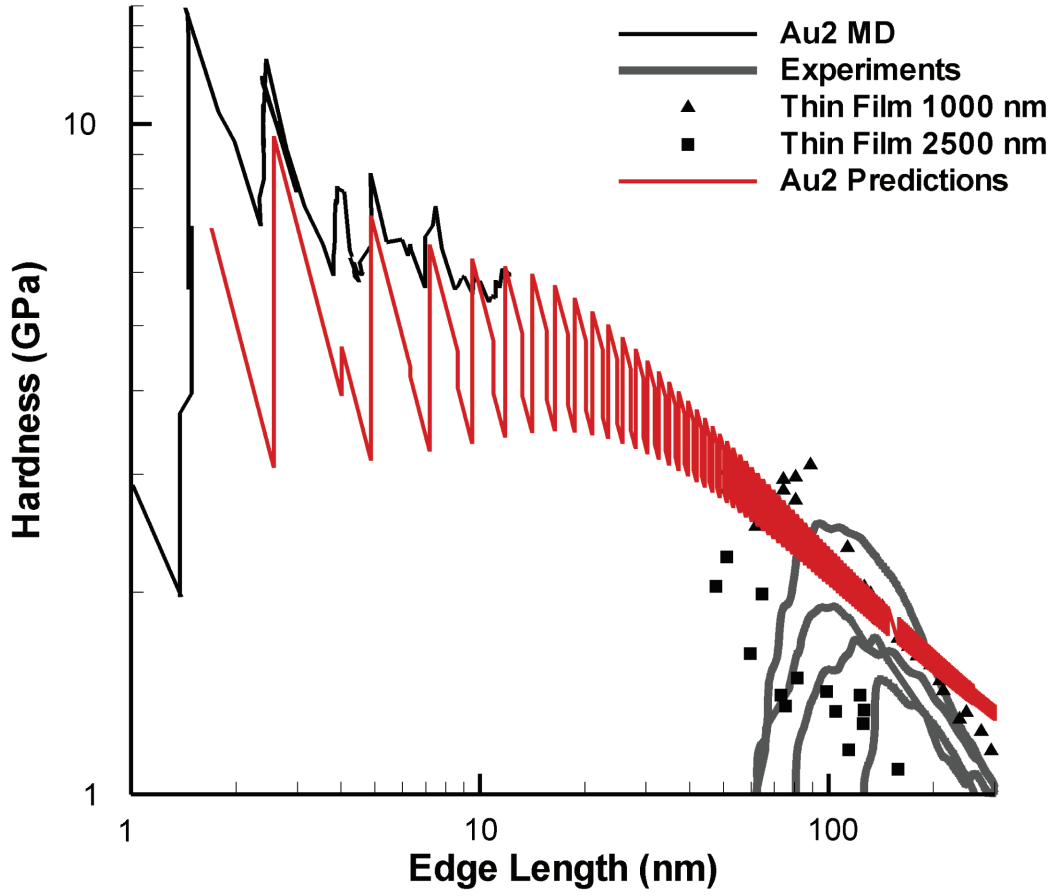

Figure 6.15: Prediction using the energetic model for the Au2 potential with a stacking fault energy of 32 mJ/nm^2 compared to the MD results and experimental pyramid compression.

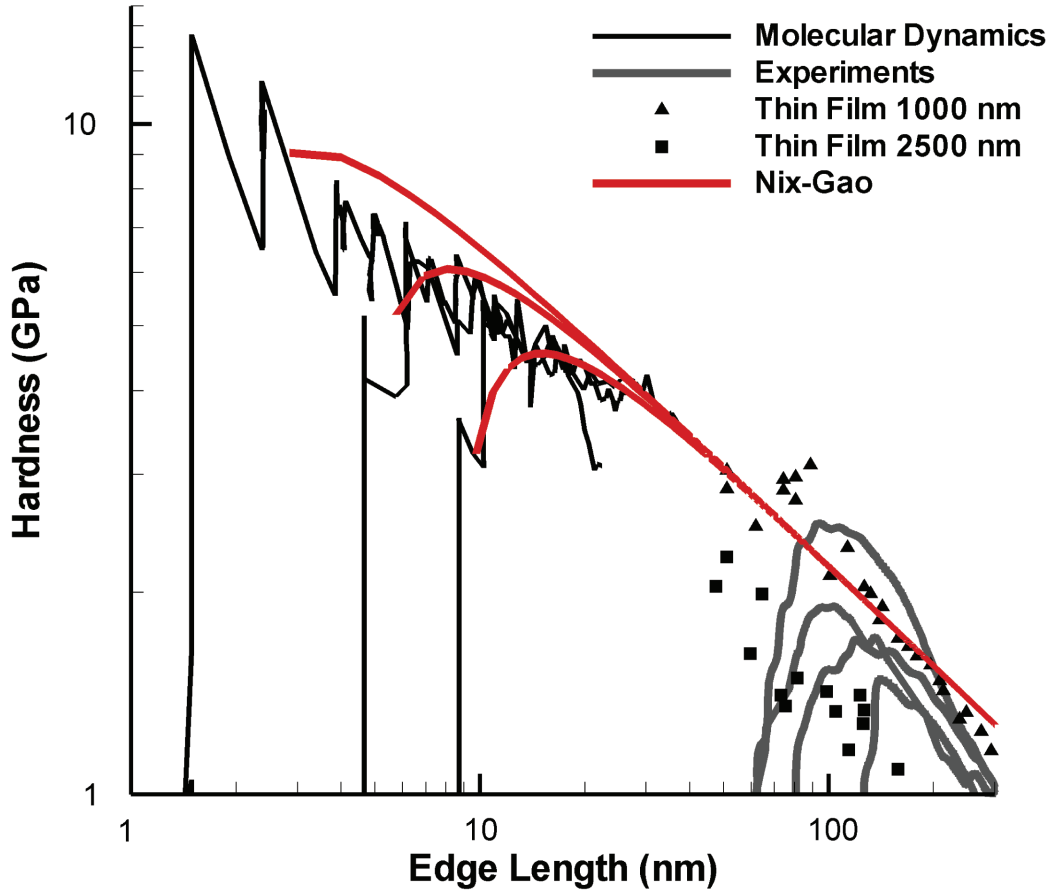

Figure 6.16: Hardness vs. edge length results of the Nix-Gao model (red lines) as applied to the pyramid compression compared with the MD (black lines) and Au pyramid compression experiments (grey lines).

Chapter 7

Concluding remarks

This study has focused on two important aspects of size scaling in systems with important engineering applications. The study of the interfaces and composites of a common casting material and more recently protective coating, Al/Si, has taken the understanding of nanocrystalline materials beyond the well described single phase materials or two phase metals and examines the metal/ceramic nanocomposite for the first time. Examination of the Au nanoasperities offers a study of the smallest length scales of surface roughness and offers and excellent opportunity to compare experiments and models of the size-dependent plasticity at length scales of $5 - 500$ nm.

Three main features of the failure and deformation of Al-Si nanocomposites have been demonstrated through the present molecular dynamics simulations. First, general mismatched Al-Si interfaces are expected to have reasonably high tensile strengths (4-6 GPa) approaching those of the ideal interfaces (~ 7 GPa) but with fracture energies that can be more than twice as large as those for ideal interfaces. Second, the presence of Si grains substantially reduces the deformation in the Al grains and at the Al/Al interfaces but leads to substantial local strains along the Al/Si interfaces in the form of sliding/shearing. With higher Si content, e.g. 6Al-2Si, the Al deformation is

constrained further and the Al/Si interface deformations are more distributed, with an associated increase in the nanocomposite yield stress with increasing Si content. Third, the nanocomposites fail primarily along the Al/Si interface at local tensile stresses, and via failure mechanism, similar to the corresponding bimaterial simulations. Thus, upon introduction of Si grains the deformation and failure are dominated by the Al/Si interfaces. Overall, introduction of the Si grains causes higher elastic modulus and yield strength, but no difference in failure strength, as compared to all-Al nanograin polycrystals. Our results further suggest that control of the interfaces through material modification may thus be one route by which Al/Si nanocomposite properties could be enhanced even further. Coupled with the expected increase in stability of nanocomposite microstructures over those of single-phase metals, the present work indicates that these nanocomposites can have a range of attractive properties. Additional work is needed to understand the role of grain size, and associated changes in the relative roles of dislocation and grain-boundary deformation, on the nanocomposite properties, and on more-realistic microstructures containing more grains and including 3d structure.

Using large-scale molecular dynamics has revealed key features of the size-dependent plastic deformation of nanoscale asperities under contact compression which are extended to general size-scaling for other processes. First, there is a unique size-scaling of the hardness which depends solely on the current contact area, in agreement with experimental trends seen in asperity compression as well as Berkohvich indentation. Second, there is power-law scaling of the hardness with contact length, $H_{MD} \approx \ell_c^{-0.32}$ as compared to $H_{expt} \approx \ell_c^{-0.75}$. Third, with the simulation and experimental sizes approaching one another, unprecedented quantitative agreement is found, with $H_{MD} \approx 4$ GPa for $\ell_c = 36$ nm and $H_{expt} \approx 2.5$ GPa for slightly larger contact lengths of $\ell_c = 100$ nm. Fourth, the simulations show that the main plastic

deformation mechanism is successive nucleation of stacking-fault half octahedra. Finally, unloading shows that at small length scales the deformation is reversible, but as soon as dislocations begin to intersect and twinning occurs deformation becomes permanent and the unloaded structures have increased contact areas due to mass transport but the majority of the energy is conserved by the plastic structures.

With the insight from the MD an analytic model that incorporates the energy cost of nucleating the s.f.h.o. dislocation structure predicts a lower bound for the hardness in qualitative and quantitative agreement with the MD. With just four adjustable parameters, C_θ, C_w, C_{cut} and N, the model sets a lower bound for the first nucleation event as well as a similar effective scaling, $H \approx \ell_c^{-0.5}$. The model also captures the increase in hardness after the first nucleation event due to the interaction energy with the previously nucleated s.f.h.o. Along with the increase in hardness other important features of the hardness associated with alternating edge lengths are captured by the energetics. From the model the scaling can easily be explained by the contribution of the dislocation interaction energies which keep the energy from dropping off to the predicted ideal ℓ_c^{-1} scaling. The model thus establishes a lower bound for the hardness magnitudes and effectively captures the scaling for both MD and experiments. The model also suggests a transitions from nucleation driven scaling for $\ell_c < 10$ nm to interaction driven scaling for larger length scales..

One great benefit of the model is that only geometry and material properties are needed as model inputs, making it broadly applicable to other asperity geometries and perhaps other nanoscale deformation experiments. This study successfully establishes an understanding of the size-scaling for nanoscale asperities at lengths not previously described by other models, PN, RT and Nix-Gao methods. Ultimately large-scale MD and the energetic model bridge the proverbial gap between atomistics

and experimental length scales and establish the size-scaling origins of nanoscale asperities ranging in size from $5 - 500$ nm, and can be used to predict contact hardness and eventually friction behavior of realistic multiple-asperity surfaces.

Bibliography

Adams, C., Atzmon, M., Cheng, Y.-T. and Srolovitz, D. (1992), 'Phase separation during co-deposition of Al-Ge thin films', *Journal of Materials Research* **7**, 653.

Aifantis, E. (1999), 'Strain gradient interpretation of size effects', *International Journal of Fracture* **95**, 299.

Allen, M. and Tildesley, D. (1989), *Computer Simulation of Liquids*, Oxford University, NY.

Armstrong, R., Chou, Y., Fisher, R. and Louat, N. (1966), 'The limiting grain size dependence of the strength of a polycrystalline aggregate', *Philosophical Magazine* **14**, 943.

Baskes, M. (1992), 'Modified embedded-atom potentials for cubic materials and impurities', *Physical Review B* **46**(5), 2727.

Baskes, M., Angelo, J. and Bisson, C. (1994), 'Atomistic calculations of composite interfaces', *Modelling and Simulation in Materials Science and Engineering*.

Beeler Jr., J. (1983), *Radiation effects computer experiments*, North-Holland Publishing, NY.

Cheng, Y. and Drew, G. (1997), 'Silver-nickel nano-composite coating for terminals of separable electrical connectors'.

Chng, A. C., O'day, M. P., Curtin, W. A., Tay, A. A. and Lim, K. M. (2006), 'Fracture in confined thin films: A discrete dislocation study', *Acta Materialia* **54**, 1017.

Clementi, E. and Roetti, C. (1974), *Atomic Data Tables* **14**, 177.

Daw, M. S. and Baskes, M. (1983), 'Semiempirical, Quantum Mechanical Calculation of Hydrogen Embrittlement in Metals', *Physical Review Letters* **50**(17), 1285.

Daw, M. S. and Baskes, M. (1984), 'Embedded-atom method: Derivation and application to impurities, surfaces, and other defects in metals', *Physical Review B* **29**(12), 6443.

Derlet, P. and Van Swygenhoven, H. (2002), 'Length scale effects in the simulation of deformation properties of nanocrystalline metals', *Scripta Materialia* **47**, 719.

Deshpande, V., Needleman, A. and Van der Giessen, E. (2005), 'Plasticity size effects in tension and compression of single crystals', *Journal of the Mechanics and Physics of Solids* **53**, 2661.

Diao, J., Gall, K. and Dunn, M. L. (2004), 'Atomistic simulation of the structure and elastic properties of gold nanowires', *Journal of the Mechanics and Physics of Solids* **52**, 1935.

Eshelby, J. (1957), 'The determination of the elastic field of an ellipsoidal inclusion, and related problems', *Proceedings of the Royal Society of London. Series a, Mathematical and Physical Sciences* **241**(1226), 376.

Espinosa, H., Prorok, B. and Peng, B. (2004), 'Plasticity size effects in free-standing submicron polycrystalline FCC films subjected to pure tension', *Journal of the Mechanics and Physics of Solids* **52**, 667.

Farhat, Z., Ding, Y., Northwood, D. and Alpas, A. (1996), 'Effect of grain size on friction and wear of nanocrystalline aluminum', *Materials Science and Engineering* **A206**, 302.

Farkas, D. and Curtin, W. A. (2005), 'Plastic deformation mechanisms in nanocrystalline alumnar grain structures', *Materials Science and Engineering A* **412**, 316.

Farkas, D., Van Swygenhoven, H. and Derlet, P. (2002), 'Intergranular fracture in nanocrystalline metals', *Physical Review B* **66**, 060101.

Fleck, N. and Hutchinson, J. (1997), 'Strain gradient plasticity', *Advances in Applied Mechanics* **33**, 295.

Fleck, N. and Hutchinson, J. (2001), 'A reformulation of strain gradient plasticity', *Journal of the Mechanics and Physics of Solids* **49**, 2245.

Fleck, N., Muller, G., Ashby, M. and Hutchinson, J. (1994), 'Strain gradient plasticity: Theory and experiment', *Acta metall. mater.* **42**(2), 475.

Foiles, S., Baskes, M. and Daw, M. (1986), 'Embedded-atom-method functions for the fcc metals Cu, Ag, Au, Ni, Pd, Pt, and their alloys', *Physical Review B* **33**(12), 7983.

Foiles, S., Daw, M. and Wilson, W. (1984), 'Application of the embedded atom method to transition metal alloys', *Metallurgical Soc of AIME* p. 275.

Friedman, L. H. and Chrzan, D. (1998), 'Continuum analysis of dislocation pile-ups: influence of sources', *Philosophical Magazine A* **77**(5), 1185.

Fucutani, K., Tanji, K., Motoi, T. and Den, T. (2004), 'Ultrahigh pore density nanoporous films produced by the phase separation of eutectic Al-Si for template-assisted growth of nanowire arrays', *Advanced Materials* **16**(16), 1456.

Gall, K., Horstemeyer, M., Van Schilfgaarde, M. and Baskes, M. (2000), 'Atomistic simulations on the tensile debonding of an aluminum-silicon interface', *Journal of the Mechanics and Physics of Solids* **48**(10), 2183.

Gao, Z. (1995), 'A circular inclusion with imperfect interface: Eshelby's tensor and related problems', *Journal of Applied Mechanics, Transactions of ASME* **62**, 860.

Gerberich, W. W., Mook, W., Chambers, M., Cordill, M., Perrey, C., Carter, C., Miller, R., Curtin, W., Mukherjee, R. and Girshick, S. (2006), 'An energy balance criterion for nanoindentation-induced single and multiple dislocation events', *Journal of Applied Mechanics* **73**, 327.

Greer, J. and Nix, W. (2005), 'Size dependence of mechanical properties of gold at the sub-micron scale', *Applied Physics A* **80**, 1625.

Greer, J. R., Oliver, W. C. and Nix, W. D. (2005), 'Size dependence of mehanical properties of gold at the micron scale in the absence of strain gradients', *Acta Materialia* **53**, 1821.

Hall, E. (1951), 'The Deformation and Ageing of Mild Steel: III Discussion of Results', *Proceeding of the Physical Society London Section B* **64**, 747.

Haslam, A., Phillpot, S., Wolf, D., Moldovan, D. and Gleiter, H. (2001), 'Mechanisms of grain growth in nanocrystalline fcc metals by molecular-dynamics simulation', *Materials Science and Engineering A* **318**, 293.

Hirth, J. and Lothe, J. (1968), *Theory of Dislocations*, McGraw-Hill, NY.

Hoover, G. W. (1985), 'Canonical dynamics: Equilibrium phase-space distributions', *Physical Review A* **31**, 1695.

Imura, T. and Saka, H. (1983), *The Structure and Properties of Crystal Defects*, Elsevier , NY.

Kelchner, C. L., Plimpton, S. and Hamilton, J. (1998), 'Dislocation nucleation and defect structure during surface indentation', *Physical Review B* **58**(17), 11085.

Lane, M., Dauskardt, R. H., Vainchtein, A. and Gao, H. (2000), 'Plasticity contributions to interface adhesion in thin-film interconnect structures', *Journal of Materials Research* **15**(12), 2758.

Latapie, A. and Farkas, D. (2003), 'Effect of grain size on the elastic properties of nanocrystalline α -iron', *Scripta Materialia* **48**, 611.

Lee, B.-J., Baskes, M., Kim, H. and Cho, Y. K. (2001), 'Second nearest-neighbor modified embedded atom method potentials for bcc transition metals', *Physical Review B* **64**, 184102.

Lee, B.-J., Shim, J.-H. and Baskes, M. (2003), 'Semiempirical atomic potentials for the fcc metals Cu, Ag, Au, Ni, Pd, Pt, Al, and Pb based on first and second nearest-neighbor modified embedded atom method', *Physical Review B* **68**, 144112.

Lee, K. and Paul, D. (2005), 'A model for composites containing three-dimensional ellipsoidal inclusions', *Polymer* **46**, 9064.

Louchet, F., Weiss, J. and Richeton, T. (2006), *Hall-Petch Law Revisited in Terms of Collective Dislocation Dynamics*, Vol. 97.

McLean, A. and McLean, R. (1981), *Atomic Data Nucl. Data Tables* **26**, 197.

McLellan, A. (1974), 'Virial Theorem Generalized', *American Journal of Physics* **42**(3), 239.

Miller, R. E., Shilkrot, L. and Curtin, W. A. (2004), 'A coupled atomistics and discrete dislocation plasticity simulation of nanoindentation into single crystal thin films', *Acta Materialia* **52**, 271.

Nicola, L., Xiang, Y., Vlassak, J., Van der Giessen, E. and Needleman, A. (2006), 'Plastic deformation of freestanding thin films: Experiments and modeling', *Journal of the Mechanics and Physics of Solids* **54**, 2089.

Nix, W. D. (1989), 'Mechanical Properties of Thin Films', *Metallurgical Transactions A*.

Nix, W. D. and Gao, H. (1998), 'Indentation size effects in crystalline materials: A law for strain gradient plasticity', *Journal of the Mechanics and Physics of Solids* **46**(3), 411.

Nix, W. D., Greer, J. R., Feng, G. and Lilleodden, E. T. (2007), 'Deformation at the nanometer and micrometer length scales: Effects of strain gradients and dislocation starvation', *Thin Solid Films* **515**, 3152.

Nordsieck, A. (1962), 'On numerical integration of ordinary differential equations', *Mathematics of Computation* **16**(77), 22.

Nose, S. (1984), 'A unified formulation of the constatn temperature molecular dynamics method', *Journal of Physics and Chemistry* **81**, 511.

Olk, C. H. and Haddad, D. (2006), 'Characterization and control of microstructure in combinatorially prepared aluminum-silicon thin film nanocomposites', *Journal of Materials Research* **21**(5), 1221.

Olk, C. H., Lukitsch, M. and Haddad, D. (2006), 'Combinatorial investigation of the mechanical properties of aluminum-silicon thin film nanocomposites', *Journal of Materials Research*.

Park, H. S. and Zimmerman, J. A. (2005), 'Modeling inelasticity and failure in gold nanowires', *Physical Review B* **72**, 054106.

Park, H. S., Gall, K. and Zimmerman, J. A. (2006), 'Deformation of FCC nanowires by twinning and slip', *Journal of the Mechanics and Physics of Solids* **54**, 1862.

Petch, N. (1953), 'The cleavage strength of polycrystals', *Journal of the Iron and Steel Institute London* **174**, 25.

Phillips, R. (2001), *Crystal, Defects and Microstructure: Modeling across scales*, Cambridge University, UK.

Picu, C. R. and Gupta, V. (1996), 'Stress singularities at triple junctions with freely sliding grains', *International Journal of Solids and Structures* **33**(11), 1535.

Ping, D., Hono, K. and Inoue, A. (2000), 'Microstructural Characterization of a Rapidly Solidified Ultrahigh Strength $Al_{94.5}Cr_3Co_{1.5}Ce_1$ Alloy', *Metallurgical and Materials Transactions*.

Qi, Y. and Cheng, Y. (2004), Molecular Dynamics Simulation of Deformation and Fracture in Nano-Crystalline Silver and Silver-Nickel, General Motors Report R&D Report-9947.

Qu, S., Huang, Y., Nix, W., Jiang, H., Zhang, F. and Hwang, K. (2004), 'Indenter tip radius effect on the Nix-Gao relation in micro- and nanoindentation hardness experiments', *Journal of Materials Research* **19**(11), 3423.

Rice, J. and Thomson, R. (1974), 'Ductile versus brittle behavior of crystals', *Philos. Mag.* **29**, 73.

Rice, J. R. (1992), 'Dislocation nucleation from a crack tip: An analysis based on the peierls concept', *Journal of the Mechanics and Physics of Solids* **40**(2), 239.

Schiøtz, J., Di Tolla, F. D. and Jacobsen, K. W. (1998), 'Softening of nanocrystalline metals at very small grain sizes', *Nature* **391**, 561.

Schiøtz, J., Vegge, T., Di Tolla, F. and Jacobsen, K. (1999), 'Atomic-scale simulations of the mechanical deformation of nanocrystalline metals', *Physical Review B* **60**(17), 11971.

Shenoy, V. B., Phillips, R. and Tadmor, E. B. (2000), 'Nucleation of dislocations beneath a plane strain indenter', *Journal of the Mechanics and Physics of Solids* **48**, 649.

Shilkrot, L., Curtin, W. and Miller, R. (2002), 'A coupled atomistic/continuum model of defects in solids', *Journal of the Mechanics and Physics of Solids* **50**, 2085.

Shilkrot, L., Miller, R. and Curtin, W. (2002), 'Coupled atomistic and discrete dislocation plasticity', *Physical Review Letters* **89**(2), 25501.

Sieradzki, K., Rinaldi, A., Friesen, C. and Peralta, P. (2006), 'Length scales in crystal plasticity', *Acta Materialia* **54**, 4533.

Tadmor, E., Ortiz, M. and Phillips, R. (1996), 'Quasicontinuum analysis of defects in solids', *Philosophical Magazine A: Physics of Condensed Matter, Defects and Mechanical Properties* **73**(6), 1529.

Takahashi, K., Nara, C., Yamagishi, T. and Onzawa, T. (1999), 'Calculation of surface energy and simulation of reconstruction for Si(111) 3x3, 5x5, 7x7, and 9x9 DAS structure', *Applied Surface Science* **151**, 299.

Tan, S., Berry, B. and Crowder, B. (1972), 'Elastic and anelastic behavior of ion-implanted silicon', *Applied Physics Letters* **20**(2), 88.

Tvergaard, V. and Hutchinson, J. W. (1988), 'Microcracking in ceramics induced by thermal expansion or elastic anisotropy', *Journal of the American Ceramic Society* **71**(3), 157.

Uchic, M. D., Dimiduk, D. M., Florando, J. N. and Nix, W. D. (2004), 'Sample Dimensions influence strength and crystal plasticity', *Science* **305**, 986.

van der Giessen, E. and Needleman, A. (1995), 'Discrete dislocation plasticity: A simple planar model', *Modelling and Simulation in Materials Science and Engineering* **3**, 689.

Van Swygenhoven, H., Derlet, P. and Hasnaoui, A. (2002), 'Atomic mechanism for dislocation emission from nanosized grain boundaries', *Physical Review B* **66**, 024101.

Van Swygenhoven, H., Derlet, P. and Hasnaoui, A. (2003), 'Atomistic modeling of strength of nanocrystalline metals', *Advanced Engineering Materials* **5**(5), 345.

Van Swygenhoven, H., Spaczér, M., Farkas, D. and Caro, A. (1999), 'The role of grain size and the presence of low and high angle grain boundaries in the deformation mechanism of nanophase Ni: A molecular dynamics computer simulation', *Nano Structured Materials* **12**, 323.

Verlet, L. (1967), 'Computer "experiments" on classical fluids. I. Thermodynamical properties of Lennard-Jones molecules', *Physical Review* **159**(1), 98.

Volkert, C. and Lilleodden, E. (2006), 'Size effects in the deformation of sub-micron Au columns', *Philosophical Magazine*.

Wang, J., Lian, J., Greer, J. R., Nix, W. D. and Kim, K.-S. (2006), 'Size effect in contact compression of nano- and microscale pyramid structures', *Acta Materialia* **54**(15), 3973.

Warner, D., Curtin, W. and Qu, S. (2007), 'Rate dependence of crack-tip processes predicts twinning trends in f.c.c. metals', *Nature Materials*.

Widjaja, A., Van der Giessen, E. and Needleman, A. (2005), 'Discrete dislocation modelling of submicron indentation', *Materials Science and Engineering A*.

Widjaja, A., Van der Giessen, E., Deshpande, V. S. and Needleman, A. (2007), 'Contact area and size effects in discrete dislocation modeling of wedge indentation', *J. Mater. Res.* **22**, 655.

Xiang, Y. and Vlassak, J. (2006), 'Bauschinger and size effects in thin-film plasticity', *Acta Materialia* **54**, 5449.

Yamakov, V., Wolf, D., Phillpot, S. and Gleiter, H. (2003), 'Dislocation-dislocation and dislocation-twin reactions in nanocrystalline Al by molecular dynamics simulation', *Acta Materialia* **51**(14), 4135.

Yamakov, V., Wolf, D., Phillpot, S. R., Mukherjee, A. K. and Gleiter, H. (2002), 'Dislocation processes in the deformation of nanocrystalline aluminium by molecular-dynamics simulation', *Nature Materials* **1**(1), 45.

Yamakov, V., Wolf, D., Salazar, M., Phillpot, S. and Gleiter, H. (2001), 'Length-scale effects in the nucleation of extended dislocations in nanocrystalline Al by molecular-dynamics simulation', *Acta Materialia* **49**, 2713.

Zhang, Y., Wang, T. and Tang, Q. (1995), 'The effect of thermal activation on dislocation processes at an atomistic crack tip', *Journal of Physics D: Applied Physics* **28**(4), 748.

Zhu, T. and Yip, S. (2004), 'Atomistic study of dislocation loop emission from a crack tip', *Physical Review Letters* **93**(2), 025503.

Zong, Z., Lou, J., Adewoye, O., Elumstafa, A., Hammad, F. and Soboyejo, W. (2006), 'Indentation size effects in the nano- and micro-hardness of fcc single crystal metals', *Materials Science and Engineering A* **434**, 178.